

Flexural Capacity of Slender Web Plate Girders

by

Jon F. Richter, B.S.

THESIS

Presented to the Faculty of the Graduate School

of The University of Texas at Austin

in Partial Fulfillment

of the Requirements

for the Degree of

MASTER OF SCIENCE IN ENGINEERING

The University of Texas at Austin

May 1998

ACKNOWLEDGEMENTS

This research was made possible through funding provided by the Metal Building Manufacturers and the American Institute of Steel Construction. Deep gratitude is extended to those who enabled this research to be conducted.

The author would also like to express his sincere appreciation to Dr. Joseph A. Yura for his limitless patience and assistance in completing this work. After having the privilege of working with a man of Dr. Yura's caliber, it is easily understood how he earned the reputation of being such a great mind in this field. Special thanks also goes out to Dr. Karl H. Frank for his advice throughout this work and to Juan Estevez whose assistance in the lab helped me to see the lighter side of engineering.

I would like to thank my parents and family for their undying support, love and advice throughout this period of my life. Without you, none of this would have been possible and with you I will continue to grow and develop into an individual that I can be proud of. I would also like to thank Lainie Simon for bringing to my attention some of the greatest things life has to offer. Through our friendship, I have become more in tune to the true meaning of happiness.

I would like to extend my appreciation to Parry Berkowitz. Parry's assistance made the computer analysis portion of this research possible, but his loyal friendship is what truly deserves the recognition. Finally, I would like to thank both Dave Mcilrath and Charles Bowen for their friendship, and reassure them that it will never be forgotten once we part ways.

Jon Richter

April 30, 1998

ABSTRACT

Flexural Capacity of Slender Web Plate Girders

by

Jon Richter

The University of Texas at Austin, 1998

Supervisor: Dr. Joseph A. Yura

Steel beams subjected to bending loads about the strong axis of the section can fail due to yielding, local flange buckling, shear buckling or flexural buckling of the web, and lateral torsional buckling between lateral brace points. In the AISC-LRFD Specification (1993), the design strengths for each of the limit states mentioned above can be found in Appendices F and G. The web slenderness determines which of these two Appendices controls the design strength. Since these Appendices were developed independently, no smooth transition exists between them. This discrepancy can be corrected if the web slenderness of a beam affects its flexural strength.

In order to accomplish this, a test program was designed to investigate a wide distribution of web slenderness ratios. This program consisted of twenty-eight plate girders that were loaded under uniform moment. The main variables in the program were web slenderness, unbraced length and flange slenderness.

These loads were compared to the strength provisions of both Appendices to examine their accuracy.

TABLE OF CONTENTS

ABSTRACT	VI
LIST OF TABLES	X
LIST OF FIGURES	XI
CHAPTER 1: INTRODUCTION	1
CHAPTER 2: DESIGN SPECIFICATION	5
2.1 YIELDING.....	5
2.2 Lateral Torsional Buckling.....	9
2.2.1 Elastic Region	12
2.2.2 Inelastic Region.....	16
2.3 Flange Local Buckling.....	17
2.4 Web Local Buckling.....	20
2.5 Related Research	25
2.5.1 The Barth Equation	26
2.5.2 The Fukumoto Method.....	28
CHAPTER 3: BEAM EXPERIMENTS	30
3.1 Test Setup.....	30
3.2 Section Properties.....	34
3.3 Material Properties	39
3.4 Data Acquisition and Testing Techniques.....	41

3.5 Experimental Procedures.....	42
CHAPTER 4: TEST RESULTS.....	45
4.1 General Behavior.....	45
4.2 Compact Flange Tests	49
4.2.1 Tests 17-22, 30 in. Web	50
4.2.2 Tests 11-16, 24 in. Web	55
4.2.3 Tests 5-10, 18 in. Web	58
4.2.4 Tests 1-4, 15 in. and 12 in. Web	60
4.3 Non-Compact Flange Tests, Tests 23 - 29	62
4.4 Fully Braced Compact Flange Tests.....	65
CHAPTER 5: FINITE ELEMENT ANALYSIS	67
5.1 Finite Element Model.....	67
5.2 Finite Element Results	71
5.2.1 Lateral Torsional Buckling Tests ($L_b = 100$ in., 75 in. and 60 in.).....	73
5.2.2 Fully Braced Test ($L_b = 37.5$ in.).....	77
5.3 Conclusions from FEM Results	80
CHAPTER 6: DESIGN RECOMMENDATIONS.....	82
6.1 Design Provisions.....	82
6.2: Recommendations	89

CHAPTER 7: SUMMARY AND CONCLUSIONS	92
APPENDIX I: IMPORTANT EQUATIONS.....	93
APPENDIX II: LOAD DEFLECTION PLOTS.....	96
APPENDIX III: LIST OF VARIABLES	125
BIBLIOGRAPHY.....	128
VITA	130

LIST OF TABLES

Table 2.1: Limiting Slenderness Parameters for Appendix F and G	9
Table 3.1: Measured Cross Section Dimensions For Test Specimens	35
Table 3.2a: Material Properties	40
Table 3.2b: Applicable Appendix For Various Web Ratios.....	40
Table 4.1: Results of Compact Flange Tests	51
Table 3.2b: Results of Non-Compact Flange Tests	63
Table 6.1: Allowable And Actual Initial Web Displacements	87

LIST OF FIGURES

Figure 1.1: Moment Capacity vs. Web Slenderness	2
Figure 2.1 Typical Lateral-Torsional Buckling Graph	6
Figure 2.2: R_e Reduction Factor Comparison	7
Figure 2.3: Slenderness Parameter vs. Unbraced Length for Both Appendices 11	
Figure 2.4: Distortion of Slender Web	15
Figure 2.5: Typical Flange Local Buckling Graph	18
Figure 2.6: Effect of Web Slenderness On Local Flange Buckling	19
Figure 2.7: Typical Web Local Buckling Graph	20
Figure 2.8a: Theoretical and True Bending Stress Distributions	22
Figure 2.8b: Cross Section And Stress Distribution Assumed By Basler	23
Figure 2.9: Effect of Web Slenderness on The R_{PG} Reduction Factor	24
Figure 2.10: Effect of a_r On The R_{PG} Reduction Factor	25
Figure 2.11: Comparison of Barth Equation to AISC-LRFD Specification ..	27
Figure 2.12: Comparison of Fukumoto Equation to AISC-LRFD Specifications	29
Figure 3.1: Test Setup	30
Figure 3.4: End Plate Moment Connection	33
Figure 3.5: Support Roller	34
Figure 3.6: Depths Investigated	36
Figure 3.7: Flange Widths Investigated	37
Figure 3.8: Unbraced Lengths Investigated	38
Figure 3.9: Tightening Of Bolts On Moment Connection Using Impact Wrench	43
Figure 4.1: Typical Load-In-Plane Displacement Curve	46
Figure 4.2: Typical Load-Lateral Displacement Curve	46
Figure 4.3: Typical Yield Pattern	47
Figure 4.4: Initial Yielding On Compression Flange Adjacent To Web Splice 48	
Figure 4.5: Oil Canning of 30 in. Web	49
Figure 4.6: Test Results for 30 in. Deep Girder	52
Figure 4.7: Lateral Torsional Buckle of 30 in. Deep Specimen	53
Figure 4.8: Web Cripple of 30 in. Girder At End Plate Connection	54
Figure 4.9: Twisting of Tension Flange	55
Figure 4.10: Test Results for 24 in. Deep Girder	56
Figure 4.11: Lateral Torsional Buckle of 24 in. Deep Specimen	57
Figure 4.12: Test Results for 18 in. Deep Girder	59

Figure 4.13: Test Results for 15 in. Deep Girder	60
Figure 4.14: Test Results for 12 in. Deep Girder	61
Figure 4.15: Typical Flange Local Buckle	62
Figure 4.16: Flange Local Buckling Results	64
Figure 4.17: Typical Web Local Buckle	66
Figure 5.1: FEM Model of Test Setup	68
Figure 5.2: Typical Initial Displacement For All FEM Models	69
Figure 5.3: Stress-Strain Curve For The Isotropic Hardening Model	70
Figure 5.4: Test and Predicted ABAQUS Load compared to AISC-LRFD Specification	72
Figure 5.5: Stress Contour For The 100 in. Unbraced Length Model	74
Figure 5.6: Stress Contour For The 75 in. Unbraced Length Model	76
Figure 5.7: Stress Contour For The 60 in. Unbraced Length Model	77
Figure 5.8: Stress Contour For The Fully Braced Model	78
Figure 5.9: Load-Deflection Curve For Fully Braced ABAQUS Model	79
Figure 6.1: Nondimensionalized Appendix F Flexural Strength Provisions	83
Figure 6.2: Appendix F Strength Curves With Test Loads For 18 in., 24 in. and 30 in. Sections	84
Figure 6.2: Appendix F Strength Curves With Test Loads For 15 in and 12 in. Sections	85
Figure 6.4: Nondimensionalized Appendix G Flexural Strength Provisions	86
Figure 6.7: Fukumoto Strength Predictions With Test loads	88
Figure 6.8: Percent of Plastic Moment Reached vs. Web Slenderness	90
Figure 6.9: Reduced Appendix F Strength Provisions With Tests For 24 in. Section	91

CHAPTER 1

INTRODUCTION

Steel beams subjected to bending loads about the strong axis of the section can fail due to yielding, local flange buckling, shear buckling or flexural buckling of the web, and lateral torsional buckling between lateral brace points. In the AISC-LRFD Specification (1993), the design strengths for each of the limit states mentioned above can be found in Appendices F and G. The web slenderness ratio, h/t_w , of the section, where h is the clear depth of the web and t_w is the web thickness, determines which of these two Appendices controls the design strength. Typically, rolled sections are controlled by Appendix F and slender web welded built-up sections are controlled by Appendix G. Specifically, for doubly symmetric sections, Appendix F controls when h/t_w is less than λ_r where

$$\lambda_r = \frac{970}{\sqrt{F_{yf}}} \quad (1.1)$$

where F_{yf} is the yield stress of the flange. Otherwise, Appendix G controls.

Since these Appendices were developed independently, no smooth transition exists between them. If two sections are considered: one with a web slenderness that is slightly smaller than λ_r and one slightly larger than λ_r , the

section with the nonslender web can have a significantly larger flexural strength for roughly the same cross section. The difference between Appendix F and G at

$$\frac{h}{t_w} = \frac{970}{\sqrt{F_y}}$$

depends on the particular limit state that controls the strength. A detailed description of the provisions in Appendix F and G are given in the next chapter,

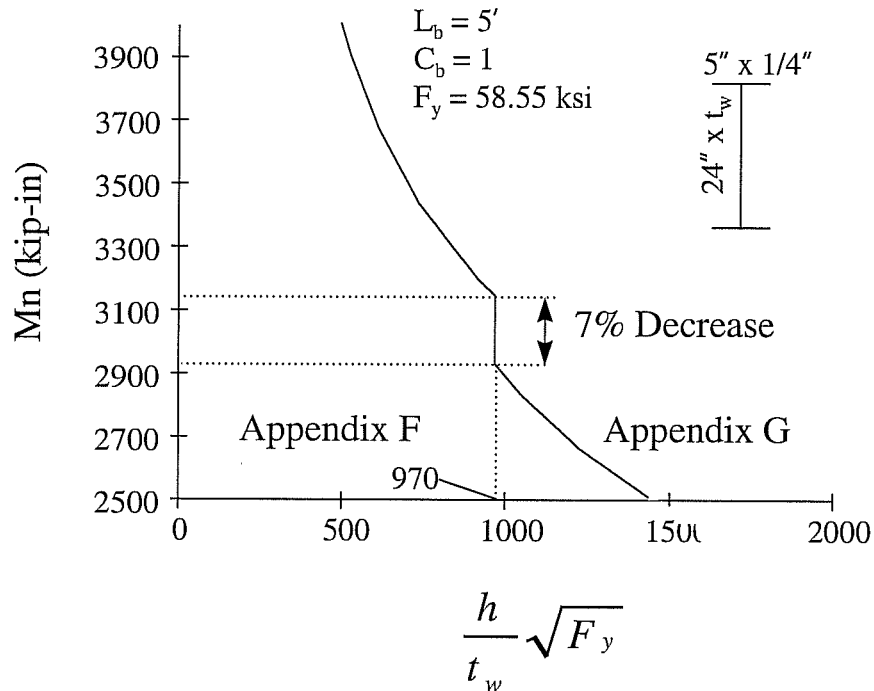


Figure 1.1: Moment Capacity vs. Web Slenderness

but an example of the differences is illustrated in Figure 1.1. This figure shows shows the relationship between the flexural strength and web slenderness ratio for

a constant yield stress. When the web ratio reaches λ_r , the flexural strength drops significantly. This inconsistency needs to be resolved.

This discrepancy can be corrected if the effect of the web slenderness of a beam affects its flexural strength. In order to accomplish this, a wide distribution of web slenderness ratios need to be investigated. By observing the behavior of numerous web ratios in flexure, general and consistent patterns should be found and better strength predictions will follow.

In order to help resolve this issue, an experimental research project was undertaken which is reported herein. Twenty-eight uniform moment tests were conducted on welded built-up sections with five different web-slenderness ratios and two different compressive flange slenderness ratios. Only built-up sections were used so that most cross sectional variables could be held constant while varying the web depth. The unbraced length of the compression flange was also a significant variable. In many instances replicate tests were conducted to examine experimental scatter of the test results. The test program was designed to study the interaction of flange local buckling, web flexural buckling and lateral torsional buckling.

Chapter 2 explains the pertinent background information that is needed to understand the theory supporting this research. Chapter 3 describes the test setup, the variables of each test such as flange slenderness, web ratio, and unbraced length, and material properties. Chapter 4 presents the actual results of the individual tests and observations related to the behavior. In Chapter 5, an inelastic finite element study of some of the test beams is presented along with

comparisons to the test results. Chapter 6 presents the conclusions and recommendations from this research paper.

CHAPTER 2

DESIGN SPECIFICATION

As discussed in Chapter 1, Appendices F and G are organized by the limit states of flange local buckling, web local buckling, lateral torsional buckling and yielding. In this chapter, background material related to these four limit states will be presented. There is more emphasis on the limit state of lateral torsional buckling because the principal variables addressed in the experimental program reported herein was unbraced length.

2.1 YIELDING

The most significant difference in moment capacities between Appendix F and G takes place when the limit state of yielding governs. A flexural member will yield if it lies below the limiting slenderness parameter for a compact element, λ_p . If the slenderness of an element, whether it is flange or web slenderness or the unbraced length slenderness ratio, is less than λ_p , then yielding will govern. This is shown in figure 2.1. The nondimensionalized flexural strengths shown in Figure 2.1 illustrate the typical buckling curve for lateral torsional buckling.

In Appendix F, yielding is based on the plastic moment, $F_y Z_x$, whereas the yield moment, $F_y S_x$, is used for Appendix G. Z_x is defined as the plastic section modulus, and S_x is the elastic section modulus. For rolled sections, the average difference between Z_x and S_x is approximately 12.0%. As the ratio of A_w/A_f increases, the ratio Z_x/S_x also increases. For example, for A_w equal to $2A_f$, the Z_x/S_x is 1.15. However, if A_w/A_f is increased to 6 then Z_x/S_x is about 1.28.

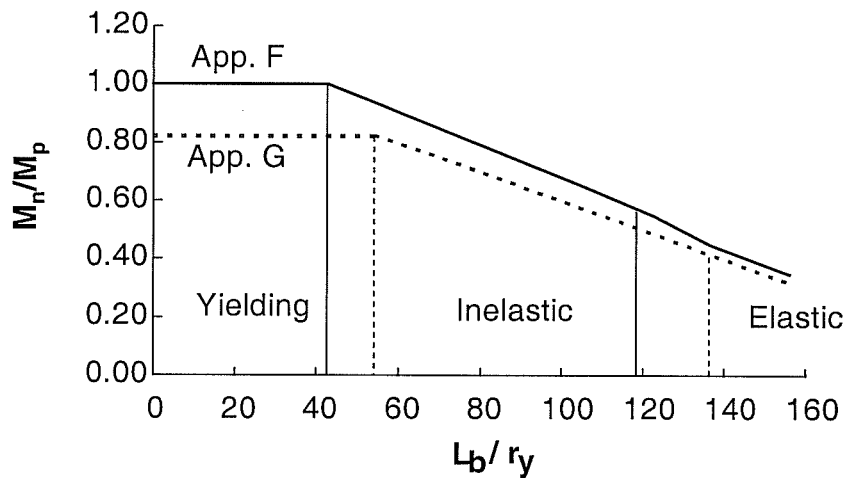


Figure 2.1 Typical Lateral-Torsional Buckling Graph

Another factor that affects the difference in flexural strength between the two appendices for yielding is the hybrid reduction factor (R_e) which is applicable to girders with a higher yield stress in the flange than in the web. This reduction factor, only adjusts the flexural strength of Appendix G. Equation 1, in *Appendix*

I , gives the equation for R_e , which is a function of m , the ratio of the yield stress of the web to that of the compression flange, and a_r , the ratio of the web area to the compression flange area. (The italicized Appendix reference indicates an Appendix at the back of this report.)

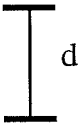
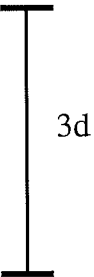
		Section A	Section B
Sect. A 	F_{yf} (ksi)	65	65
	F_{yw} (ksi)	36	36
	S_x (in ³)	13.2	59.61
	Z_x (in ⁴)	15.4	75.2
	m	0.554	0.554
	a_r	2.0	6
	R_e (hybrid)	0.94	0.87
	M_p/M_y (hybrid)	1.05	1.06
	R_e (non-hybrid)	1.0	1
	M_p/M_y (non-hybrid)	1.15	1.26
	Sect. B 		

Figure 2.2: R_e Reduction Factor Comparison

The a_r term is the most influential term in the R_e equation and will account for the greatest difference between the two Appendices. The influence of the R_e term is best understood by an example. Figure 2.2 shows two different sections: A and B. Both sections have flanges made of 5" by 0.2" plate and a web thickness of 0.2". The only difference between the two sections is that Section A has a depth of 10" and Section B's depth is 30".

Both sections will be analyzed first by assuming hybrid properties ($F_{yf} = 65$ ksi and $F_{yw} = 36$ ksi) and then assuming non-hybrid conditions ($F_y = 36$ ksi). The Figure shows that Section B, the more slender section, has a smaller R_e value than A. The R_e section for Section B will reduce the moment capacity by 13.0% ($R_e = 0.87$), but the R_e factor for Section A will only reduce the capacity by 6.0% ($R_e = 0.94$). Thus, the R_e factor becomes more influential as the web area is increased.

Since the R_e factor is dependant upon the ratio of the web yield stress to the flange yield stress, both non-hybrid sections have an R_e factor equal to 1.0. Thus, the R_e factor will have a greater influence for a hybrid section. Figure 2.2 also shows the ratio of the plastic moment to the yield moment, which is a direct comparison of Appendix F to Appendix G. For the hybrid sections, the ratio shows a difference of 5.0% or 6.0%. However, for the non-hybrid sections this difference is increased to 15.0% for Section A and 26.0% for Section B. By observing these results, Appendices F and G are closer together for sections that are considered hybrid. For sections that are non-hybrid, the difference between the two Appendices is increased significantly.

2.2 LATERAL TORSIONAL BUCKLING

Figure 2.1 shows the plastic, inelastic and elastic regions for both Appendices F and G for the limit state of lateral torsional buckling. It is important to understand the significance of these regions in order to fully understand how Appendices F and G are organized. Table 2.1 gives the values of the slenderness parameters (λ , λ_p , λ_r) for both Appendices F and G.

Table 2.1: Limiting Slenderness Parameters for Appendix F and G

Appendix F		Appendix G
$\frac{L_b}{r_y}$	λ	$\frac{L_b}{r_T}$
$\frac{300}{\sqrt{F_{yf}}}$	λ_p	$\frac{300}{\sqrt{F_{yf}}}$
$\frac{X_1}{F_L} \sqrt{1 + \sqrt{1 + X_2 F_L^2}}$ <p>where $X_1 = \frac{\pi}{S_x} \sqrt{\frac{EGJA}{2}}$</p> $X_2 = 4 \frac{C_w}{I_y} \left(\frac{S_x}{GJ} \right)^2$	λ_r	$\frac{756}{\sqrt{F_{yf}}}$

Both values for the limiting slenderness parameter for compact elements, λ_p , are solely dependent upon the yield stress of the flange and have identical

values for Appendices F and G. However, the value for λ_r , the limiting slenderness parameter for non-compact elements, in Appendix F is dependent on various sectional and torsional properties of the member. In Appendix G, λ_r is similar to λ_p in Appendices F and G because it is solely dependent upon the yield stress of the flange for its value.

The lateral buckling slenderness parameter, λ , also varies from one appendix to another. In Appendix F, λ is a function of the unbraced length and the radius of gyration of the member with regard to the y-axis. In appendix G, λ remains to be dependent upon the unbraced length, however, it is nondimensionalized by using r_T as opposed to r_y . This parameter, r_T , is described as the radius of gyration of the compression flange plus one third of the compression portion of the web taken about an axis in the plane of the web. Thus $r_y < r_T$, which explains why λ is always greater in Appendix F than in Appendix G. This is shown in Figure 2.3.

In the past, the lateral torsional buckling behavior of beams has been compared to pure columns. The reason Appendix G uses the r_T term as opposed to the r_y term for the slenderness parameter is because it converts the buckling strength from a critical moment to a critical stress. If the elastic lateral buckling moment found in Appendix F is divided by the section modulus to get stress, the conversion process reduces the cross sectional area of the web by a total of 1/6.

This reduces the value of the radius of gyration accordingly. This conversion process and the derivation of r_T is explained by Tall (1974).

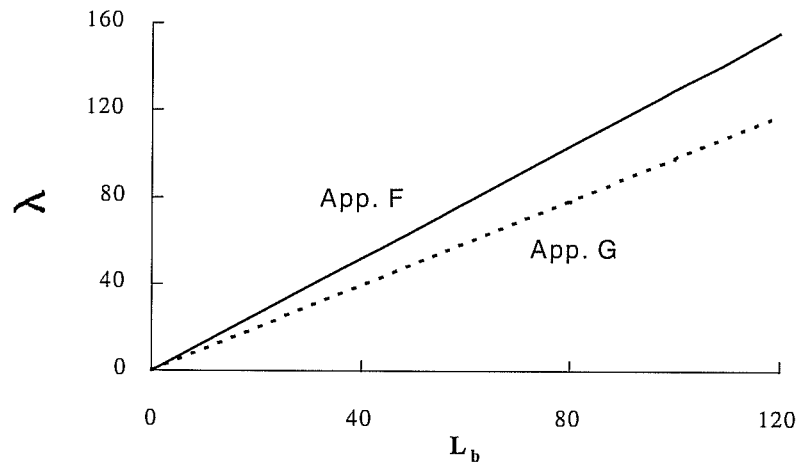


Figure 2.3: Slenderness Parameter vs. Unbraced Length for Both Appendices

In the plastic region ($\lambda \leq \lambda_p$), the governing limit state is either yielding or local web buckling. For yielding, the moment capacity of the section will be equal to the plastic bending moment (M_p) for Appendix F and the yield bending moment for Appendix G (M_y). Since the values of M_p and M_y are independent of the unbraced length, they remain constant until the lateral buckling slenderness ratio exceeds λ_p . When $\lambda_r > \lambda > \lambda_p$, the beam is in the inelastic region. The moment capacity of a specimen in the inelastic region decreases linearly and is

shown as the negative sloped line portion of the plot. In the event that $\lambda_r < \lambda$, the beam will behave elastically.

2.2.1 Elastic Region

If the slenderness parameter, λ , is greater than the limiting slenderness parameter, λ_r , the section is in the elastic region. Many authors have examined the elastic lateral-torsional buckling strength of an I-shaped beam for the uniform moment as well as other common load cases. The elastic lateral torsional buckling capacity (Timoshenko and Gere (1961)) for a W shape is

$$M_{cr} = C_b \frac{\pi}{L} \sqrt{EI_y GJ + \left(\frac{\pi E}{L_b}\right)^2 I_y C_w} \quad (2.1)$$

This equation, which is the elastic buckling equation for Appendix F, is made up of two terms; the warping term $[(\pi E/L_b)^2 I_y C_w]$ and the St. Venant ($EI_y GJ$). The theoretical flexural strength is a function of the square root of the sum of the two squares of these two constants.

The elastic lateral-torsional equations for Appendix F and G have one major difference. Unlike Appendix F, the flexural strength equation for Appendix G just depends on the warping term for its moment capacity. In Appendix G, this warping constant is reduced to a term called the plate girder coefficient or C_{PG} .

To show that the C_{PG} and the Appendix F warping terms are equal, some other variables need to be defined. In Appendix G, by setting the C_b , R_e and R_{PG} terms equal to 1.0, the nominal lateral-torsional buckling strength is

$$M_n = S_x \frac{286,000}{L_b^2} r_T^2 \quad (2.2)$$

The radius of gyration of the compression flange plus one third the compression portion of the web, r_T is equal to:

$$r_T = \sqrt{\frac{I_y/2}{A_f + 1/6 A_w}} \quad (2.3)$$

Finally, S_x will be:

$$S_x = \frac{I_x}{d/2} \quad (2.4)$$

where:

$$I_x = d^2/2 (A_f + 1/6 A_w) \quad (2.5)$$

For S_x , the d term is simply the total depth of the beam, but for I_x , d is the distance between flange centroids. For simplification, these two distances are assumed to be equal.

By making these substitutions, the moment capacity equation is reduced to:

$$M_n = 143000 \frac{dI_y}{L_b^2} \quad (2.6)$$

Neglecting the torsion term in the Appendix F equation yields

$$M_n = C_b \frac{\pi}{L_b} \sqrt{\left(\frac{\pi E}{L_b}\right)^2 I_y C_w} \quad (2.7)$$

where the warping constant C_w is:

$$C_w = \frac{I_y d^2}{4} \quad (2.8)$$

After making these substitutions, the moment equation is reduced to

$$M_n = 143109 \frac{dI_y}{L_b^2} \quad (2.9)$$

The two answers are essentially identical. Thus, the elastic equation for Appendix G is solely dependant upon the warping constant in Equation 2.1. This derivation assumes that the centroid of the flange and the extreme fiber are at the same location. However, this is not the case, because the centroid of the flange and the extreme fiber are separated by a distance equal to half of the thickness of the flange. This distance does, however, seem insignificant.

The reason that Appendix G ignores the St. Venant torsion term in Equation 2.1 for a slender web plate girder is to conservatively account for cross section distortion. The torsion term is a function of J that can be closely approximated using the formula:

$$J \approx \sum \frac{1}{3}bt^3 \quad (2.10)$$

This formula is based on the assumption that the angle of rotation or twist is uniform throughout the entire cross section. For members with compact webs, this assumption is valid, but as the web becomes more and more slender, the angle of twist varies throughout the cross section due to web distortion.

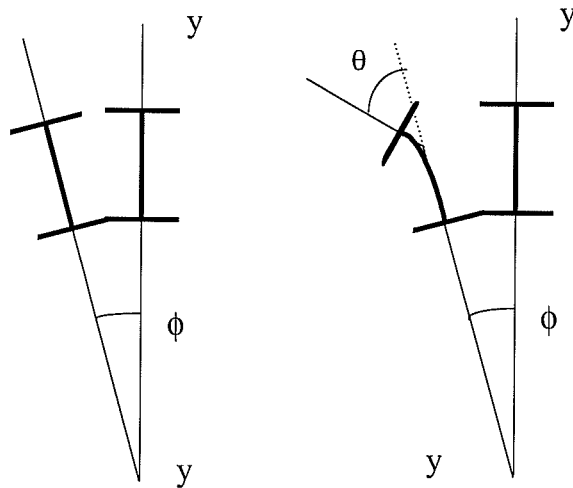


Figure 2.4: Distortion of Slender Web

Figure 2.4 shows a member that has a uniform angle of twist and one that has cross section distortion. Since the cross sectional distortion is difficult to establish, Appendix G simply drops this term and relies solely on the warping constant for the value of the moment capacity.

2.2.2 Inelastic Region

When the slenderness parameter, λ , is greater than λ_p , Appendix F and G require the use of different formulas for the moment capacity. These formulas, for the inelastic region, are listed as Equations 2 and 3 respectively in *Appendix I*. Studies of inelastic lateral-torsional buckling summarized in LRFD have been summarized by Yura, Galambos, and Ravindra (1978).

In the inelastic region, the moment capacity equations for lateral-torsional buckling look similar for both Chapter F and G in LRFD. These formulas are representative of a linear interpolation for all moment capacities where $\lambda > \lambda_p$ thru $\lambda \leq \lambda_r$. The inelastic section is shown in Figure 2.1. Since they were derived from linear interpolations the region is simply a line with a negative slope.

Like the limit state of yielding, the main difference between appendix F and G for the inelastic region is that the moment capacity for appendix F starts at the plastic moment (M_p), but appendix G begins at the yielding moment (M_y). It was noted earlier that $M_p > M_y$ because M_p used the plastic section modulus, Z_x , as opposed to the elastic section modulus, S_x . For $\lambda = \lambda_p$, where the inelastic region begins, the values for the inelastic formulas are equal to that of the formulas for the limit state of yielding, and thus the difference in flexural strength is the same as it is for yielding.

The moment capacity for Appendix F switches from the yielding region to the inelastic region at a shorter unbraced length than Appendix G. The reason for this is that the slenderness ratio, λ , for Appendix F is inversely proportional to the radius of gyration about the y axis, r_y . However, λ for Appendix G is inversely proportional to r_T as observed in Table 2.1. Since r_y is always greater than r_T and λ_p is equal for both Appendices, the value for λ , for Appendix F, will be equal to λ_p at a shorter unbraced length than for Appendix G. This will explain why there is a shift to the side, in Figure 2.1, between the transition points going from yielding to the inelastic region for both Appendices F and G.

2.3 FLANGE LOCAL BUCKLING

Figure 2.5 shows the nondimensionalized flexural strength of both Appendices F and G for the limit state of flange local buckling. The moment capacity shown in the figure is plotted against a varying flange slenderness. The initial plateau is where yielding is the controlling limit state. In this region, the flange slenderness is compact and does not govern. According to the AISC-

LRFD specifications, the compact slenderness parameter, λ_p , for flange local buckling is equal to

$$\lambda_p = \frac{65}{\sqrt{F_{yf}}} \quad (2.11)$$

If the flange slenderness of the beam is greater than λ_p , then flange local buckling will govern in the inelastic range. However, if the flange-slenderness of the beam is less than λ_p , the flange is considered compact and flange local buckling will not control the design. The most notable difference in the capacities between the two Appendices takes place at the yield plateau located at the top part of the graphs.

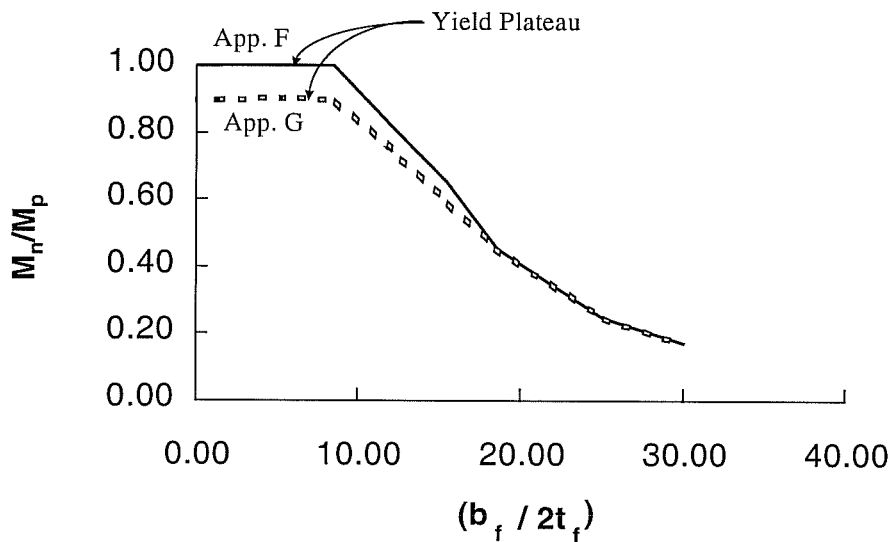


Figure 2.5: Typical Flange Local Buckling Graph

Tests (Johnson 1985) have shown the web slenderness has an effect on the flange local buckling capacity. In LRFD, the interaction is considered by adjusting the elastic flange buckling capacity

$$F_{cr} = \frac{26200k_c}{\lambda^2} \quad (2.12)$$

by the term k_c term, where k_c is

$$k_c = 4\sqrt{\frac{h}{t_w}} \quad (2.13)$$

Figure 2.6 shows the interaction of the web and flange. As the web slenderness increases, k_c increases and the inelastic region gets larger.

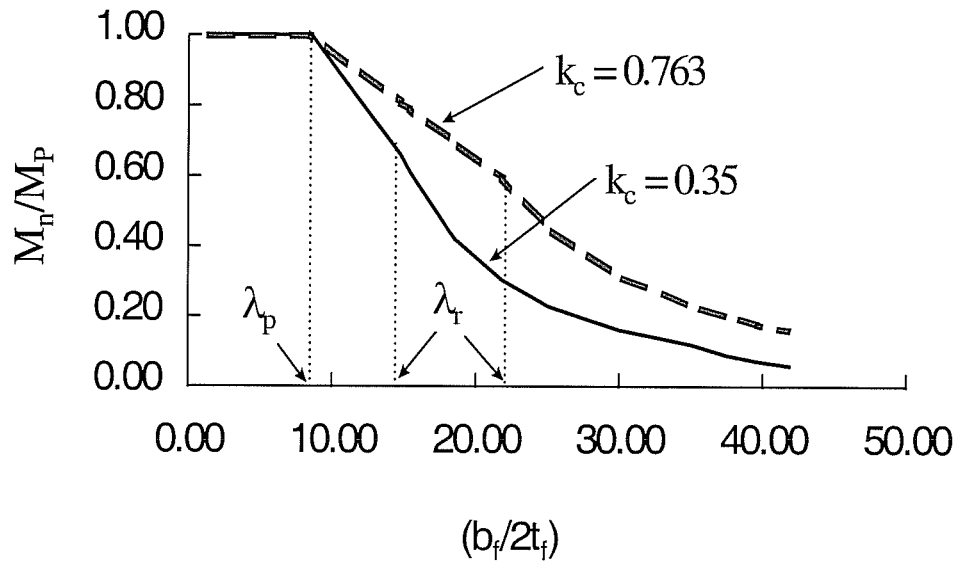


Figure 2.6: Effect of Web Slenderness On Local Flange Buckling

2.4 WEB LOCAL BUCKLING

The flexural strength vs. l relationship for the limit state of web local buckling shown in Figure 2.7 is similar to those shown earlier for flange local buckling and lateral torsional buckling. The inelastic region begins once the λ_p slenderness parameter is exceeded. Appendix F applies for both the yield and inelastic regions. Once the slenderness ratio surpasses the λ_r slenderness ratio, Appendix G applies.

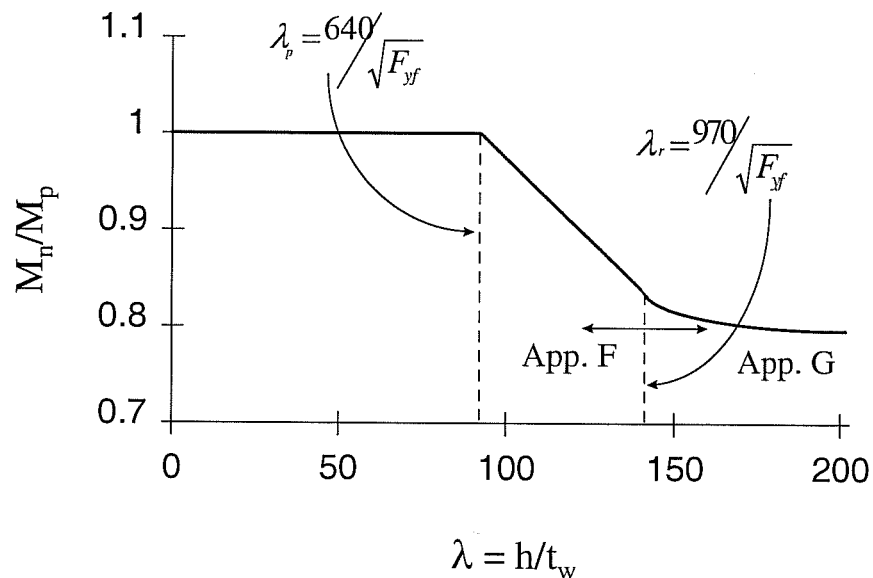


Figure 2.7: Typical Web Local Buckling Graph

In Appendix F, the limit state of web local buckling is handled as an individual limit state and thus has to be checked separately similar to the way

flange local buckling or lateral torsional buckling are checked. However, Appendix G checks the potential for web buckling by assigning a reduction factor, R_{pg} , the plate girder bending strength reduction factor. This reduction factor decreases the yield moment of a section according to its web slenderness. The more slender the web becomes, the greater the flexural strength is reduced by R_{pg} , which is listed as part of Equation 3 in *Appendix I*. This reduction factor was first introduced by Basler (1963). It is mainly dependant upon two parameters for any section, the web slenderness, h/t_w , and the ratio of the web area to compression flange area, a_r . The factor's maximum limit is 1.0 which indicates that the member's flexural strength is not effected by this reduction factor. However, if the factor is less than 1.0, the section's moment capacity is reduced accordingly.

This reduction in the moment capacity occurs because the R_{pg} factor adjusts the stress distribution of the member. Figure 2.8a shows the theoretical and true stress distribution for a typical girder. The true stress distribution is based on past experiments performed with strain gauges.

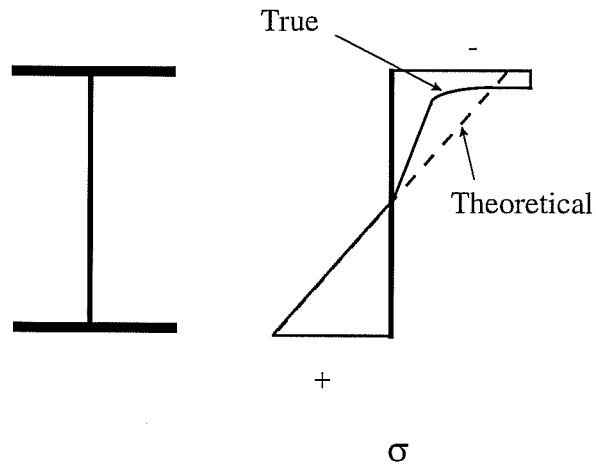


Figure 2.8a: Theoretical and True Bending Stress Distributions

Figure 2.8b shows how Basler reduced the cross section by eliminating a portion of the web in compression. This distribution uses a portion of the web in compression. However, the Basler stress distribution ignores the web from the neutral axis to a distance that is $30t_f$ from the extreme fiber of the compression flange. R_{pg} is simply the ratio of the moment found by using the stress distribution derived by Basler to the actual moment found by the true stress distribution. A more detailed discussion of this reduction factor can be found in Salmon and Johnson.

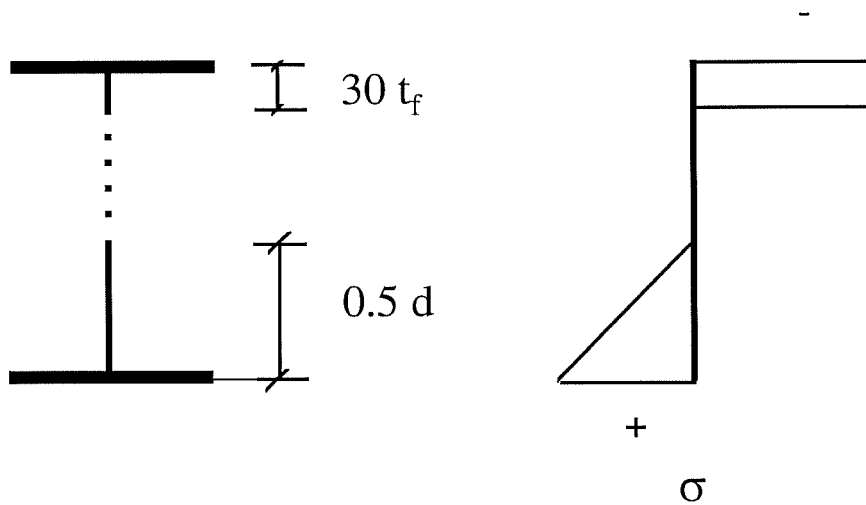


Figure 2.8b: Cross Section And Stress Distribution Assumed By Basler

Figure 2.9 shows how the web slenderness affects the value for R_{PG} . The plot varies web slenderness while keeping the ratio of web area to flange area constant. The reduction factor decreases as the web becomes more slender (h/t_w increases). For this example, the reduction factor in Figure 2.8 has no effect on the moment capacity ($R_{PG} = 1.0$) until h/t_w is greater than λ_r .

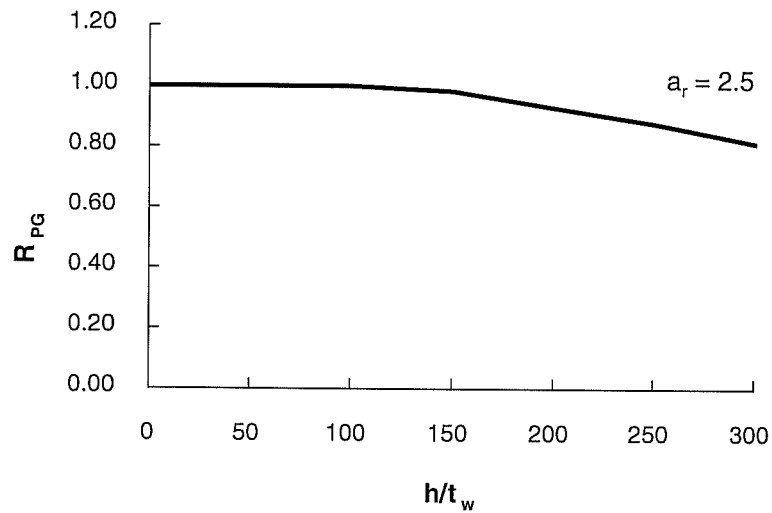


Figure 2.9: Effect of Web Slenderness on The R_{PG} Reduction Factor

Figure 2.10 shows the effect that an increase in a_r , the ratio of the web area to the compression flange area, has on the R_{PG} factor. The value for a_r in Appendix G is limited to a maximum of 10.0. In this plot, the web slenderness and the overall depth was kept constant as a_r was increased. The web area was kept constant while the compression flange width was adjusted. This graph shows that a_r only effects the value of R_{PG} slightly more than 2.0%.

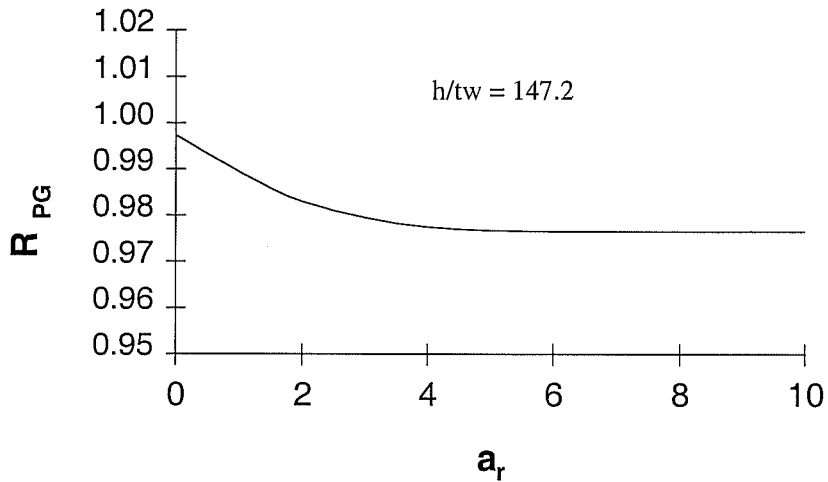


Figure 2.10: Effect of a_r On The R_{PG} Reduction Factor

2.5 RELATED RESEARCH

Some recent studies have been performed to investigate the flexural behavior of built-up sections. Work done by Barth (1996) and Fukomoto (1997) have tried to better predict this flexural strength through the use of numerical models. The following sections will look at both models to asses their accuracy compared to the AISC-LRFD specification.

2.5.1 The Barth Equation

Barth (1996) used mathematical models to try and better predict the flexural strength of steel bridge beams and girders in the inelastic region. In order to predict peak moment behavior, he uses a multi-linear regression model to develop an equation based on inelastic finite element solutions. His equation takes into account both flange and web slenderness and the ratio of the area of the compression flange to the area of the compression portion of the web. This equation is shown as Equations 4a and 4b in *Appendix I*. Barth has the flexural strength of a member dependant on D_{cp} , the compression portion of the web depth; t_w , the web thickness; A_{fc} , the area of the compression flange; and A_{wc} , the area of the web in compression.

Figure 2.11 shows the flexural strength for Appendices F and G for local flange buckling and the Barth Equation with respect to flange slenderness. The flange slenderness was increased so that the A_{fc}/A_{wc} term in the Barth Equation remains constant at a value of about 0.5. The Barth Equation gives predictions close to the LRFD requirements for members with a low flange slenderness, but as this slenderness increases, it grossly overestimates the flexural strength

compared to the AISC specifications. The Barth Equation was designed to be used for fully braced bridge girders that typically have compact or non-compact plate elements, but it should not be used to predict peak moment capacities for girders with non-compact flanges.

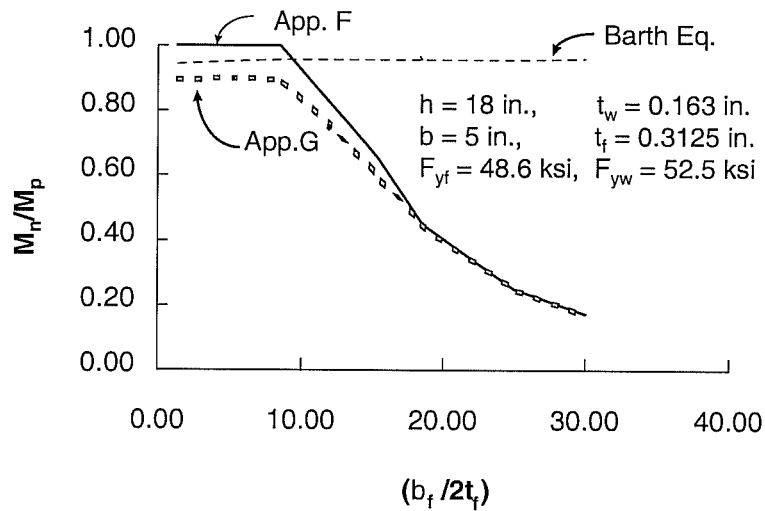


Figure 2.11: Comparison of Barth Equation to AISC-LRFD Specification

Since this equation's accuracy decreases for slender flanges, there should be a limiting flange slenderness ratio. Once this limit is exceeded, use of the equation should not be allowed. A second disadvantage of this equation is that it assumes a fully braced condition. If the member is not fully braced, the equation does not have the capability to adjust for an increased unbraced length.

2.5.2 The Fukumoto Method

Fukumoto (1997) has also published a numerical model to predict the flexural strength of a plate girder. The Fukumoto method is similar to the current LRFD Specification since it considers the various limit states. The failure mode that has the lowest strength controls. These failure modes examine both the ultimate strength of the compression flange and the web. The two failure modes for the compression flange are the lateral buckling strength and the torsional buckling strength. There are three failure modes for the web depending on the location and orientation of longitudinal and transverse stiffeners.

When compared to the LRFD specifications for lateral torsional buckling, the Fukumoto Equation for lateral buckling of the compression flange gives similar predictions. Figure 2.12 shows the Fukumoto Equation plotted against Appendix F and Appendix G for the failure mode of lateral-torsional buckling. The Fukumoto Equation tends to be conservative when compared to both appendices. However, unlike the work of Barth, Fukumoto considers the effect of the unbraced length on a section's flexural capacity while taking into account the effect of the web and flange slenderness. Fukumoto's equation, though

conservative, follows the same general trend as the LRFD, and seems to be a valid alternative for the AISC Specifications.

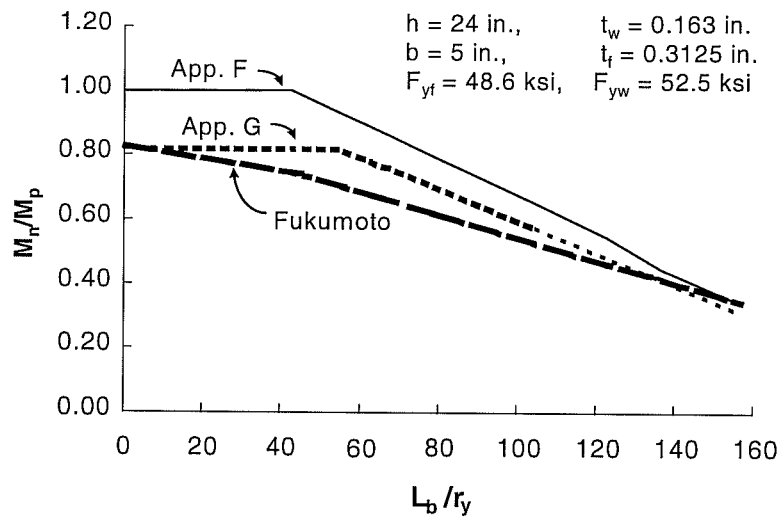


Figure 2.12: Comparison of Fukumoto Equation to AISC-LRFD Specifications

CHAPTER 3

BEAM EXPERIMENTS

3.1 TEST SETUP

The experimental work was conducted at the Ferguson Structural Engineering Laboratory at the University of Texas at Austin.. The test setup, which was the same for all the experiments, was designed so the specimens would be tested under uniform moment and is shown schematically in Figure 3.1. The shear and moment diagrams given by the loading conditions in the

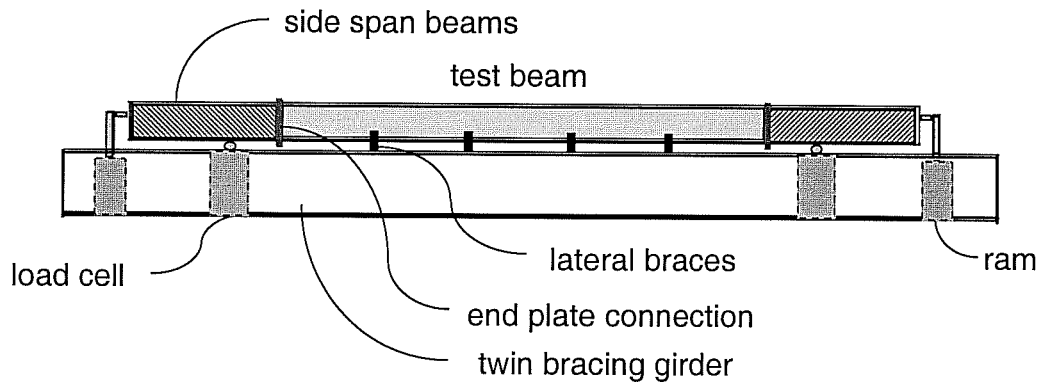


Figure 3.1: Test Setup

setup are shown in Figure 3.2. The presence of shear is limited to the side span beams of the test setup. This prevents any type of shear failure in the test specimen and it also limits the C_b factor to 1.0.

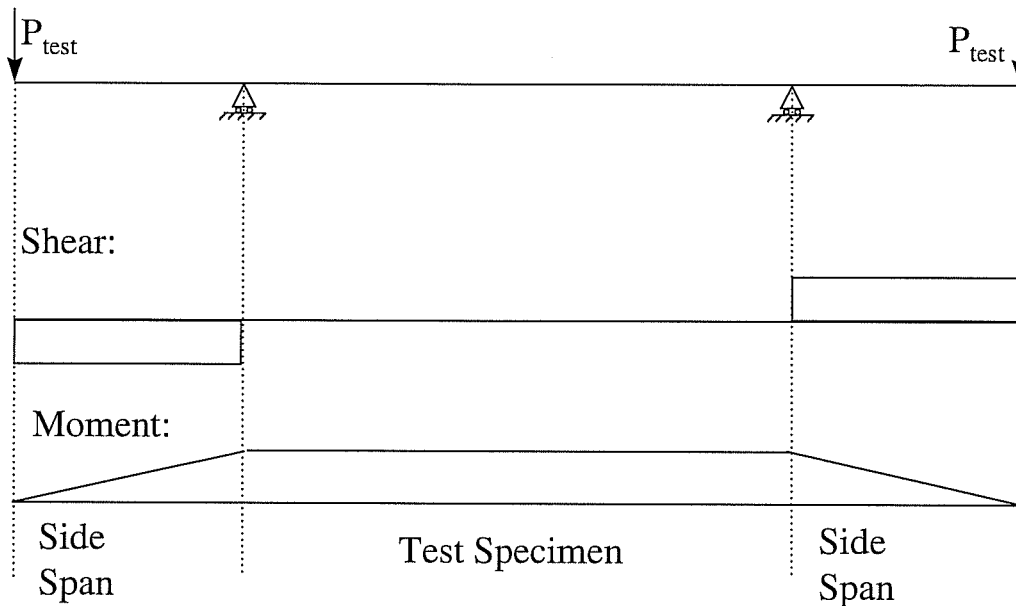


Figure 3.2: Loading Conditions

The test setup also had to accommodate certain design criteria. In order to test all the specimens, a design that allowed for variable beam depth, unbraced length, and flange width had to be configured. This was accomplished by using a creative brace and moment connection design.

By fabricating braces that could easily be adjusted for flange width and a change in unbraced length, labor and preparation time were minimized. One of these braces is shown in Figure 3.3. By clamping onto the top flange of the

bracing girder, which encompassed the test beam, a brace could be attached at any location along the test beam to compensate for any change in unbraced length.

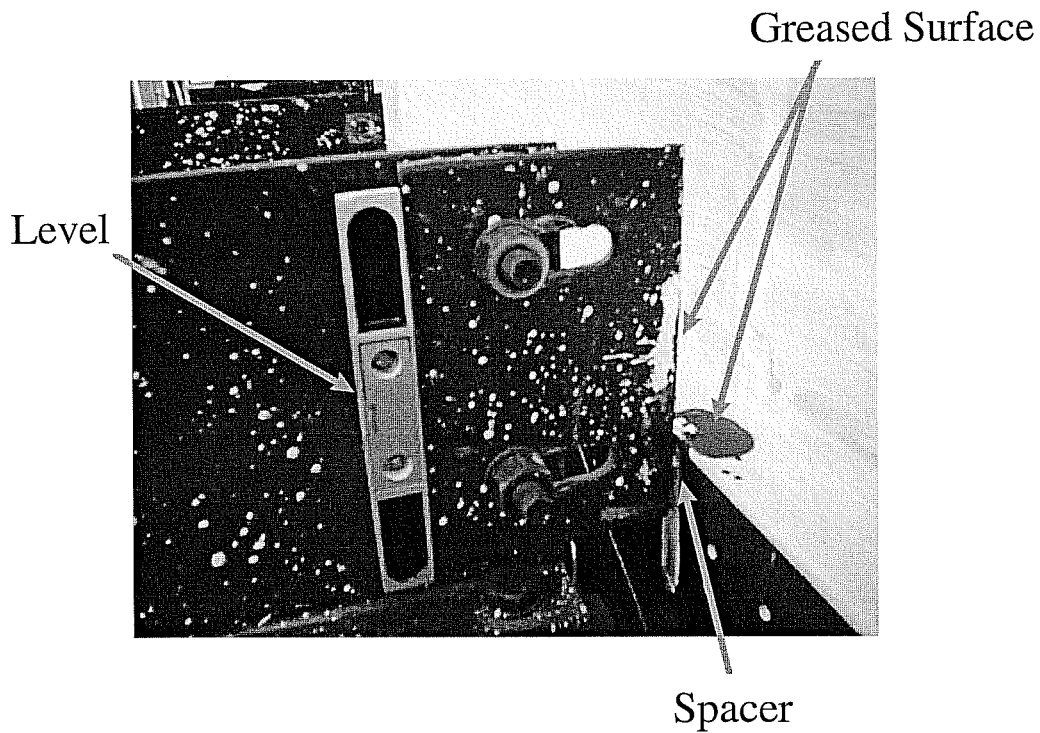


Figure 3.3: Typical Lateral Brace

In order for the test setup to be compatible with an array of varied beam depths, an end plate moment connection was designed that allowed for any of the depths considered. The plate on the side span beam had numerous holes that had a pitch and gage of three inches. The number of rows drilled was a function the range of depths tested. This connection is illustrated in Figure 3.4.

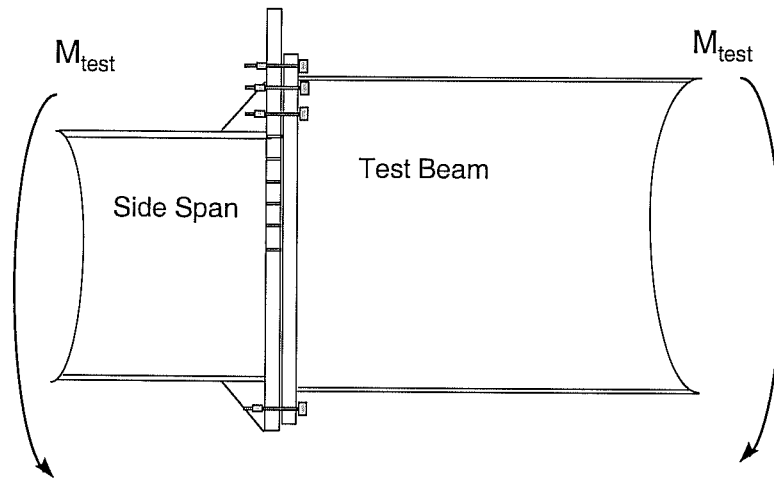


Figure 3.4: End Plate Moment Connection

The hydraulic rams that were used to apply the end loads had a capacity of 100 kips each. Rollers were placed on the inside load cells so that the sidespan beams could pivot freely and account for the large curvatures of the test beams. These rollers, which are shown in Figure 3.5, would alleviate any fixity and ensure a constant moment region throughout the entire length of the test beam. In order to prevent any twisting of the setup, a torsional brace was placed at each reaction load cell. The actual test beam was 25 ft. long and each side span beam was 7.5 ft giving the complete setup a total length of 40 ft.

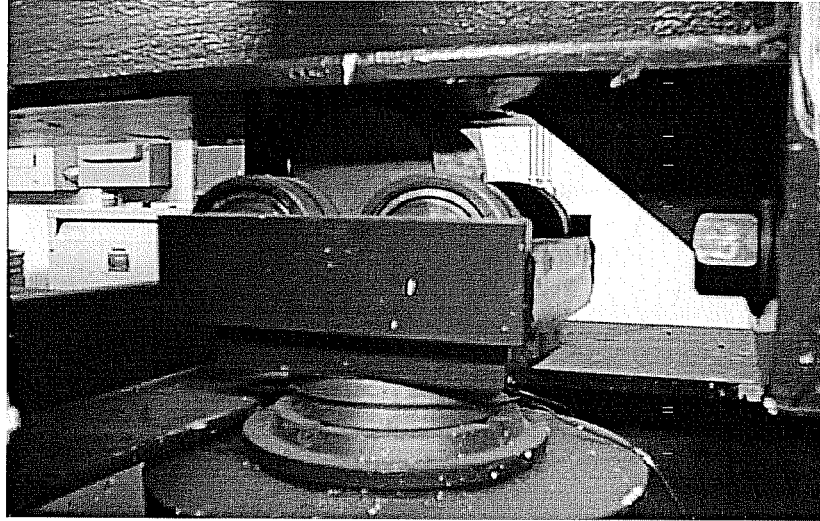


Figure 3.5: Support Roller

3.2 SECTION PROPERTIES

Cross sections were chosen to represent a wide spectrum of slenderness conditions. Flange slenderness and web height were the two main variables distinguishing one cross section from another. Some cross sections were tested with different unbraced lengths to study the interactions of local and lateral buckling.

All dimensions, with the exception of beam height, were measured with a caliper at various points along the beam section. The height of the web was measured with a standard 1/16 in. tape measure. The dimensions of all the test

Table 3.1: Measured Cross Section Dimensions For Test Specimens

Test #	h/t_w	L_b	h	$b_{f(-)}$	$b_{f(+)}$	$t_{f(-)}$	$t_{f(+)}$	t_w
1	73.17	37.5	12.06	4.98	4.99	0.310	0.312	0.163
2	73.17	60	12.00	4.99	5.00	0.313	0.309	0.164
3	91.46	37.5	15.00	4.98	4.99	0.310	0.308	0.162
4	91.46	60	15.06	4.99	5.00	0.313	0.309	0.163
5	109.8	37.5	18.00	4.99	4.96	0.309	0.310	0.163
6	109.8	60	18	4.98	4.99	0.312	0.315	0.163
7	109.8	60	18	4.98	4.96	0.309	0.310	0.164
8	109.8	75	17.92	4.98	4.98	0.309	0.310	0.163
9	109.8	100	17.97	4.98	4.99	0.312	0.314	0.162
10	109.8	100	17.92	4.95	4.97	0.308	0.312	0.163
11	146.3	37.5	24.03	4.98	4.98	0.311	0.310	0.164
12	146.3	60	23.97	4.99	5.00	0.309	0.312	0.163
13	146.3	60	24.03	4.98	4.98	0.310	0.311	0.163
14	146.3	75	23.92	4.97	4.96	0.313	0.315	0.162
15	146.3	75	24	4.96	4.96	0.309	0.310	0.163
16	146.3	100	24	4.98	4.98	0.308	0.309	0.162
17	182.9	37.5	29.96	4.98	4.98	0.311	0.311	0.162
18	182.9	60	30.03	4.95	4.98	0.311	0.312	0.163
19	182.9	60	30	4.97	4.99	0.310	0.310	0.164
20	182.9	75	29.93	4.98	5.00	0.312	0.313	0.163
21	182.9	75	29.97	4.95	4.95	0.309	0.309	0.163
22	182.9	100	30.03	4.97	4.97	0.309	0.312	0.165
23	109.8	90	18.06	5.93	5.93	0.254	0.255	0.161
23	109.8	110						
24	109.8	100	18.03	5.99	5.98	0.257	0.254	0.161
25	146.3	100	24.09	5.99	6.00	0.253	0.254	0.164
26	146.3	100	24.03	6.00	5.97	0.254	0.253	0.16
27	182.9	100	30.03	5.98	6.00	0.254	0.255	0.162
28	182.9	100	30.06	6.00	5.99	0.252	0.252	0.163

- h Web Height (inside to inside of flanges)
- $b_{f(-)}$ Flange width compression side
- $b_{f(+)}$ Flange width tension side
- $t_{f(-)}$ Flange thickness compression side
- $t_{f(+)}$ Flange thickness tension side
- t_w Web thickness

cross sections are reported in Table 3.1 as the averaged value of all the measurements taken along the cross section. For convenience, these tests were assigned a specific “Test Number” that will be referenced to in later chapters. The nominal web thickness was the same for all girders.

There were a total of five web slendernesses that were tested as shown in Figure 3.6. The least slender web, which measured 12 in., fell into the compact

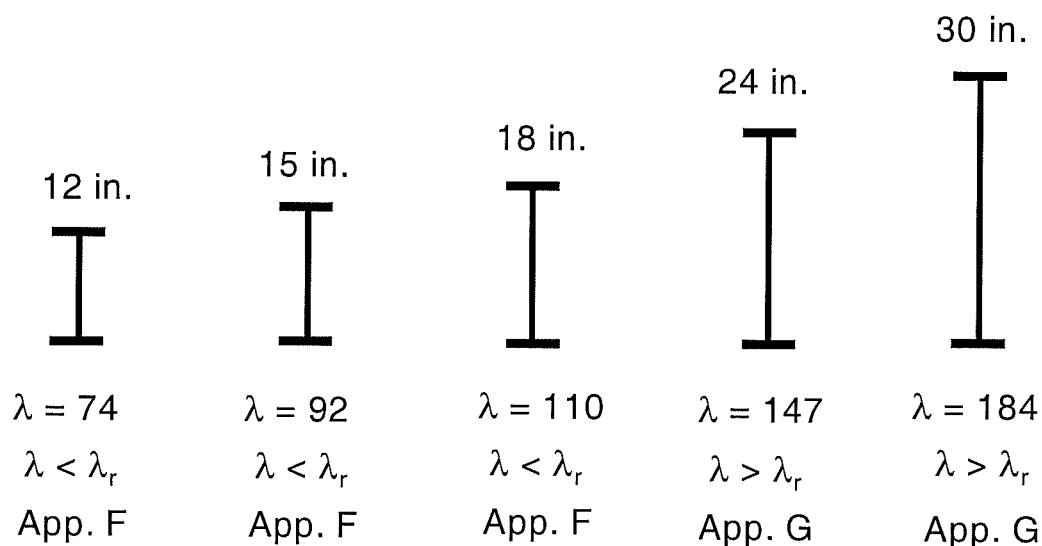


Figure 3.6: Depths Investigated

category which requires the use of Appendix F in LRFD to predict its flexural strength. Based on an assumed yield point between 50 ksi to 60 ksi, both the 15 in. and 18 in. depths were noncompact thus requiring the use of Appendix F for analysis, while the 24 in. and 30 in. webs were considered slender when compared to the λ_r parameter, thus requiring Appendix G. By testing all five web

ratios, the effect of web slenderness on the flexural strength of a member could be better understood.

There were two different flange widths tested; a 5 in. and 6 in. as seen in Figure 3.7. The 5 in. flange was compact so local flange buckling was not

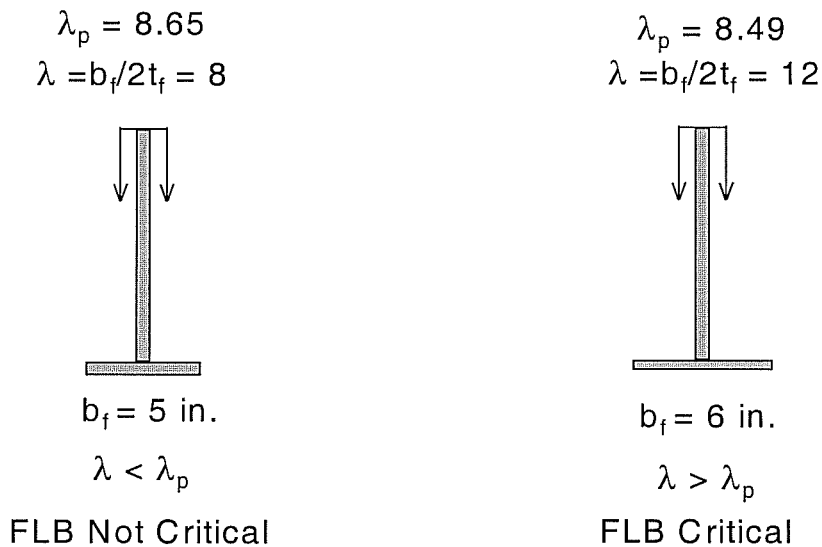


Figure 3.7: Flange Widths Investigated

expected to control the behavior of these girders. Thus, the beam would either fail from yielding, lateral torsional buckling or local web buckling. These sections were chosen to investigate the relationship between unbraced length and web slenderness, and to hopefully see how these two variables interact. All of the unbraced lengths for these sections are shown in Figure 3.8.

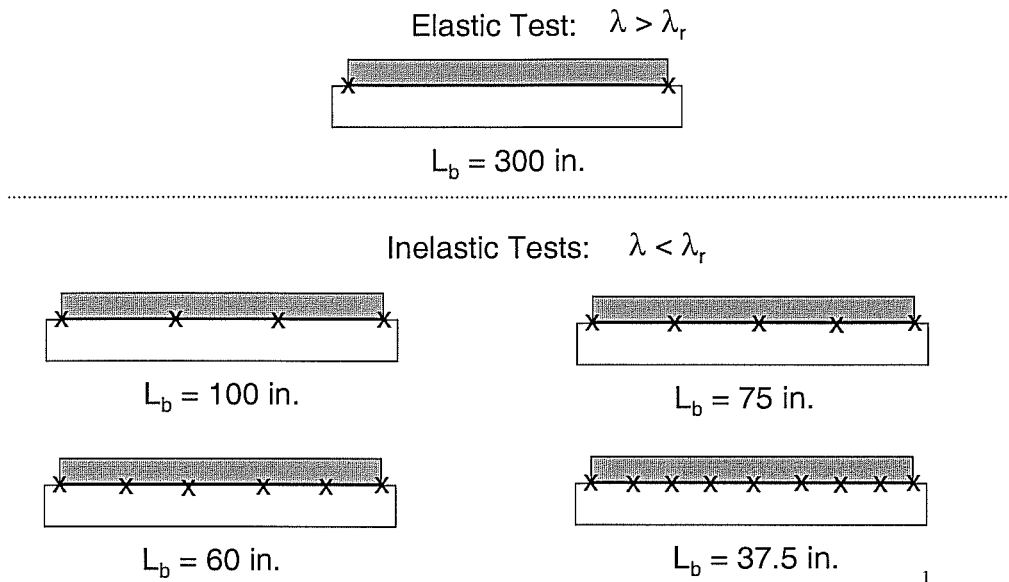


Figure 3.8: Unbraced Lengths Investigated

The 5 in. flange beams were first tested elastically using a 300 in. unbraced length test. The 18 in., 24 in. and 30 in. depths were then tested in the inelastic range ($\lambda_p < \lambda < \lambda_r$) at an unbraced length of either 37.5 in, 60 in., 75 in., or 100 in. unbraced lengths. The 15 in. and 12 in. depths were tested only at 60 in. and 37.5 in. The 37.5 in. Unbraced length was less than L_p , the plastic limit for unbraced length, so lateral buckling would not be expected and the girder would be in the plastic region as discussed in Chapter 2. Since the 12 in. beam had compact flanges and a compact web, the plastic moment was expected.

As shown in Figure 3.7, the 6 in. flange had a flange slenderness that was noncompact making it susceptible to localized buckling of the flange (Tests 23-28). These sections were chosen to try and find any correlation between the web slenderness of a beam and its resistance to local flange buckling. Since the

beam's failure mode was flange local buckling and not lateral torsional buckling, they were only tested at an unbraced length of 100 in. This was a short enough length to force the beam to locally buckle in the compression flange.

3.3 MATERIAL PROPERTIES

The material properties of the flanges and webs of the welded sections were not constant. Since the mill reported all plates in a particular shipment were from the same steel, only random coupon tests had to be performed to gain an understanding of the strength of the material for that particular shipment. There were a total of three shipments of beams : the non-compact flange sections; the compact flange sections with depths of 30 in., 24 in. and 18 in.; and the compact flange sections that had depths of 15 in. and 12 in. For all of the beams in a shipment, the flanges had the same yield strength and the webs also had the same yield strength.

In order to determine the material properties for all the beams, Standard ASTM A370 tension tests were performed on samples taken from randomly selected beams. Three static yield stress readings were taken from each coupon and the averaged values are listed in Table 3.2a. The corresponding values of

Table 3.2a: Material Properties

	Area	Percent Elongation	Static Yield	Ultimate Stress
	in ²	%	ksi	ksi
Top Flange	0.379	22.7	58.4	82.2
Bottom Flange	0.379	24.1	58.7	83.2
Web	0.250	23.6	51.7	73.9
5 in. Flange Beams (h = 24 in. and 30 in.)				
Top Flange	0.460	22.8	48.7	76.6
Bottom Flange	0.462	25.0	48.4	75.3
Web	0.243	21.3	52.5	73.0
5 in. Flange Beams (h = 15 in. and 12 in.)				
Top Flange	0.460	23.0	61.1	86.8
Bottom Flange	0.462	24.0	60.8	86.6
Web	0.243	23.4	58.6	72.4

Table 3.2b: Applicable Appendix For Various Web Ratios

Web Depth	h/t_w	F_{yf} (ksi)	Limit λ_p	Limit λ_r	$(h/t_w)/\lambda_p$	$(h/t_w)/\lambda_r$	Current Category
5 in. Flange							
12	73.17	64.4	79.8	120.9	0.92	0.61	App. F
15	91.46	64.4	79.8	120.9	1.15	0.76	App. F
18	110	48.6	91.8	139.2	1.20	0.79	App. F
24	146.3	48.6	91.9	139.2	1.59	1.05	App. G
30	182.9	48.6	91.9	139.2	1.99	1.31	App. G
6 in. Flange							
18	109.8	58.6	83.6	126.8	1.31	0.87	App. F
24	146.3	58.6	83.6	126.8	1.75	1.15	App. G
30	182.9	58.6	83.6	126.8	2.19	1.44	App. G

the slenderness parameters resulting from these measured values are listed in Table 3.2b for each group of beams. The coupon tests verified that the two flanges of each test specimen were fabricated from the same heat of steel.

3.4 DATA ACQUISITION AND TESTING TECHNIQUES

All tests monitored nearly identical data which consisted of load, lateral and in-plane displacement, hydraulic pressure in the system and midspan strain. The load was measured by a total of four different load cells. There was a shear pin load cell at each hydraulic ram that measured the amount of shear transferred from the ram to the side span beam. Two reaction load cells measured the compressive force applied at each reaction located 7 ft. in from the ram. After examining the data, it was decided that the true test load was best represented by taking the average of the compressive load cell readings. A pressure transducer was placed between the pump and the rams so that the pressure could be monitored within the system. By multiplying this pressure by the ram's piston area, a load could be calculated. It should be noted that this calculated load does not consider friction within the system.

Deflections were monitored with the use of LVDT's or linear potentiometers. These pots used voltage to allow the data acquisition system to convert any lateral or in-plane movement to a measured distance. There were two linear pots located at the ends of the setup near the hydraulic rams and a third located at the midspan of the test beam. All of the linear pots were used to detect

any in-plane movement in the system as the load was increased. A string potentiometer was placed at the compressive flange of the midspan of the centermost unbraced length to monitor the maximum lateral movement of this flange.

Strain gauges were placed at the midspan of the test beam to monitor the bending stress. These gauges were placed at the extreme fibers of the beams so that the maximum tensile and compressive stresses may be calculated. Distortion of the web in compression could be determined by observing the variation of the compressive stress relative to the tensile stress.

3.4 Experimental Procedures

Before a beam was bolted into the setup, a four foot level was used to assure that both side span beams were level. This guaranteed that the setup was symmetrical with no additional initial displacements on one side relative to the other. Once the sidespans were ready, the test beam was fastened to the setup by its end plate connections. To assure rigidity and reduce slip, all bolts were fastened using an impact wrench. These bolts were standard ASTM A 325 with a diameter of 7/8 in. The impacting of the bolts at the end plate connection is illustrated in Figure 3.9.

Once the test beam was fully bolted to the side spans and all the measurements were taken, a lime and water mixture was applied to all surfaces of the test beam. This lime mixture was used to visually detect yielding.

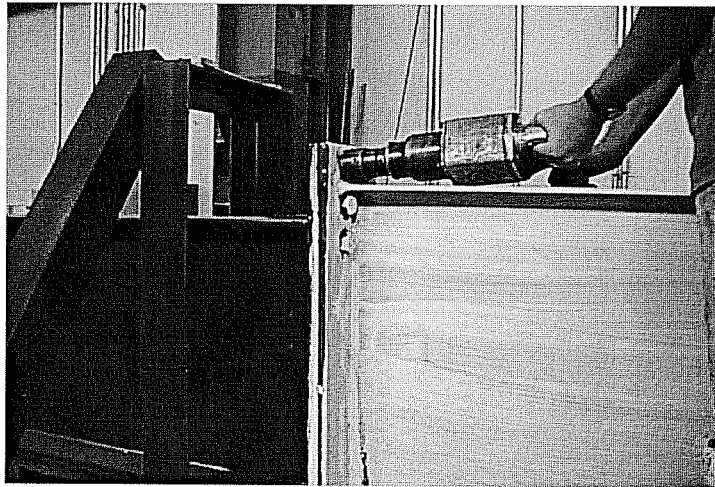


Figure 3.9: Tightening Of Bolts On Moment Connection Using Impact Wrench

The braces were then fastened in their proper location to the flanges of the bracing girders. These braces were made out of T-sections which were inverted and fastened to the bracing girders with clamps. These braces had slotted holes so that they could be adjusted to compensate for the varying flange slenderness of the beam. Like the end plate connection, the bolts used to fasten the braces were also impacted. To affirm that these braces would only provide lateral support and not

restrict any in-plane movement, a torpedo level was used to certify that the brace would touch the compression flange at a right angle. To try and reduce the amount of friction in the braces its contact surface was coated with oil and all the braces on one side of the setup had an initial spacing of 1/32 in. separating it from the test beam. These preparations are shown in Figure 3.3.

Two plotters continually monitored loads from a load cell and the midspan and lateral deflections, respectively so that peak load could be recorded. When a test began, electronic data was initially recorded at a load increment of about 2.0 kips (observed on the plots) until initial yielding was detected. To ensure consistency, the lateral displacement was also measured manually with the use of a transit at every four load increments. Once initial yield was detected, load increments were based on deflection. All beams were tested until stiffness was lost and a maximum “peak” load could be seen by both plots.

CHAPTER 4

TEST RESULTS

In section 4.1, the general behavior which was common to all tests is described. Specific results of each test are presented in the subsequent sections along with comparisons to the AISC-LRFD provisions.

4.1 GENERAL BEHAVIOR

For all tests recorded the load vs. in-plane deflection and the load vs. lateral deflection response was recorded and the results for all tests were similar. Typical load vs. in-plane and lateral deflection plots are shown as Figures 4.1 and Figure 4.2 respectively. These specific plots are taken from Test 2 which was the 18 in. deep compact flange section that was tested at an unbraced length of 60 in. Both load vs. deflection plots start in the elastic region. Then a loss of stiffness takes place at the load point labeled first yield. This loss of stiffness continues until the ultimate load of the section is finally reached. All load vs. in-plane and lateral deflection plots are shown in *Appendix II* in the back of this paper.

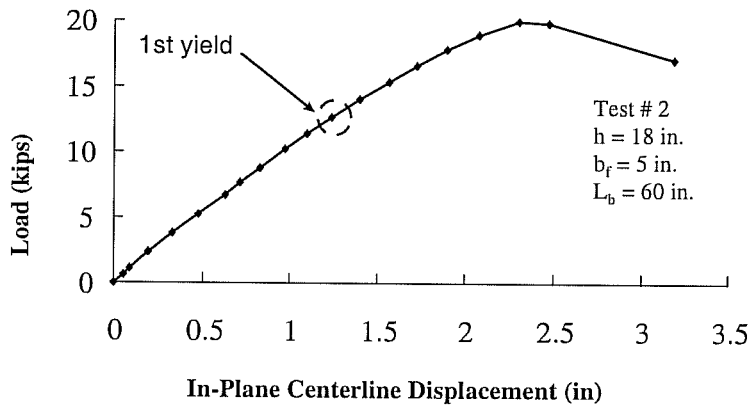


Figure 4.1: Typical Load-In-Plane Displacement Curve

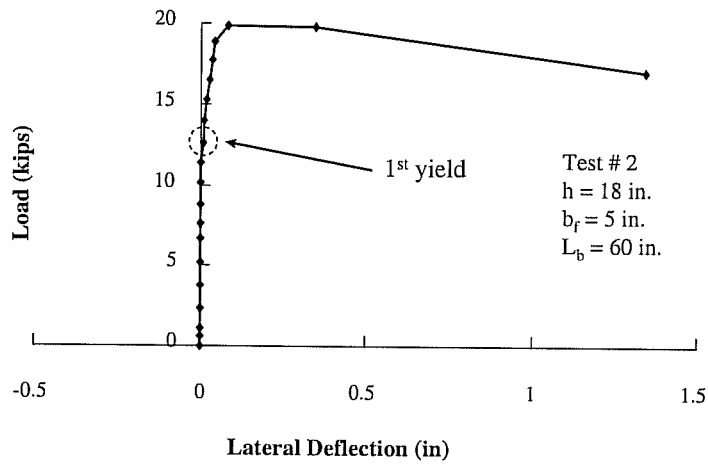


Figure 4.2: Typical Load-Lateral Displacement Curve

When testing all of the sections, the yielding pattern that formed looked very similar for every beam. This typical yielding, shown as Figure 4.3, has yield lines at 45° from the centerline of the test beam. From Mohr's Circle, it is known that the maximum shear takes place at a 45° plane which explains the orientation of the pattern illustrated in Figure 4.3.

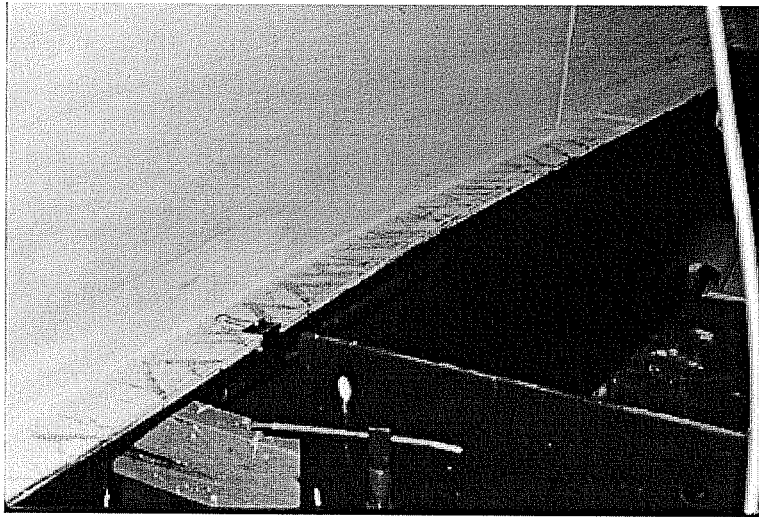


Figure 4.3: Typical Yield Pattern

For all of the tests, this yielding first appeared in areas of high residual stress such as web and flange splices and at the welds which connected the flange to the end plates. On all of the beams that were tested with a web splice, the first sign of yielding was noticed on the compression flange adjacent to the splice. This initial yielding is shown as Figure 4.4. Yielding due to the residual stresses in the beam would appear at about 30% of the ultimate load of the member, and would continue to grow during the duration of the test. With the exception of a

slight loss of stiffness, this initial yielding had little effect on the performance of the member.

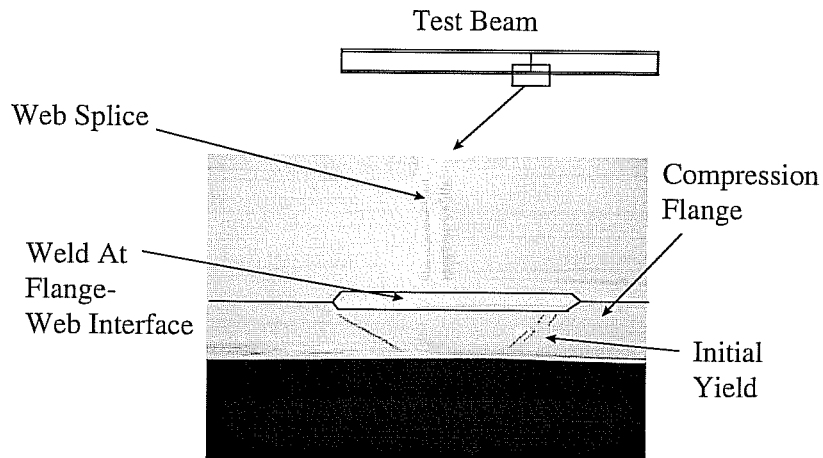


Figure 4.4: Initial Yielding On Compression Flange Adjacent To Web Splice

During the tests, it was very common for the beam to create a loud popping sound which was indicative of “oil canning” taking place. This oil canning causes noticeable undulations of the web along the length of the beam. Figure 4.5 shows the web after these waves are formed. When the popping and undulations did occur, there appeared to be no effect on the stiffness of the beam. The oil canning was present on all of the depths that were tested, but it was most pronounced on the 30 in. beam.

The strain gauges were used to examine how close the compressive stress and the tensile stress were equal at the extreme fibers. These gages showed that most tests had extreme fibers that were about equal for the first 50% of the peak

load. After the first half of the buckling load was applied, these stresses would begin to deviate. The difference between the two stresses greatly depended upon the depth of the web. The 30 in. deep girder had the greatest difference of about 20.0%, while the 12 in. had stresses which were only about 10.0%. As the web got more slender, the difference between the extreme fiber stresses would increase. An explanation for this could be attributed to more web distortion present in the more slender girders.

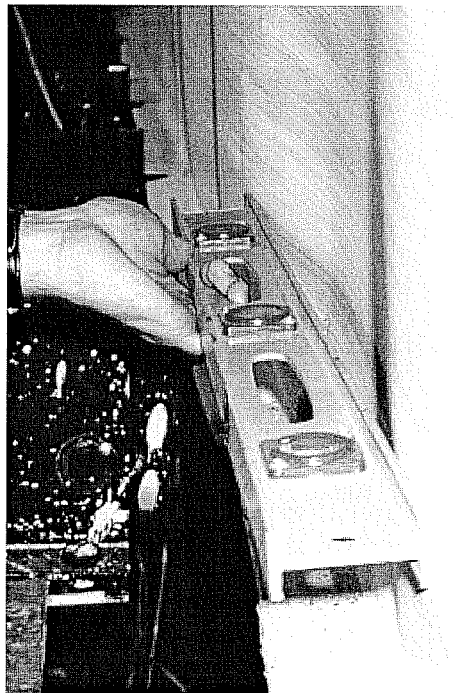


Figure 4.5: Oil Canning of 30 in. Web

4.2 COMPACT FLANGE TESTS

In this section, the results of all the compact flange sections that failed by lateral-torsional buckling are reported. These test results are organized according to the web depth and the numerical results are reported in Table 4.1. The material properties and the applicable AISC Appendix, F or G, are reported in Table 3.2a and Table 3.2b for each test.

4.2.1 Tests 17-22, 30 in. Web

Six Tests were conducted with unbraced length as the only variable. Four different unbraced lengths were considered: 100 in., 75 in., 60 in. and 37.5 in. Replicate tests were conducted with the 60 in. and 75 in. unbraced lengths to establish the degree of experimental scatter. The experimental maximum loads are shown in Figure 4.6 along with the AISC-LRFD design strength provisions for Appendices F and G. The flexural strength is nondimensionalized by the girder's plastic moment, and the unbraced length, L_b , is nondimensionalized by the, r_y , radius of gyration in the y direction.

Besides the fully braced test ($L_b/r_y = 41$), all of the beams in this section failed by a lateral-torsional buckling which is what LRFD predicted. Figure 4.7 shows a typical lateral torsional buckling failure, Test 22, $L_b=100$ in. Both the front and back views of the buckle are shown to provide a better understanding of the mode shape that the section buckled into upon reaching its ultimate capacity. Although three braces are shown in the picture, only two were active

Table 4.1: Results of Compact Flange Tests

Test Number	h	h/t _w	b/t _f	L _b	P _{WLB(F)} (kips)	P _{FLB(F)} (kips)	P _{LTB(F)} (kips)	P _{FLB(G)} (kips)	P _{LTB(G)} (kips)	P _{TEST} (kips)	P _{TEST} /P _{AISC}	M _{test} kip*in	M _{test} /M _p	Failure Mode
1	12	73.6	8	37.5	****	18.1	18.1	15.3	16.3	17.51	0.967	1471	0.97	WLB, Then LTB & FLB
2	12	73.6	8	60	****	18.1	16.6	15.3	15.3	16.04	0.966	1347	0.89	LTB
3	15	92	8	37.5	22.4	23.8	23.8	20.5	21.3	22.65	1.011	1903	0.95	WLB, Then LTB & FLB
4	15	92	8	60	22.4	23.8	21.5	20.5	19.8	19.45	0.905	1634	0.82	LTB
5	18	109.8	8	37.5	23.4	24.8	24.8	23.1	21.2	21.29	0.909	1788	0.86	WLB, Then LTB & FLB
6	18	109.8	8	60	23.4	24.8	22.8	23.1	20.4	19.80	0.870	1663	0.80	LTB
7	18	109.8	8	60	23.4	24.8	22.8	23.1	20.4	19.55	0.859	1642	0.79	LTB
8	18	109.8	8	75	23.4	24.8	20.7	23.1	18.5	18.59	0.897	1562	0.75	LTB
9	18	109.8	8	100	23.4	24.8	17.4	23.1	15.3	17.09	0.985	1436	0.69	LTB
10	18	109.8	8	100	23.4	24.8	17.4	23.1	15.3	16.98	0.979	1426	0.68	LTB
11	24	146.3	8	37.5	****	36.6	36.6	32.2	30.5	28.41	0.932	2386	0.77	WLB, Then LTB & FLB
12	24	146.3	8	60	****	36.6	32.7	32.2	28.9	26.82	0.930	2253	0.73	LTB, Then WLB
13	24	146.3	8	60	****	36.6	32.7	32.2	28.9	26.58	0.921	2233	0.72	LTB
14	24	146.3	8	75	****	36.6	29.5	32.2	26.1	23.91	0.917	2008	0.65	LTB
15	24	146.3	8	75	****	36.6	29.5	32.2	26.1	24.67	0.946	2072	0.67	LTB
16	24	146.3	8	100	****	36.6	24.1	32.2	21.3	22.25	1.046	1869	0.61	LTB
17	30	182.9	8	37.5	****	50.3	50.3	38.0	38.0	35.36	0.931	2970	0.70	WLB, Then LTB & FLB
18	30	182.9	8	60	****	50.3	43.8	38.0	36.1	33.21	0.919	2790	0.66	LTB
19	30	182.9	8	60	****	50.3	43.8	38.0	36.1	34.07	0.943	2862	0.68	LTB, Then WLB
20	30	182.9	8	75	****	50.3	39.0	38.0	32.8	31.41	0.959	2638	0.61	LTB
21	30	182.9	8	75	****	50.3	39.0	38.0	32.8	30.69	0.937	2578	0.61	LTB
22	30	182.9	8	100	****	50.3	31.1	38.0	27.1	27.54	1.017	2313	0.55	LTB

* Measured F_{yr} = 58.55 ksi for b/t_f = 12; F_{yf} = 48.6 ksi for b/t_f = 8 (h=30 in., 24 in., 18 in.); F_{yf} = 61.0 ksi for b/t_f = 8 (h=15 in., 12 in.)
 * Measured F_{yw} = 51.7 ksi for b/t_f = 12; F_{yw} = 52.5 ksi for b/t_f = 8 (h=30 in., 24 in., 18 in.); F_{yw} = 58.6 ksi for b/t_f = 8 (h=15 in., 12 in.)
 * Values For Both Appendix F & G Assume k = 1

* FLB = Flange Local Buckling

* WLB = Web Local Buckling

* LTB = Lateral Torsional Buckling

* Number In Bold Indicates Failure Mode = P_{AISC}

**** = Does not apply

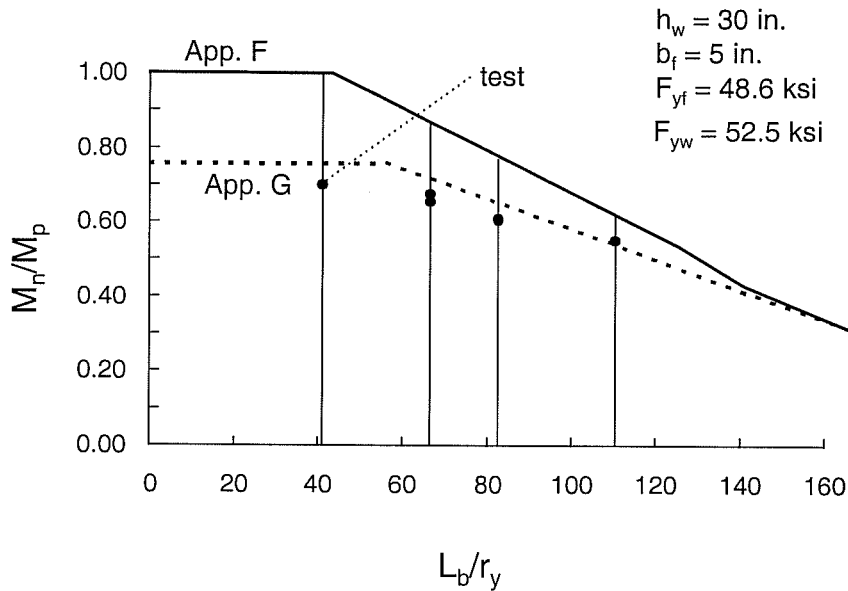


Figure 4.6: Test Results for 30 in. Deep Girder

in the test. The third brace, shown in the middle, was simply used to limit the lateral movement of the beam upon failure so that deflection instrumentation would not be damaged. For all of these tests, the largest lateral movement occurred at the mid span of the middle unbraced length. The unbraced length nearest the center of the test span was the most critical because it had the least lateral end restraint (effective length factor, $k=1.0$). Similar unbraced lengths near the end plate would be less critical because of the restraint provided by the elastic end spans.

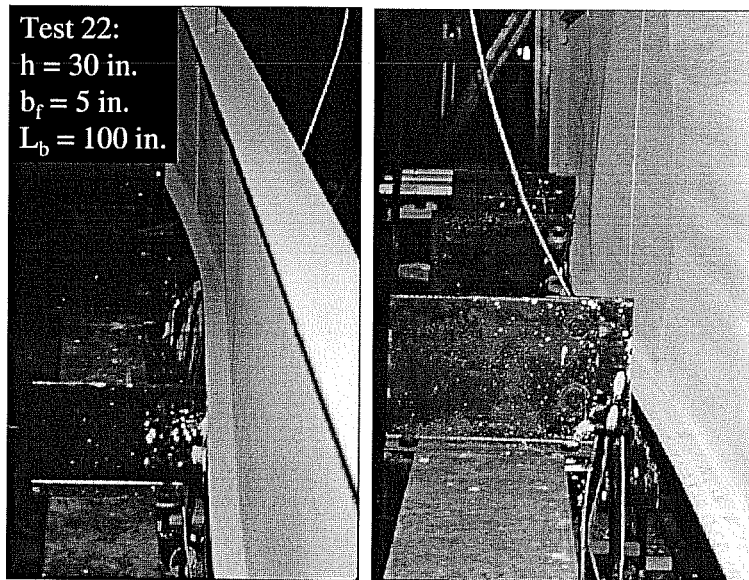


Figure 4.7: Lateral Torsional Buckle of 30 in. Deep Specimen

In all of the 30 in. deep specimens, a web cripple developed at the end plate connection. This crippling of the web both in its initial and final stages is shown in Figure 4.8. The web typically began to buckle at about 40% - 60% of the ultimate flexural load. The buckle would initially form at the compression flange end plate interface and would continue to grow up the web to the neutral axis as the load was increased.

This web buckle was caused by the large compression flange force of the side span bearing on the thin web of the test specimen as shown in Figure 4.8. The side span's compression flange is offset about 3 in. from the compression flange of the test beam. Thus, the side span's flange is directed into the web of the test beam. This flange force was intended to be more evenly distributed by the

$\frac{3}{4}$ in. thick end plates. However, the web still buckled in spite of the fact the web crippling provisions in Chapter K of LRFD were satisfied. These web buckles at the end plate connections did not affect the way that the beam failed, but did reduce the in-plane stiffness once they were initiated.

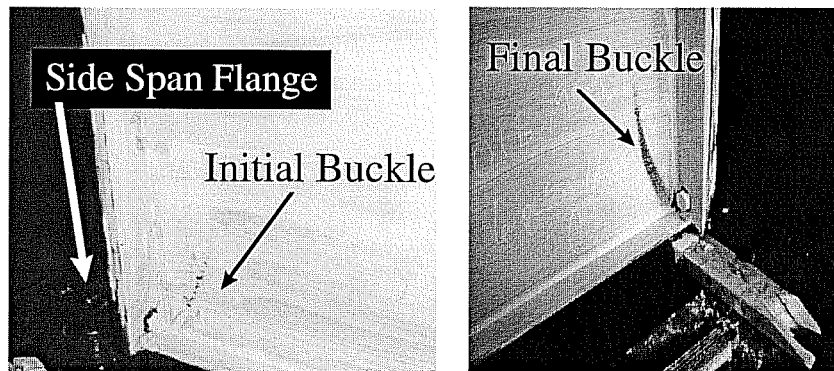


Figure 4.8: Web Cripple of 30 in. Girder At End Plate Connection

At the maximum load level, the severe twisting of the tension flange occurred. This was caused by the lateral movement of the compression flange and the web buckling due to flexure. This twisting is shown in Figure 4.9. The twisting of this tension flange was present on all of the beams tested, but it was most easily observed on the 30 in. specimens.

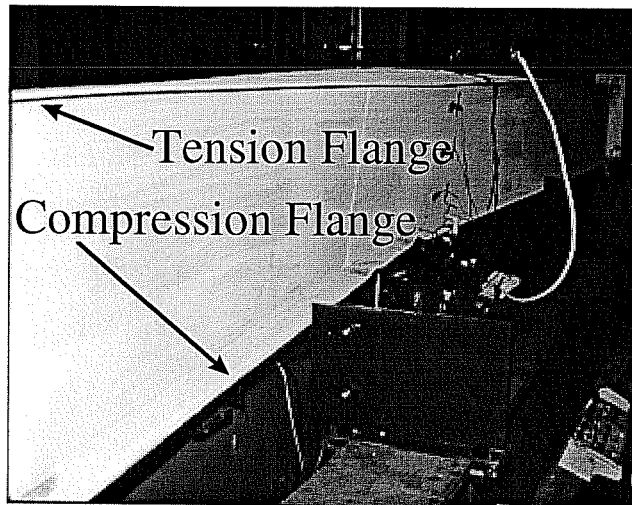


Figure 4.9: Twisting of Tension Flange

From Figure 4.6, Appendix G more closely predicts all of the 30 in. section's true buckling loads. This is consistent with the LRFD specification which would use Appendix G to analyze this section because its slender web has a web ratio greater than the elastic slenderness parameter ($\lambda > \lambda_r$). However, with the exception of the 100 in. unbraced length test ($L_b/r_y = 111$), Appendix G was unconservative in its predictions. Also, by looking at Figure 4.6 and Table 4.1, the accuracy of Appendix G seems to be diminishing as the unbraced length gets shorter.

4.2.2 Tests 11-16, 24 in. Web

The test results for the 24 in. deep section are shown in Figure 4.10. There was very little difference in the replicate test results. All of the specimens failed in a lateral torsional buckling mode except for the fully braced test ($L_b/r_y = 39$)

which failed by web local buckling. Figure 4.11 shows the lateral buckle for Test 14 that had an unbraced length of 75 in. which was typical for the 24 in. deep specimens.

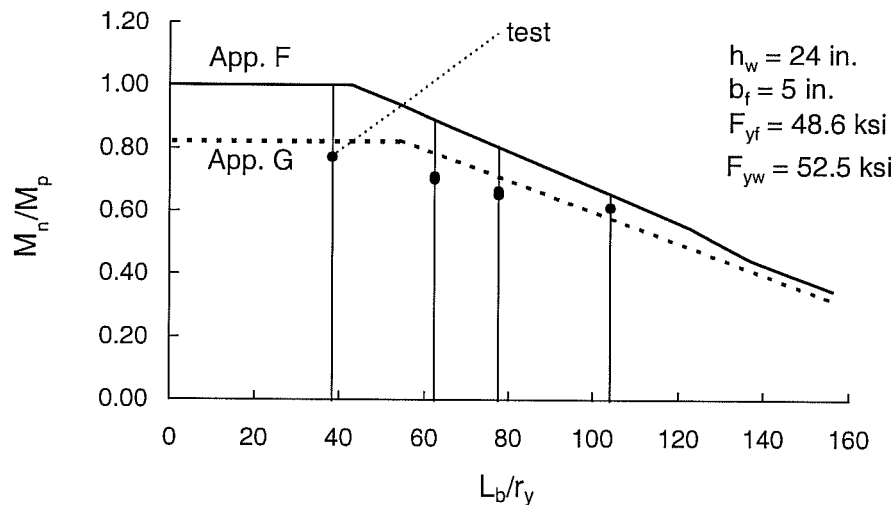


Figure 4.10: Test Results for 24 in. Deep Girder

The behavior of the 24 in. sections was similar to the 30 in. sections, but the web distortion was not as pronounced. There was visible twisting of the tension flange as it would try to restrain the lateral movement of the compression flange. However, the 24 in. section had a less slender web than the 30 in. so there was less web distortion. Web crippling at the end plate connections was not a factor for these 24 in. sections, since the compression flange on the side span beams aligned with those on the test specimen.

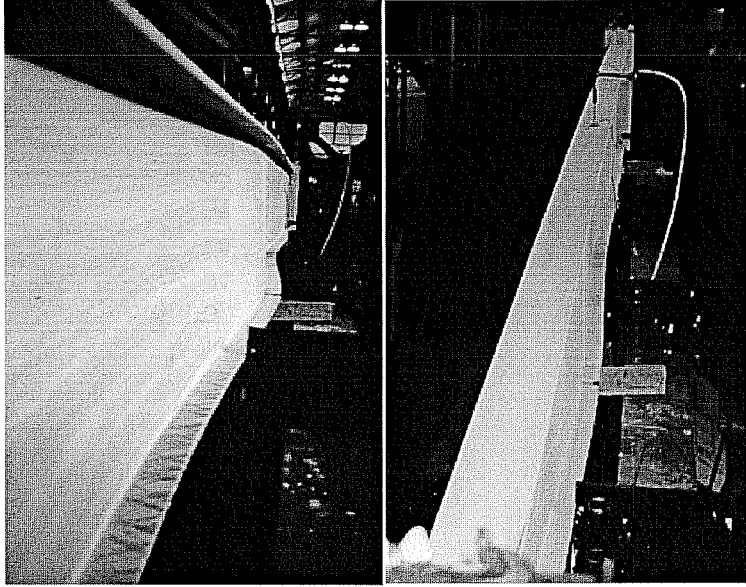


Figure 4.11: Lateral Torsional Buckle of 24 in. Deep Specimen

For the 24 in. deep girders, Appendix G predicts the true buckling load much better than Appendix F. This is once again consistent with the LRFD specification because the 24 in. deep section has a web slenderness that is considered to be slender ($\lambda > \lambda_r$). For this section, λ is 146.3 and λ_r is equal to 139.2. However, Appendix G is still unconservative in all predictions except the 100 in. unbraced length test ($L_b/r_y = 104$). Like the 30 in. section, the Appendix G prediction tends to be less accurate as the unbraced length gets shorter for all of the tests in the inelastic range.

4.2.3 Tests 5-10, 18 in. Web

Unlike the 24 in. and 30 in. sections, the 18 in. section has a web that is considered non-compact as opposed to slender. Thus, its web slenderness ratio is less than the elastic slenderness parameter ($\lambda > \lambda_r$), and Appendix F should be applicable for these sections. For this section, λ is 110 and λ_r is equal to 139.2. The test results are shown in Figure 4.12, and like the 24 in. girder tests there was very little scatter between the replicate tests. The AISC-LRFD design strength provisions are also shown. The solid line and dotted line refer to the lateral buckling limit state for Appendix F and G respectively and the dashed line shows the web buckling limit state provision of Appendix F. Since Appendix F is applicable for this section, local web buckling is considered a separate failure mode. In Appendix G, web local buckling is addressed in the lateral torsional buckling equations when the plate girder reduction factor is found (R_{pg}).

All of the 18 in. tests failed by lateral torsional buckling with the exception of the fully braced test ($L_b/r_y = 37$) which failed by web local buckling. This also occurred in the 24 in. and 30 in. test beam series.

Figure 4.12 shows that Appendix G appears to better predict the maximum load. Only the two 100 in. unbraced length tests ($L_b/r_y = 97$) reached the prediction given by Appendix F, all of the other tests either barely reached or fell short of the Appendix G predictions. This is surprising considering that Appendix F is the appropriate design method which would have been used for

these sections. Figure 4.12 shows that the AISC Appendix F prediction becomes less accurate as the unbraced length decreases. This is the same trend that was shown in Figure 4.6 and Figure 4.10 for the 30 in. and 24 in. specimens respectively.

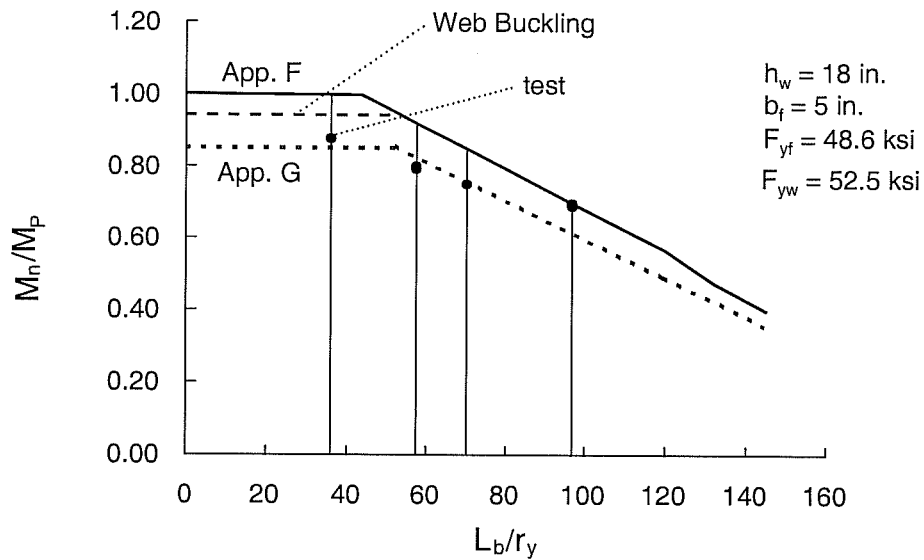


Figure 4.12: Test Results for 18 in. Deep Girder

Like the 24 in. and 30 in. test girders, the 18 in. specimens also showed signs of oil canning and tension flange twisting during the test. However, unlike the 24 in. and 30 in. beams, the web on the 18 in. did not have any visible undulations until after ultimate load was reached and the tension flange twisting was much less pronounced.

4.2.4 Tests 1-4, 15 in. and 12 in. Web

Two tests were conducted on each of the 15 in. and 12 in. deep plate girders; one at $L_b = 37.5$ in. and one with $L_b=60$ in. The results of these four tests are plotted in Figure 4.13 and Figure 4.14 respectively. For both the 15 in. and 12 in. deep web, the 60 in. unbraced length failed due to lateral-torsional buckling.

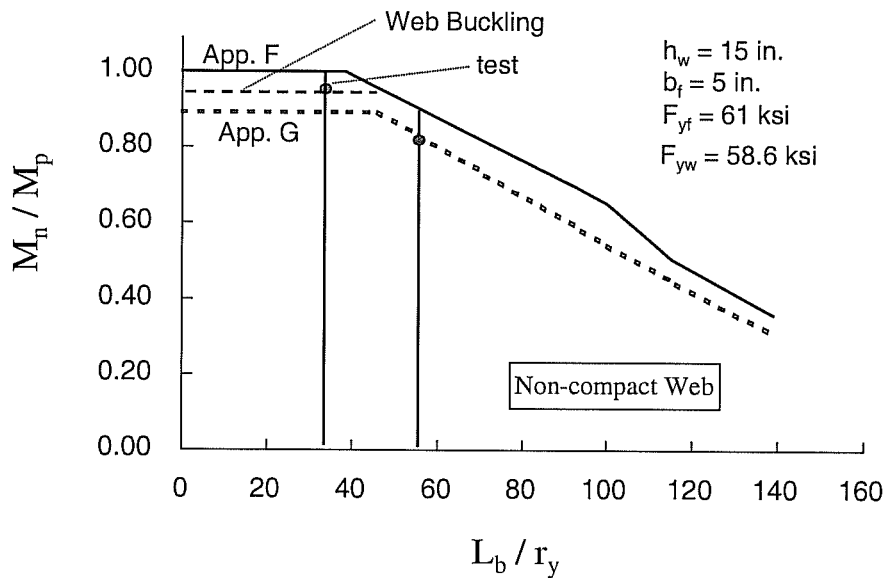


Figure 4.13: Test Results for 15 in. Deep Girder

The 15 in. deep girder which falls in the Appendix F category, did not have enough capacity to reach the Appendix G prediction. Table 4.1 shows that this beam (Test # 4) only reached 85% of the predicted Appendix F buckling load. This may seem surprising because the web is well into the non-compact range and should have buckled closer to the limit prescribed by Appendix F.

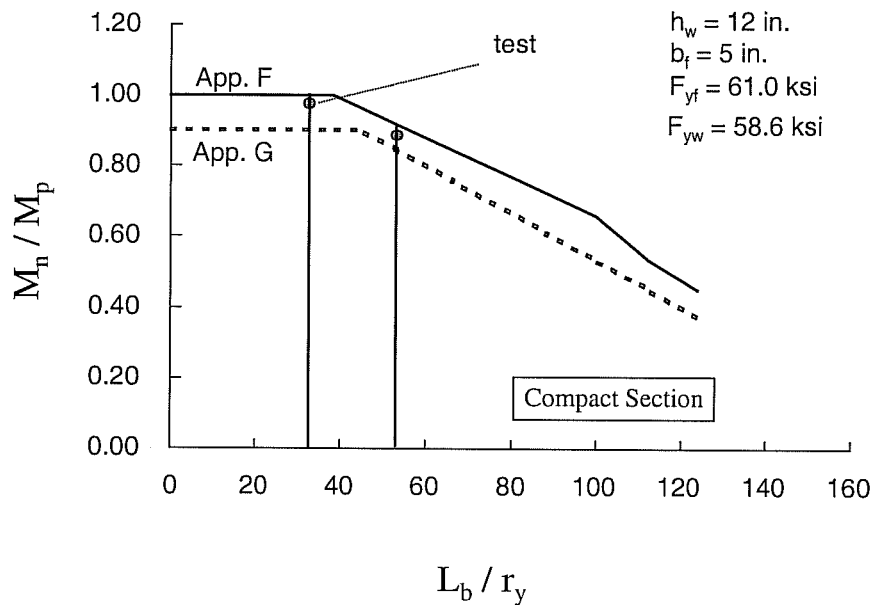


Figure 4.14: Test Results for 12 in. Deep Girder

The 12 in. girder performed slightly better but still fell short of the Appendix F buckling load for its 60 in. unbraced length test. Unlike the 15 in. girder, this section did manage to just surpass the Appendix G prediction. Since the 12 in. web is considered compact ($\lambda < \lambda_p$), the local web buckling limit state was not applicable according to LRFD. Thus, this failure mode is not shown on Figure 4.14.

For both of these sections, oil canning was present but not as easily seen because of the relatively stockier webs. In general, the webs seemed to resist distortion much better than the more slender sections, but the Appendix F flexural strengths were still unattainable.

4.3 NON-COMPACT FLANGE TESTS, TESTS 23 - 29

This series of tests were conducted on girders with non-compact flanges. When a flange is non-compact, it is susceptible to local flange buckling, which is how all of these beams failed. These tests were performed to confirm that a flange local buckle would occur and the test load was compared to the load predicted by the AISC-LRFD flange local buckling provisions. A typical flange local buckle is shown in Figure 4.15. All numerical results for all the non-compact tests are shown in Table 4.2.

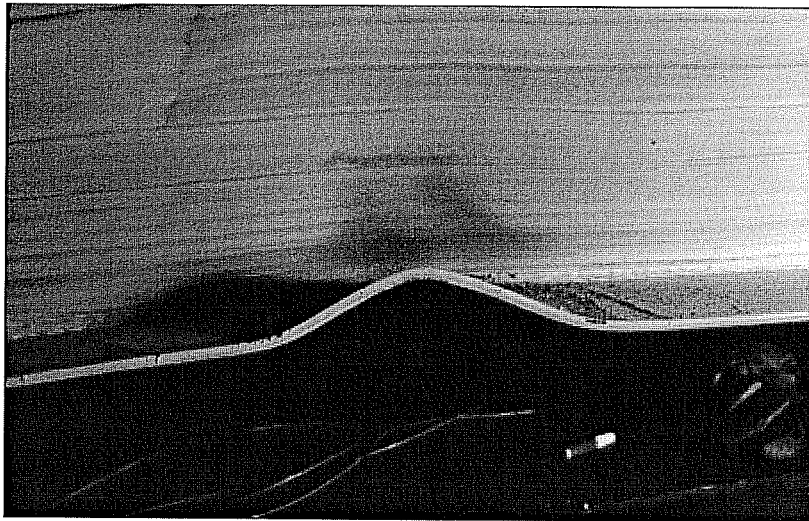


Figure 4.15: Typical Flange Local Buckle

When these flanges locally buckled, the failure was very sudden and dramatic. As the local buckle formed, the flange tried to redistribute this stress to the slender web which forced both the web and flange to immediately buckle.

Figure 4.16 shows the results of tests compared with the provisions for flange local buckling AISC-LRFD specification. The bar graph is arranged by

Table 4.2: Results of Non-Compact Tests

Test Number	h	h/t _w	b/t _f	L _b	P _{WLB(F)} (kips)	P _{FLB(F)} (kips)	P _{LTB(F)} (kips)	P _{FLB(F)} (kips)	P _{FLB(G)} (kips)	P _{LTB(G)} (kips)	P _{TEST} (kips)	P _{TEST} /P _{AISC}	M _{test} kip*in	M _{test} /M _p	Failure Mode
23	18	109.8	12	90	23.4	22.5	22.3	20.5	20.4	20.5	0.92	1722	0.75	FLB	
24	18	109.8	12	105	23.4	22.5	20.5	20.5	18.4	20.5	1.00	1722	0.75	FLB	
25	18	109.8	12	100	23.4	22.5	21.1	20.5	19.0	20.4	0.97	1714	0.75	FLB	
26	24	146.3	12	100	****	31.5	29.7	28.2	26.7	31.3	1.17	2629	0.78	FLB	
27	24	146.3	12	100	****	31.5	29.7	28.2	26.7	28.2	1.06	2369	0.71	FLB	
28	30	182.9	12	100	****	40.8	39.0	34.9	33.0	35.1	1.06	2948	0.65	FLB	
29	30	182.9	12	100	****	40.8	39.0	34.9	33.0	36.3	1.10	3049	0.67	FLB	

- * Measured F_{yf} = 58.55 ksi, F_{yw} = 51.7 ksi
- * Values For Both Appendix F & G Assume k = 1
- * FLB = Flange Local Buckling
- * WLB = Web Local Buckling
- * LTB = Lateral Torsional Buckling
- * Number In Bold Indicates Failure Mode = P_{AISC}
- **** = Does not apply

beam depth: 18 in., 24 in. and 30 in. All tests were performed using an unbraced length of 100 in. with the exception of the Tests 23 and 24. This beam had two unbraced lengths at each end that measured 105 in. and a third unbraced length at the midspan which measured 90 in. For all cases when flange local buckling was critical, the test load, P_{test} , exceeded the LRFD prediction for flange local buckling, P_{AISC} . From the seven flange local buckling tests performed, the LRFD specification appeared conservative.

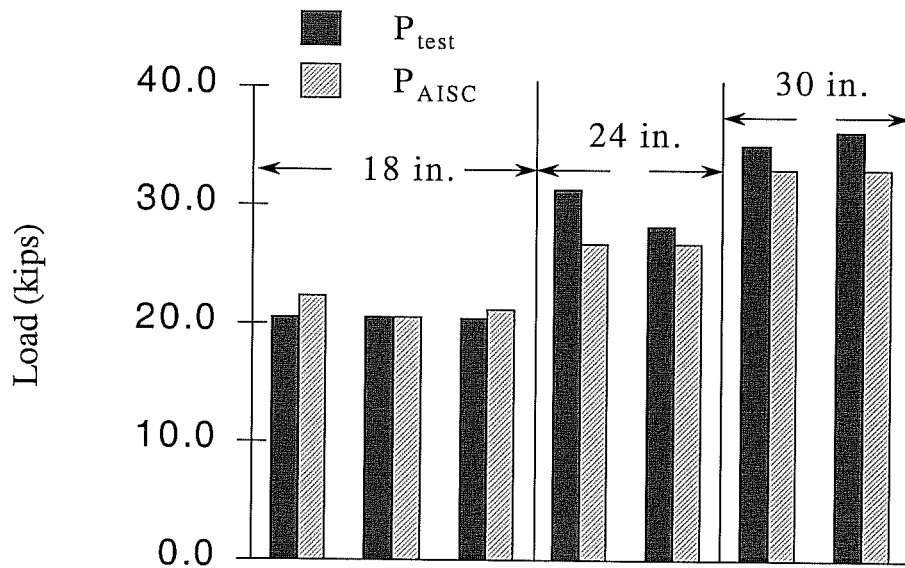


Figure 4.16: Flange Local Buckling Results

4.4 FULLY BRACED COMPACT FLANGE TESTS

Every compact flange section was tested at a full braced configuration to see if the plastic moment, yield moment or the web buckling moment could be achieved. These were test numbers 1,3,5,11 and 17. The moment that was expected depended on the web slenderness of the section in question and could be determined by simply looking at the lateral torsional buckling graphs shown in this chapter. If the section is fully braced and has compact flanges, a slender web should be able to reach the yield moment of the section, a non-compact web should reach the web buckling moment, and a compact web should reach the plastic moment based on the LRFD-AISC Specification.

For the fully braced configuration for all of the sections, lateral braces were placed at an unbraced length of 37.5 in. At this length, all sections were considered to be in the plastic region ($\lambda < \lambda_p$) of the lateral torsional buckling graph. Thus, the plastic, web buckling or yield moment should be achieved. However, not one of the beams that was tested in this configuration had the strength to reach the design moment predicted by AISC-LRFD. This is shown in Figures 4.5, 4.10, 4.12, 4.13, 4.14.

All of the sections that were fully braced failed due to a premature buckle in the web. When this web buckled, it drove the flange to buckle with it. This flange buckle was not a normal flange local buckle (FLB) that takes place when you have a non-compact flange (seen in Figure 4.15). The FLB on a section with non-compact flanges happens very suddenly, develops instantly, is very sharp and

abrupt, and is only about 4 in. - 6 in. in length, which was equivalent to the flange width. The FLB that was caused by the initial web local buckle had a long buckled length; as much as 15 in. in length for the 30 in. deep section and got shorter as the web became less slender. In addition, the buckle happened gradually and did not result in a sudden and dramatic failure. A typical web local buckle that was observed in the 30 in. section is shown as Figure 4.17.

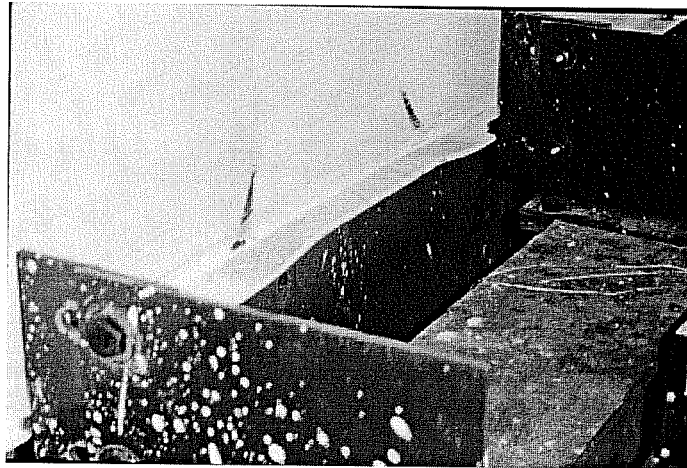


Figure 4.17: Typical Web Local Buckle

CHAPTER 5

FINITE ELEMENT ANALYSIS

A three dimensional inelastic finite element analysis (FEM) was performed on all 24 in. deep girders. The analysis was conducted using the ABAQUS 5.6-7 software package and a Cray T90 Parallel Vector Supercomputer. This analysis was performed to verify the validity of the FEM model so that future work could utilize theoretical analysis rather than expensive experiments. If the analysis is reasonably accurate, then various parametric studies can be used to develop reliable design rules.

5.1 FINITE ELEMENT MODEL

The full geometry of the setup; which included both side spans, both end plates and the test beam; was modeled and is shown in Figure 5.1. The axes are defined as:

- 1 the longitudinal direction
- 2 the lateral direction
- 3 the transverse direction

All unbraced lengths , which included the 100 in., 75 in. 60 in. 37.5 in., were examined and compared to the actual test results using the same initial lateral out-of-straightness for each FEM analysis. This initial deflected shape is shown as

Figure 5.2 where $\Delta_0 = 0.1$ in. The model was loaded at the side span ends and subjected to uniform moment. The model used C3D8 continuum elements so that both stress and displacement could be observed.

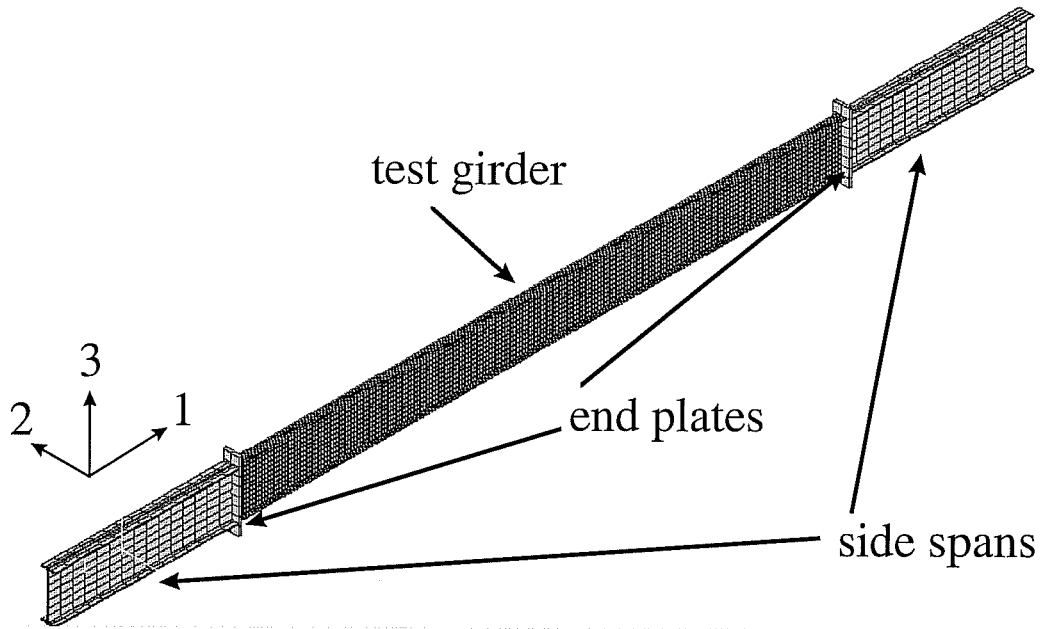


Figure 5.1: FEM Model of Test Setup

The end plate connections were modeled by defining four surfaces: the end of the side span adjacent to the end plate, the end of the test girder adjacent to the end plate, and one on each side of the end plate. After these surfaces were defined, both the test girder and side spans could be connected to the end plates by using the tied parameter in the contact pair command with the beams considered to be the slave surfaces and the end plates as the master surface. By modeling the connection this way, it is assumed to be infinitely stiff.

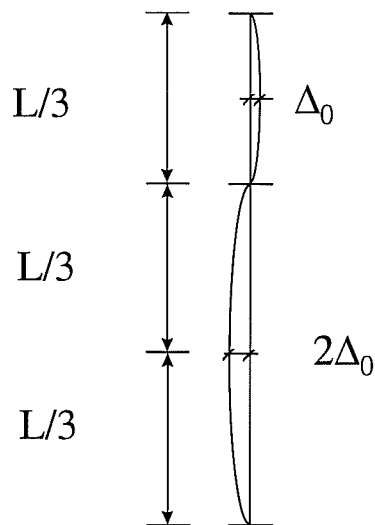


Figure 5.2: Typical Initial Displacement For All FEM Models

The test girder was modeled as a hybrid section with the yield stress in the flange equal to 48.6 ksi and the yield stress in the web equal to 52.0 ksi. The end plates and side span beams were assumed to be grade 50 steel. An isotropic hardening model was assumed for both the web and flange, but both side spans and end plates were assumed to remain elastic due to their relatively thick cross sectional areas. Figure 5.3 shows the typical stress strain curve used for the flange material.

The model was simply supported at the side spans in accordance with the conditions shown in Figure 3.2. To avoid any unwanted local buckling in the flange of the side spans, the supports were defined across the flange's entire width. The pinned support was fixed in the x, y and z directions while the roller support was only fixed in the y and z directions. The end plates were restrained

torsionally by laterally fixing the end plate at the top and bottom to prevent them from twisting. The compression flange of the test girder was laterally braced by fixing the proper nodes in the 2 direction (lateral direction) as shown in Figure 5.1.

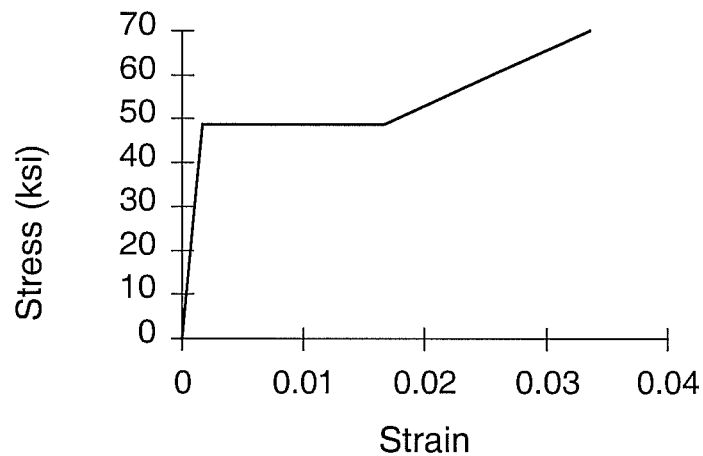


Figure 5.3: Stress-Strain Curve For The Isotropic Hardening Model

In order to perform the inelastic analysis, a RIKS Buckling method was defined. This method uses a geometrically nonlinear load-displacement inelastic solution procedure and an initially imperfect geometry to converge on an inelastic solution. This solution procedure allows convergence for a member with large displacements which would prove unstable for elastic procedures. In order to try and minimize computational time, only twenty increments were specified in the step.

The RIKS method uses a proportion of a total specified load to assess whether or not the system is stable or unstable. If stable, it adds more load in a

prespecified incrementation until the system is unstable. Once this occurs, the percentage of the applied load at this stage is the point at which the system fails or the buckling load.

5.2 FINITE ELEMENT RESULTS

The goal of the finite element analysis was two fold. First, ABAQUS was used to gain an understanding of how close the predicted buckling value would come to the test load. Once these loads were compared, the actual behavior of the model was compared to the test. This “behavior” included general tendencies of the beams during the test, buckling modes and failure modes. By comparing the theoretical buckling loads to the test loads, the validity of the analysis will be confirmed and considered acceptable.

This section will discuss the results of all four finite element models that were analyzed. These four models used the same 24 in. deep girder and had unbraced lengths of 100 in., 75 in., 60 in. and 37.5 in. Figure 5.4 shows how these results compared to both the AISC-LRFD predictions and the test buckling load. The buckling load that ABAQUS provided is plotted as a diamond for each unbraced length. Figure 5.4 shows that the ABAQUS predictions, shown as diamonds, are very close to the test load for all unbraced lengths. This accuracy is excellent when lateral torsional buckling is the failure mode, but some accuracy is lost when the girder is fully braced and lateral torsional buckling is no longer

critical. The shortest unbraced length, which has the largest difference between the two loads of 7.0%, still has very reasonable accuracy.

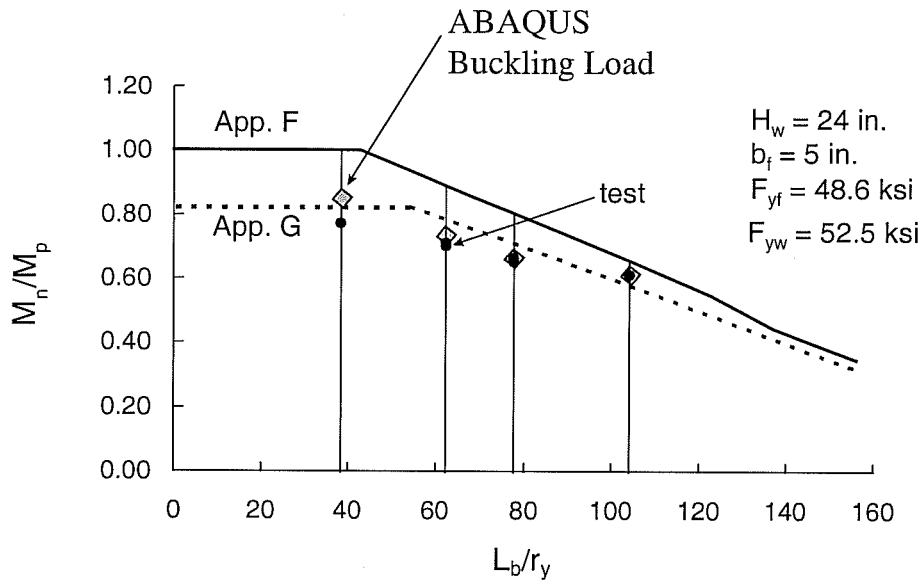


Figure 5.4: Test and Predicted ABAQUS Load compared to AISC-LRFD Specification

For these 24 in. deep sections ABAQUS predicted two types of failure modes for the unbraced lengths modeled. ABAQUS was successful in predicting the failure modes of the 100 in., 75 in. and 60 in. unbraced length girders which all failed due to a lateral torsional buckle. However, the program had trouble successfully modeling the fully braced girder. This girder, which was modeled with an unbraced length of 37.5 in., failed in the laboratory by local web buckling. The results will be organized and discussed by failure mode.

5.2.1 Lateral Torsional Buckling Tests ($L_b = 100$ in., 75 in. and 60 in.)

The three longest unbraced lengths, the 100 in., 75 in. and 60 in., all failed in the lab by lateral torsional buckling. For all three lengths, ABAQUS was able to successfully detect this failure mode as critical and also provide the correct mode of buckling. The deflected shape and stress contour for the 100 in. unbraced length FEM is shown in Figure 5.5. This shape is indicative of a lateral torsional buckle due to the large out-of-plane displacements. The figure shows the standard stress contour of a beam under uniform moment with the highest stressed regions located at the extreme fibers and the lowest at the neutral axis of the member. The highest concentration of stress is located on the compression flange at the center unbraced span. This high stress region is caused by an in-plane bending stress component and a lateral bending stress component. The maximum stress took place on the compressive portion of the web at the flange and web interface. After some strain hardening, the maximum stress was 53.9 ksi.

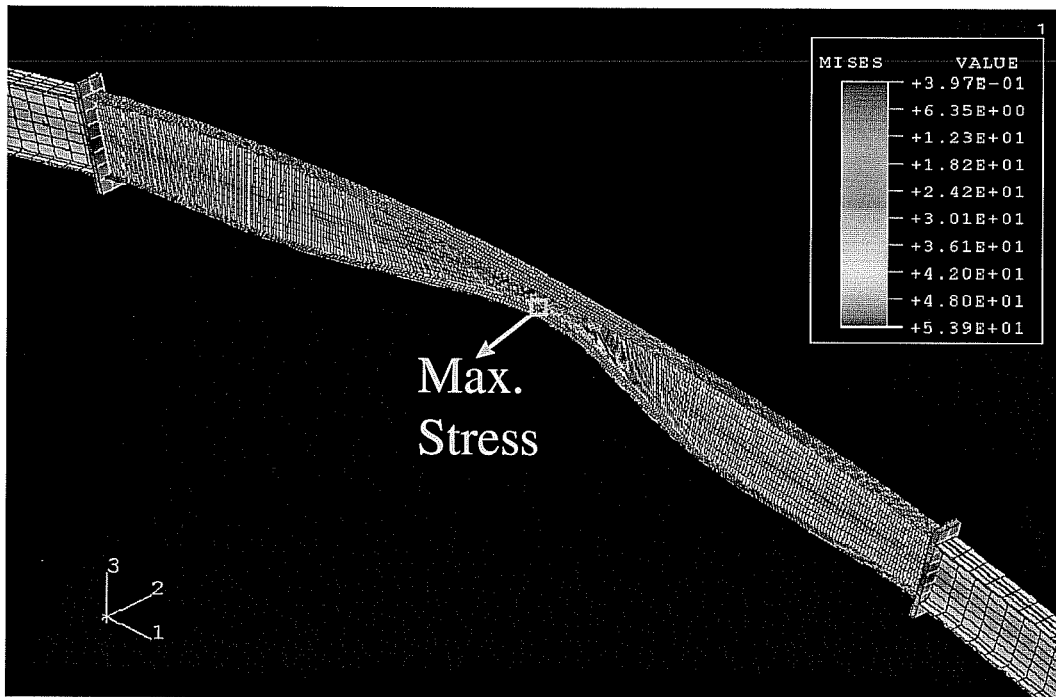


Figure 5.5: Stress Contour For The 100 in. Unbraced Length Model

Since the web material was modeled with a higher yield stress than the flange material, in order for the maximum stress to be located on the web, the flange material must have yielded. The stress contour in Figure 5.5 shows that the flange material is at a stress between 48.0 ksi and 53.9 ksi . The yield stress of the flange material is 48.6 ksi. Figure 5.5 shows that this maximum stress is located at the midspan of the centermost unbraced length. In this region, there is little lateral stiffness in the beam due to the yielding of the flanges and a great deal of distortion in the web. Due to the high degree of web distortion and the lack of

lateral stiffness in the flanges, the web buckles from the increasing demand placed on it, which results in the high region of stress shown in Figure 5.5.

Figure 5.5 shows that the middle unbraced length is the critical span for the model. Like the actual tests performed in the laboratory, the FEM shows that only the compression flange moves laterally. The contour also shows the tension flange twisting, described in Chapter 4, which occurred in all of the lateral torsional buckling tests performed in the lab. This girder, as predicted by the FEM, failed due to a lateral torsional buckle in the centermost span. Thus, ABAQUS proved to be a very useful and effective tool in predicting the behavior of this particular girder, and according to Figure 5.4, the results that were given proved to be extremely accurate.

Figure 5.6 shows the deflected shape and stress contour for the 75 in. unbraced length. The stress contour in Figure 5.6 is indicative of a typical lateral torsional buckle which is the same failure mode that occurred in the lab. Like the 100 in. unbraced length FEM, the 75 in. FEM yields very accurate results when compared to the test. This is shown in Figure 5.4 which shows a difference of less than 1.9% between the ABAQUS prediction and the average of the two test loads. However, the 75 in. FEM shows much more web distortion than the 100 in. For this FEM, the highest stress concentrations are at the web and flange interface in the middle of the unbraced length where the highest value of lateral movement is seen. At this location, the stresses reached a maximum value of 54.9 ksi after strain hardening.

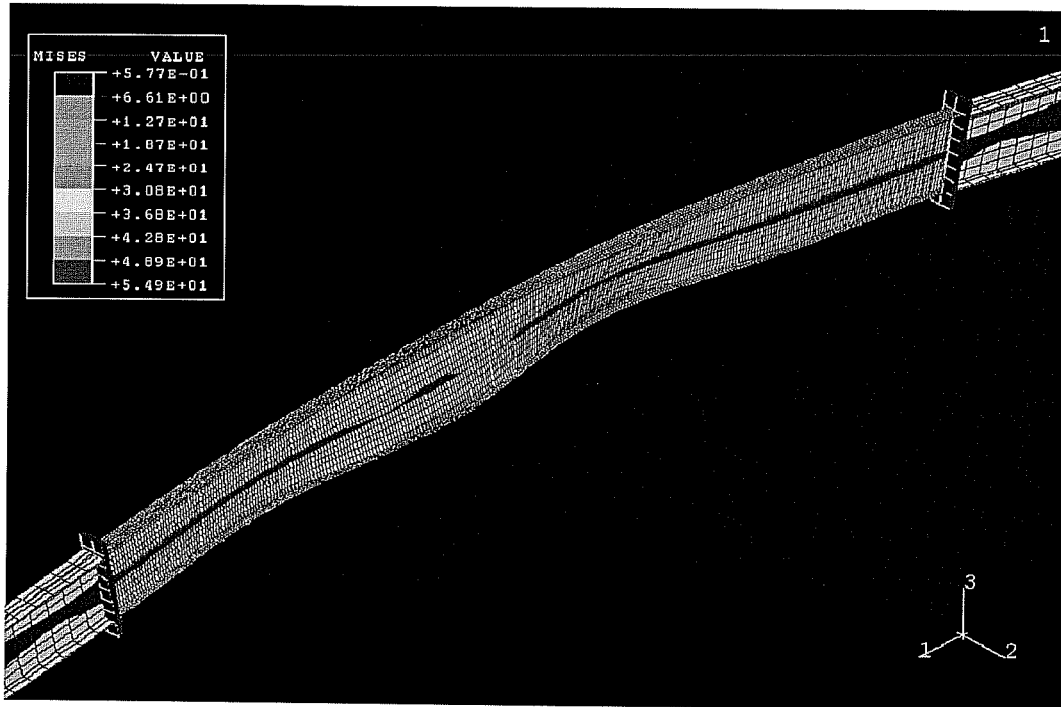


Figure 5.6: Stress Contour For The 75 in. Unbraced Length Model

Since these girders were modeled as hybrids with the web yield stress greater than the flange yield stress, the maximum stress will take place on the web once the flanges become fully yielded. The stress contour in figure 5.6 shows that both flanges in this model have fully yielded, and some sections of the web near the web and flange interface have also yielded. Since the web's yield stress is higher, the maximum stress, shown as red, is on the web and not the flange.

The 60 in. unbraced length FEM is shown in Figure 5.7. Like the 75 in. and 100 in. models, the 60 in. model's maximum stress is also located on the web at the web and flange interface. This model gave predictions that differed from

the actual test loads by 1.6%. The stress contour and deflected shape once again indicate the correct failure mode of lateral torsional buckling with the maximum stress, having a value of 56.3 ksi, taking place in the web at the web and flange interface. Also, the maximum stress, like that of the 100 in. and 75 in. models, was at the midspan of the centermost unbraced length.

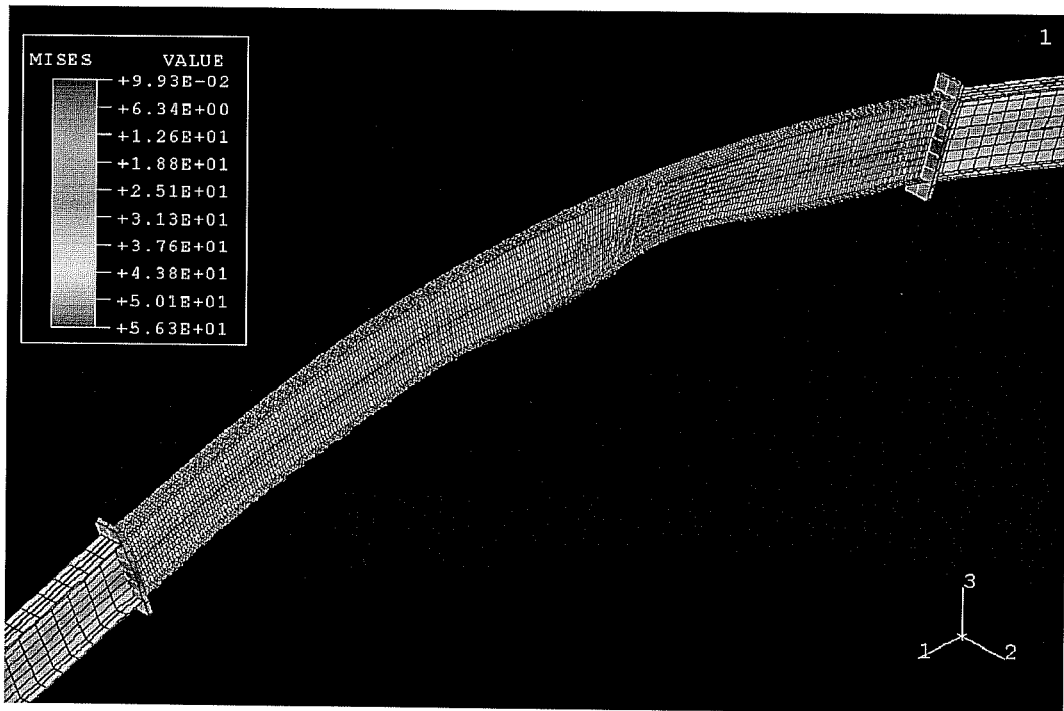


Figure 5.7: Stress Contour For The 60 in. Unbraced Length Model

5.2.2 Fully Braced Test ($L_b = 37.5$ in.)

The 37.5 in. unbraced length FEM was the only model that did not result in a lateral torsional buckle. ABAQUS predicted the true buckling load within a

7.0% difference, but the mode of failure is not clear. The stress contour that ABAQUS provided is shown in Figure 5.8. By looking at the deflected shape and stress contour, there is no apparent reason why the program could not continue to apply more load. There is no obvious signs of instability and the section has not fully yielded.

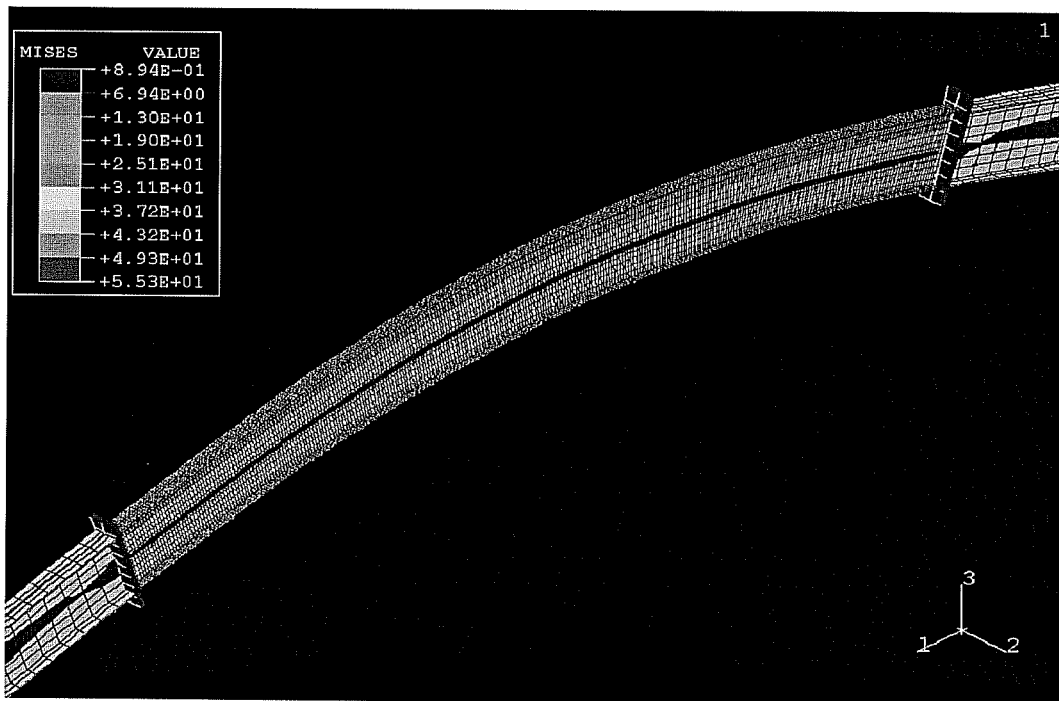


Figure 5.8: Stress Contour For The Fully Braced Model

Figure 5.9 shows the load centerline deflection curve for the FEM incrementation. The true test load is shown on the figure as 28.4 kips. This curve indicates that the section has lost all stiffness. The stress contour, indicates that

the section has not been fully yielded. Since the RIKS inelastic buckling analysis uses a load-displacement solution procedure, the program terminated when ABAQUS detected a complete loss of stiffness. Thus, there must exist some type of localized instability which has caused this loss of stiffness. However, the displaced shape on the stress contour does not show any lateral movement which is indicative of such a failure.

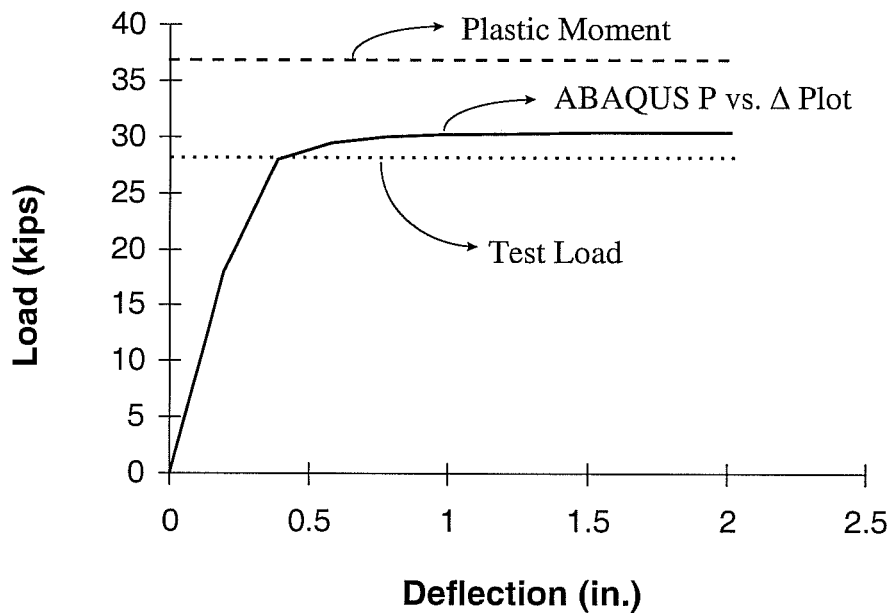


Figure 5.9: Load-Deflection Curve For Fully Braced ABAQUS Model

The test performed in the lab at this unbraced length failed due to a local buckle in the web near the web and flange interface which drove the flange to locally buckle as shown in Figure 4.17. However, there is no localized failure present in the analysis which ABAQUS performed. Although the program was

able to predict the true buckling load with considerable accuracy, it seemed illogical for the program to stop the incrementation since no signs of instability were present. There was no evident cause for the program to terminate, whether it be a localized failure or full yielding of the section.

5.3 CONCLUSIONS FROM FEM RESULTS

The results reported above show that finite element can be an extremely powerful tool to help predict and understand the behavior of a slender web plate girder. However, it is dangerous to rely on these results without logically justifying the credibility of the analysis. ABAQUS did a good job in modeling the behavior of these beams when lateral torsional buckling was the critical failure mode. It accurately predicted the true buckling loads, and the buckling modes for every test where lateral torsional buckling was critical. The stress contours showed that lateral instability was introduced by yielding of the compression flange at the midspan of the centermost unbraced length. This instability placed an increased demand on the slender web which was unable to cope with these high stresses. As a result, a lateral torsional buckle occurred.

The fully braced results were not as conclusive as the lateral torsional buckling failures. Although the ABAQUS prediction was only 7.0% from the test load for the fully braced condition, it would be ill-advised to accept the prediction that ABAQUS provided because no cause could be attributed to the premature termination of the program.

CHAPTER 6

DESIGN RECOMMENDATIONS

6.1 DESIGN PROVISIONS

In order to evaluate the suitability of the current design provisions given in Appendices F and G of the AISC-LRFD Specification, all the test data from sections with compact flanges will be compared to Appendix F provisions and Appendix G provisions separately. Figure 6.1 presents the design strengths from Appendix F of the AISC-LRFD specification for each of the sections tested with compact flanges. The flexural strength and unbraced length are nondimensionalized by M_p and r_y respectively. When nondimensionalized in this fashion, the design strengths given by Appendix F are similar for each depth girder as long as the yield strengths are the same. The buckling curves for the 30 in., 24 in. and 18 in. deep girders, which all came from the same material, have little variance. The same is true for the 15 in. and 12 in. girders, which also came from the same material.

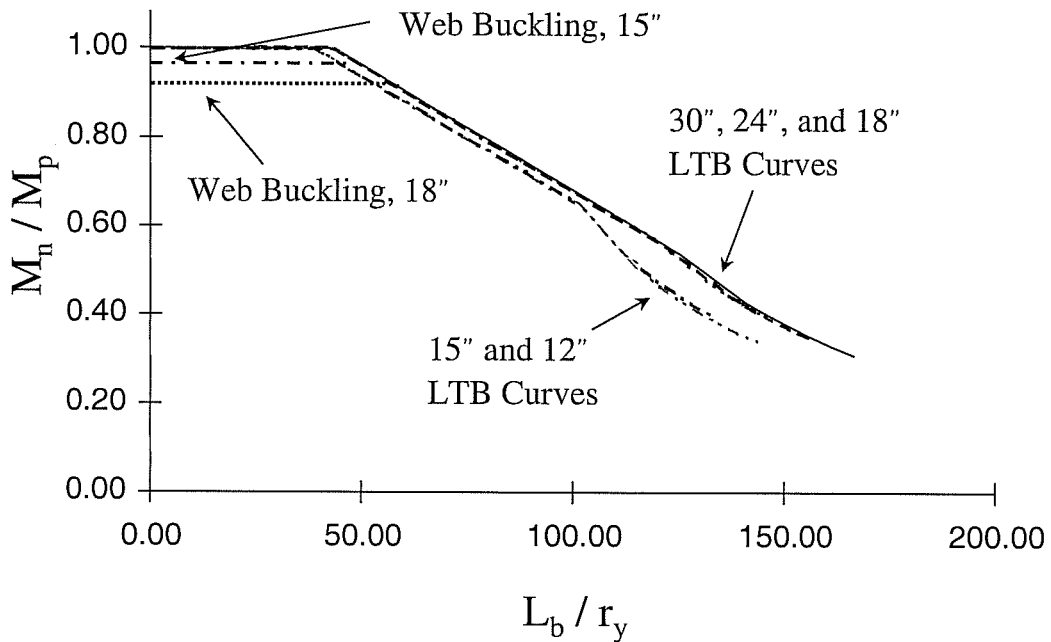


Figure 6.1: Nondimensionalized Appendix F Flexural Strength Provisions

Figure 6.2 shows the design strength curves for the 30 in., 24 in. and 18 in. girders plotted with their respective test values. The graph shows that Appendix F overestimates the strength for all three girders. This may not seem irregular since the 30 in. and 24 in. girders, which have slender webs, both fall into Appendix G. However, the 18 in. girder has a web slenderness that places it well into Appendix F and the strength is still overestimated by the AISC-LRFD specification.

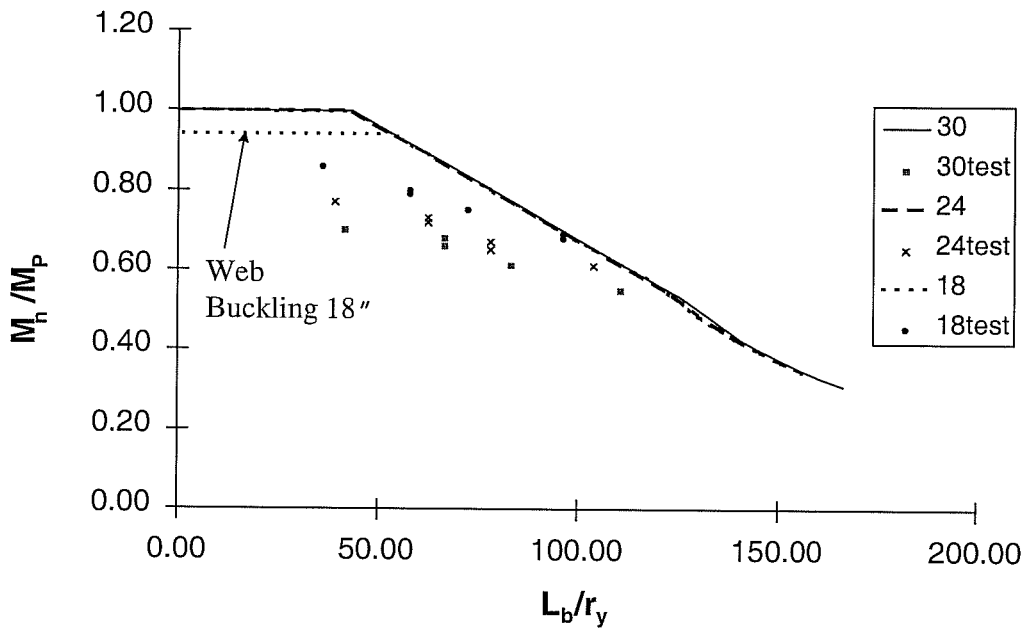


Figure 6.2: Appendix F Strength Curves With Test Loads For 18 in., 24 in. and 30 in. Sections

The 15 in. and 12 in. girders are evaluated in Figure 6.3. Like the 18 in. girder, both girders in this plot would be currently governed by the Appendix F strength provisions. The plot shows that the Appendix F predictions still are not met for these relatively stockier webs. This is surprising for the 12 in. web, which has a web slenderness that meets the compactness requirements for Appendix F. For all of the beams with compact flanges that were tested, Appendix F appears unconservative in its predictions despite the fact that the strength of three out of the five girders would currently be based on this Appendix.

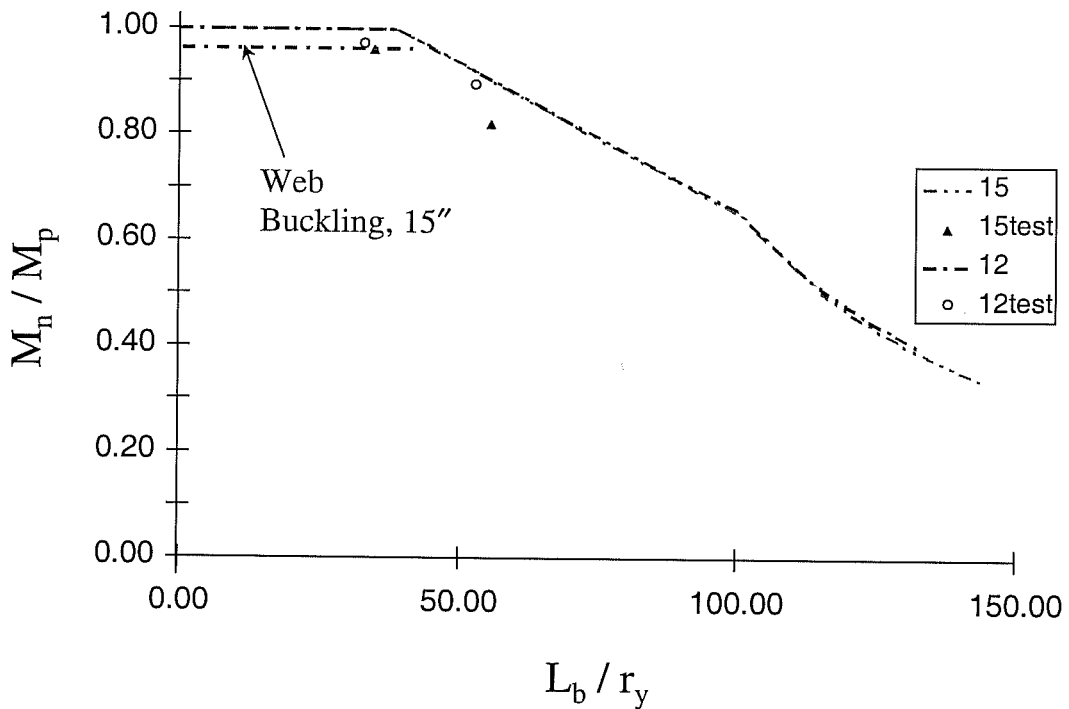


Figure 6.3: Appendix F Strength Curves With Test Loads For 15 in and 12 in. Sections

The Appendix G buckling graph along with the test results are shown in Figure 6.4. In order to be consistent with the Appendix G provisions, the flexural strength is nondimensionalized by the yield moment rather than the plastic moment and the unbraced length with r_T instead of r_y . The design provisions for the 30 in., 24 in., and 18 in. girders are very similar because the same material was used in these girders.

Figure 6.5 shows how the 30 in., 24 in., and 18 in. tests compare to the Appendix G strength provisions. The 30 in. girder has a slightly higher strength due to a varying R_{PG} reduction factor. When compared to Appendix F, Appendix G appears to predict the buckling loads of the member with much

greater accuracy even for the 18 in. girder which would be controlled the Appendix F provisions.

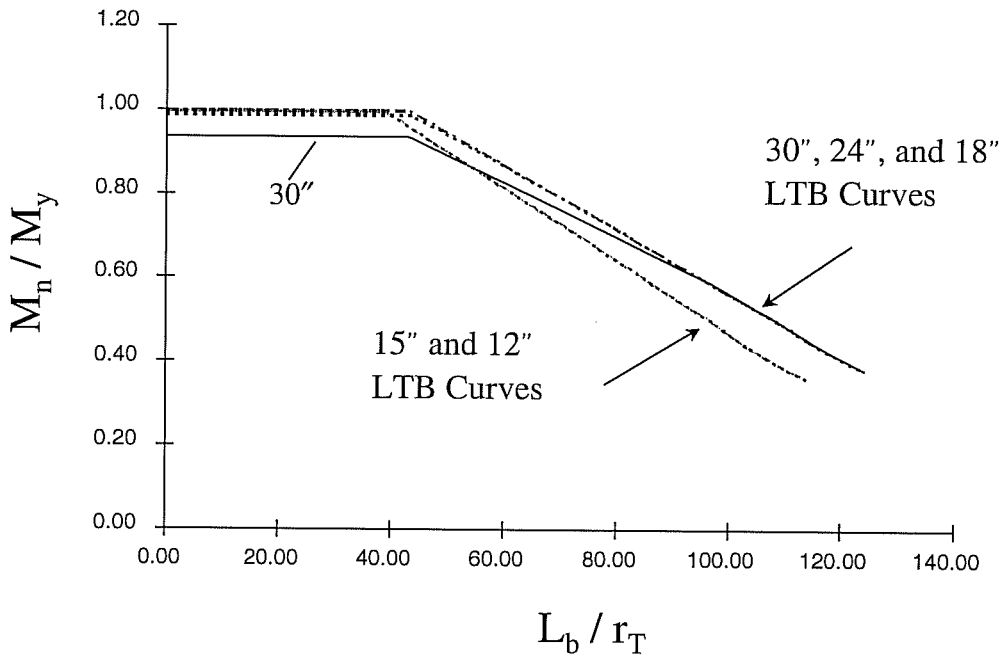


Figure 6.4: Nondimensionalized Appendix G Flexural Strength Provisions

In Figure 6.6, the buckling loads of the 15 in. and 12 in. girders are compared to the Appendix G provisions. These girders, which have relatively stockier webs, just barely reached the yield moment for the fully braced test ($L_b/r_t \approx 29$). This may seem surprising since Appendix F predicted these beams to reach their plastic moment at this unbraced length.

After comparing all of the tests to the AISC-LRFD strength provisions, it is clear that Appendix G more accurately predicts the flexural strength of all of the welded sections that were tested in this program. The cause of such an inconsistency in the AISC-LRFD specification could be attributed to the web of

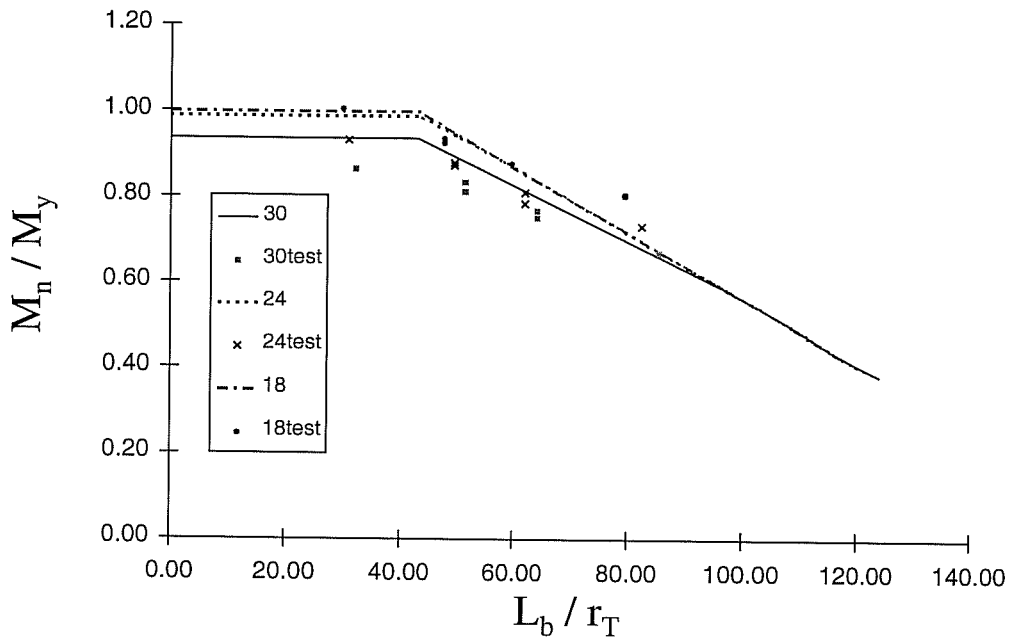


Figure 6.5: Appendix G Strength Curves for Slender Web Girders

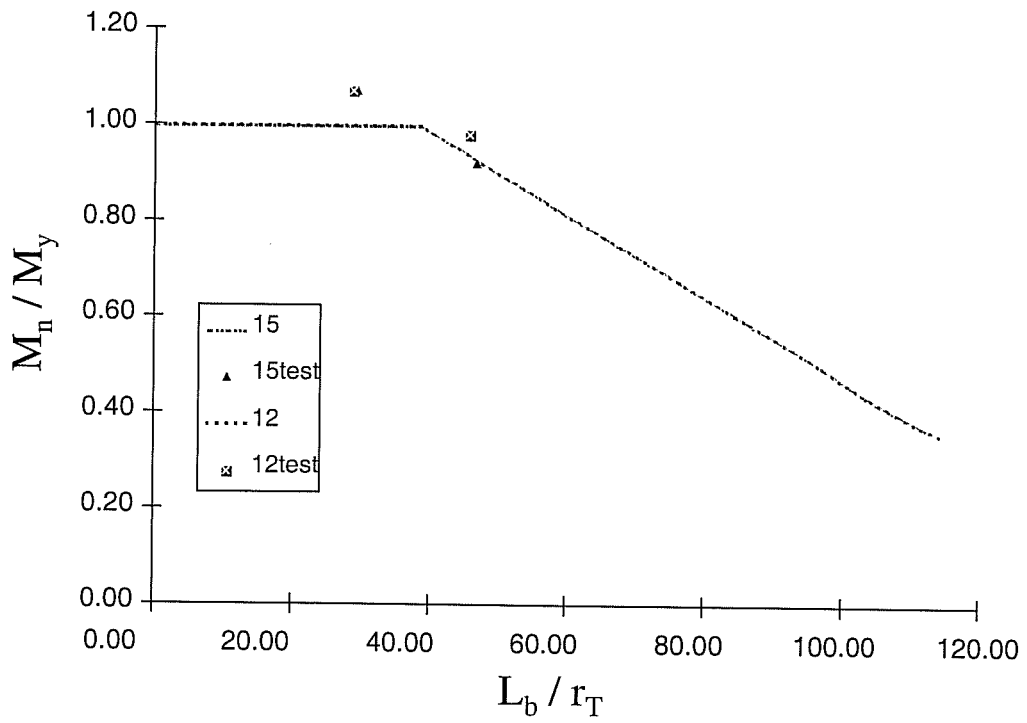


Figure 6.6: Appendix G Strength Curves for 12 in and 15 in Sections

these welded sections. The tendency of all the webs to “oil can” may cause enough of an initial instability to induce premature buckling of the member. The differential cooling caused by the welding process creates a region of high residual stresses. This region of high initial stress caused many of these webs, most notably the more slender ones, to have visible undulations down the entire length of the member before any load was placed on them. Although the oil canning did not seem to affect the in-plane stiffness of the member, after the beam reached its buckling load these initial undulations in the web were amplified.

These initial waves in the web may be a cause of the premature buckling of the members tested. The current tolerance for lateral displacement of the webs according to the Low Rise Building Systems Manual (1996) is $D/72$ where D is the height of the web between flanges. Table 6.1 shows the allowable tolerances and the actual tolerances measured from random test specimens. All members tested were within the allowable limit which may lead to the fact that these tolerances need to be more strict.

Table 6.1: Allowable And Actual Initial Web Displacements

Depth (in)	$\Delta_{\text{allowable}}$ (in)	Δ_{actual} (in)
12	0.167	0.031
15	0.208	0.063
18	0.250	0.063
24	0.333	0.250
30	0.417	0.375

Figure 6.7 shows how the test loads compared to the strengths predicted by the Fukumoto Equation. The figure shows that this equation does a reasonably

accurate job in predicting the strength of these girders. Only the fully braced configuration of the 30 in. deep girder was unconservative in its forecasted strength. The Fukumoto equation appears to be an adequate alternative for the analysis of these welded sections.

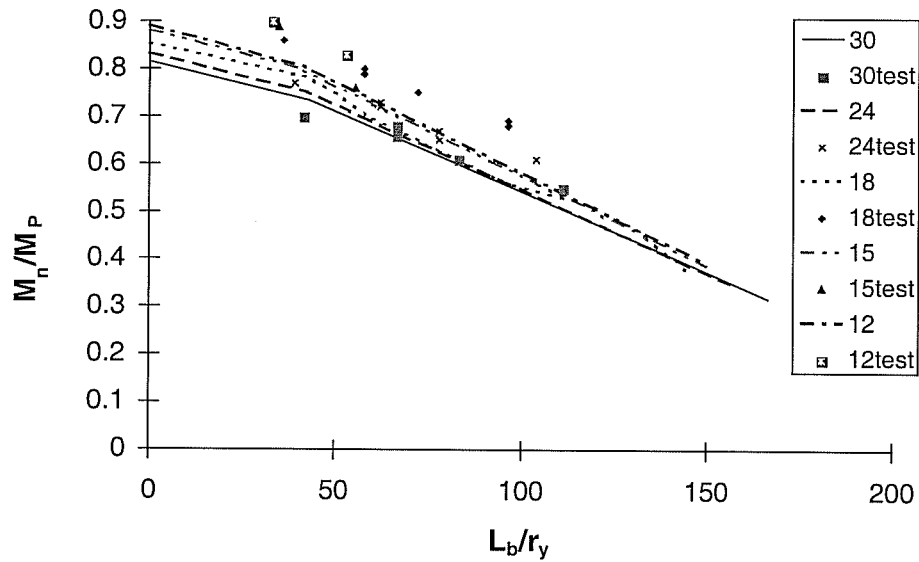


Figure 6.7: Fukumoto Strength Predictions With Test loads

6.2: RECOMMENDATIONS

Currently, Appendices F and G in the AISC-LRFD specification, should be based solely on the web slenderness, disregarding whether the member is rolled or welded. However, it has been shown that Appendix G more accurately predicts the strength of these welded sections, the depth of the member notwithstanding. In order to correct the unconservative predictions that the current specification

provides two options were investigated. The first was to use Appendix G rather than Appendix F to analyze all welded sections regardless of the web slenderness.

The second was to reduce the design strength provided by Appendix F as a function of the beam's web slenderness to eliminate any unconservativeness for welded sections. By reducing the maximum moment as a function of web slenderness, the Appendix F buckling graph would be shifted down to adjust for the adverse effects that these webs have on the strength of the section. Figure 6.8 shows the fully braced test results for all web slenderness ratios. The graph plots the percentage of the plastic moment attained as a function of the member's web slenderness. The shape of the plot is very similar to the AISC column curve. For extremely short unbraced lengths, the highest possible value a welded section could reach is 90% of its plastic moment. As the web slenderness increases, the percentage of the plastic moment that was reached decreases.

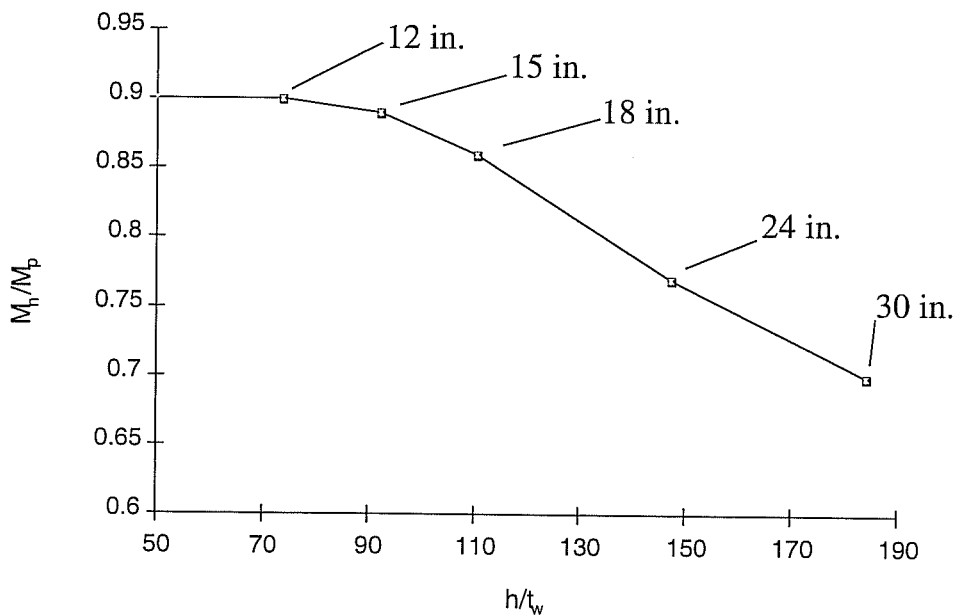


Figure 6.8: Percent of Plastic Moment Reached vs. Web Slenderness

The reduced plastic moment found in Figure 6.8 would have to be used in the inelastic lateral torsional buckling equations. From Figure 6.8, the 24 in. girder's maximum moment would be only 77% of the actual value for M_p . In the inelastic formula for lateral torsional buckling, which is a simple linear interpolation between the section's M_p and M_r values, the value for M_p would reduce to 77% of M_p . This is done in Figure 6.9. This approach provides buckling strengths which are more conservative than Appendix G. Though, the reduced strength predictions are reasonably accurate, more research needs to be conducted in this area. Thus, the logical alternative is to currently analyze all welded section using Appendix G.

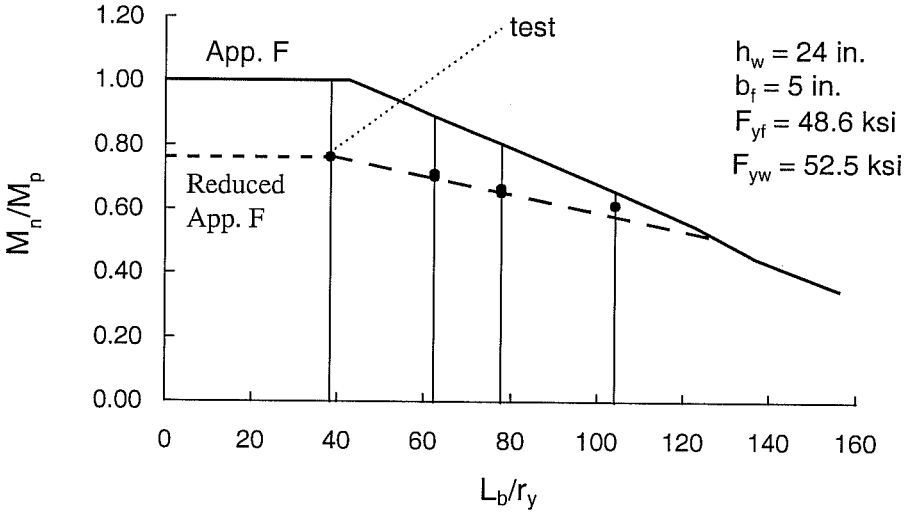


Figure 6.9: Reduced Appendix F Strength Provisions With Tests For 24 in. Section

More research needs to be conducted regarding the effect of “oil canning” on a section. The tests presented have shown that the tendency of the web to behave in this fashion may result in premature failure. If this initial out-of-straightness of the web is causing an instability, then it needs to be corrected.

CHAPTER 7

SUMMARY AND CONCLUSIONS

A test program was designed to correct the inconsistency that exists between the flexural strength provided by Appendices F and G in the AISC-LRFD Specification. A total of twenty-eight specimens were tested under uniform moment. All specimens were welded plate girders. The main variables in the program were web slenderness, unbraced length and flange slenderness. The test loads were compared to the strength provisions of both Appendices to examine their accuracy. Finite element analysis was performed on one section to check the credibility of the test results.

All of the test data provided shows that Appendix F overestimated the flexural strength for welded sections. However, Appendix G predicted the buckling loads with reasonable accuracy. These results were independent of web slenderness which is the only criteria in the current specification that decides the appropriate Appendix for a member. This premature failure may be attributed to the tendency of the web of these girders to “oil can”. These results lead to the conclusion that all welded sections should be based on the Appendix G strength provisions and Appendix F should no longer consider such members. Also,

further investigation should be conducted on the influence of “oil canning” on the flexural strength of plate girders.

APPENDIX I

IMPORTANT EQUATIONS

LRFD EQUATIONS:

$$1. \quad R_e = \frac{12 + a_r(3m - m^3)}{12 + 2a_r}$$

$$2. \quad M_n = C_b \left[M_p - (M_p - M_r) \left(\frac{\lambda - \lambda_p}{\lambda - \lambda_r} \right) \right] \leq M_p$$

$$3. \quad M_n = S_{xc} R_{pg} R_e F_{cr}$$

where:

$$R_{pg} = 1 - \frac{a_r}{1200 + 300a_r} \left(\frac{h_c}{t_w} - \frac{970}{\sqrt{F_{cr}}} \right) \leq 1$$

$$F_{cr} = C_b F_{yf} \left[1 - \frac{1}{2} \left(\frac{\lambda - \lambda_p}{\lambda_r - \lambda_p} \right) \right] \leq F_{yf}$$

Barth Equations:

$$4. \quad M_n = \partial Z_x F_y$$

where:

$$5. \quad \partial = 0.989 + \frac{3.75}{\sqrt{2D_{cp}/t_w}} + 0.0932 \frac{A_{fc}}{A_{wc}} - \frac{M_p}{M_y} \leq 1$$

Fukumoto Equations:

$$6. \quad M_n = M_y \frac{\sigma_{uf}}{\sigma_{yfc}} \quad \sigma_{uf} \leq \sigma_{uw}$$

where:

$$7. \quad \frac{\sigma_{uf}}{\sigma_{yfc}} = 1, \quad \lambda \leq 0.2$$

$$8. \quad \frac{\sigma_{uf}}{\sigma_{yfc}} = 1 - 0.412(\lambda - 0.2), \quad 0.2 < \lambda \leq \sqrt{2}$$

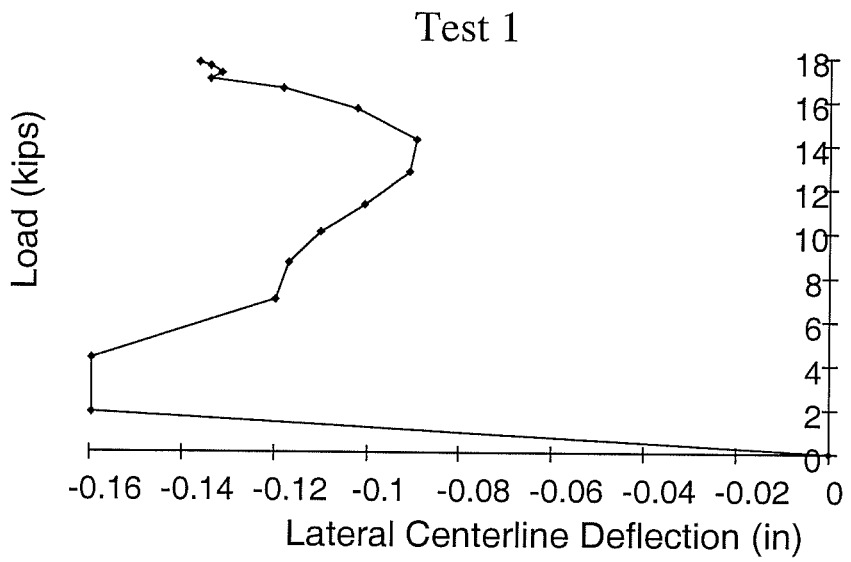
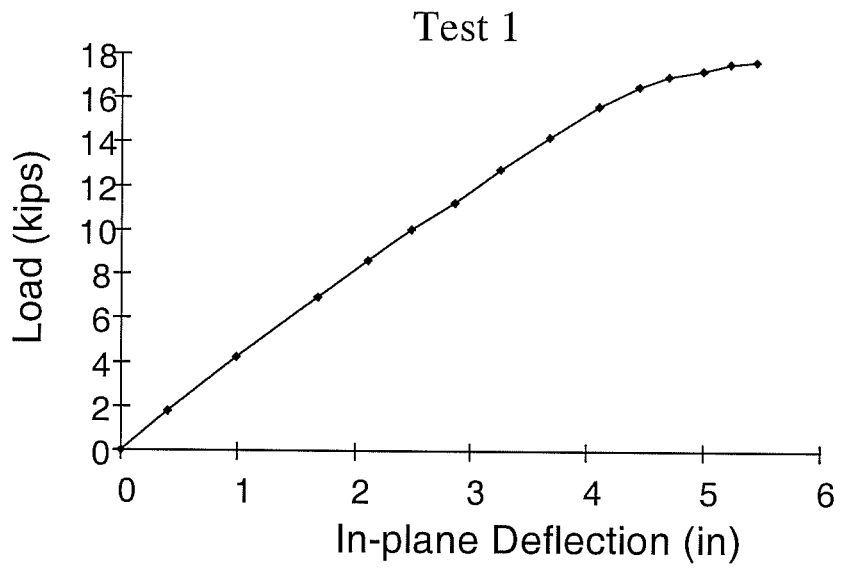
$$9. \quad \lambda = \frac{2}{\pi} K \sqrt{\frac{\sigma_{yfc}}{E} \frac{L}{b_{fc}}}$$

$$10. \quad K = 2, \quad A_w/A_{fc} \leq 2$$

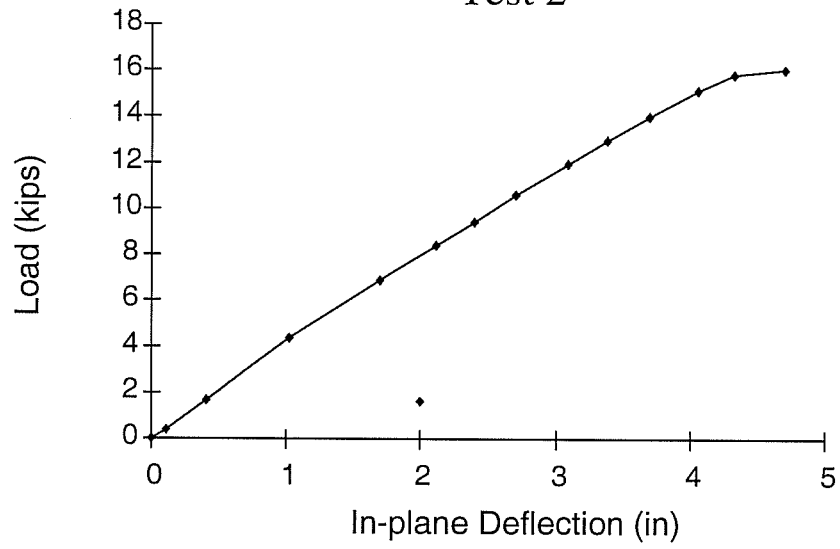
$$11. \quad K = \sqrt{3 + \frac{A_w}{2A_{fc}}} \quad A_w/A_{fc} \geq 2$$

APPENDIX II

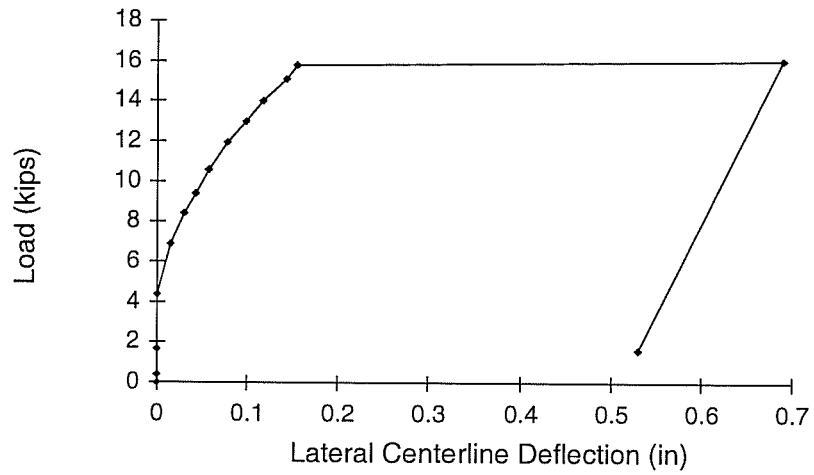
LOAD DEFLECTION PLOTS



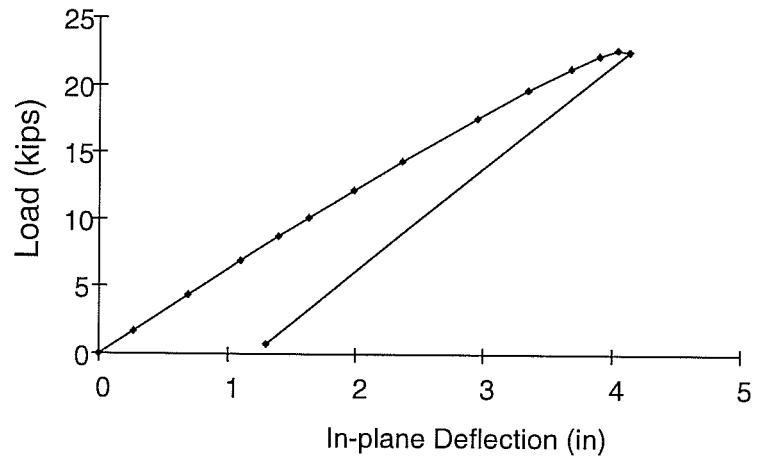
Test 2



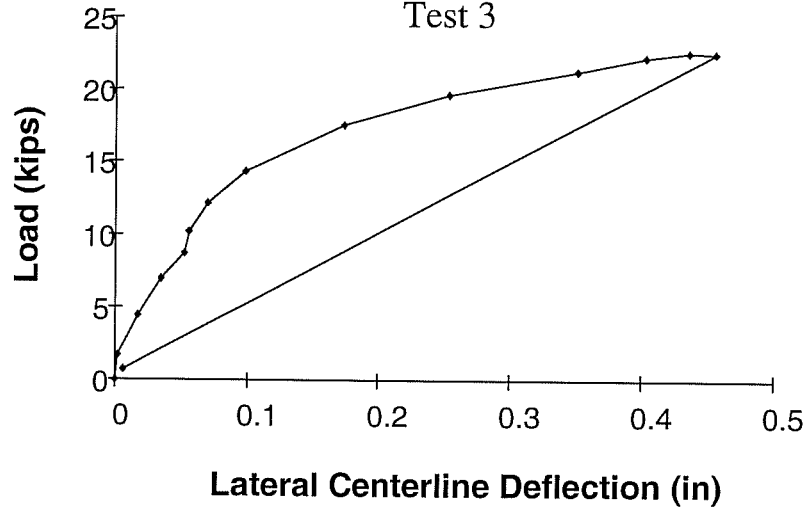
Test 2

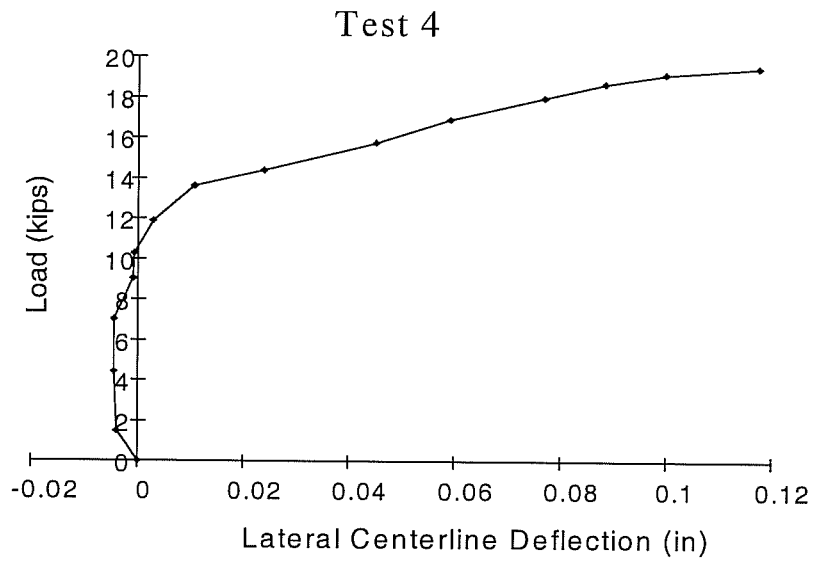
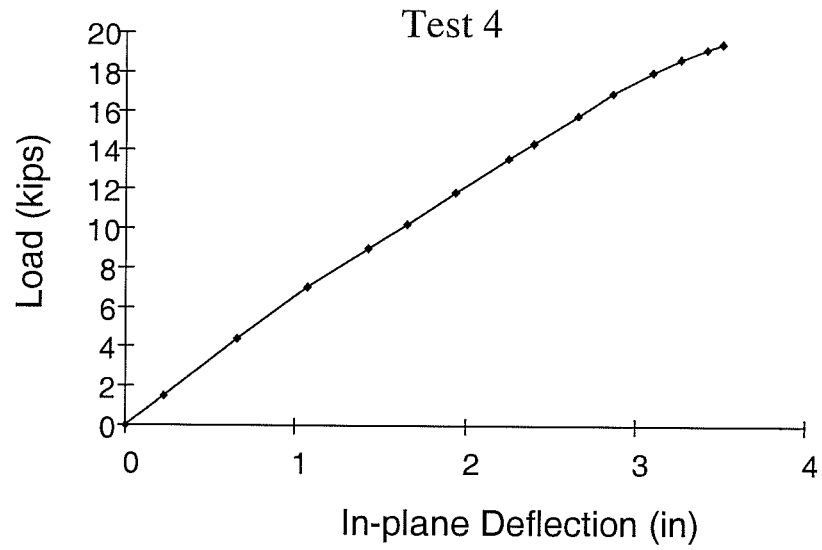


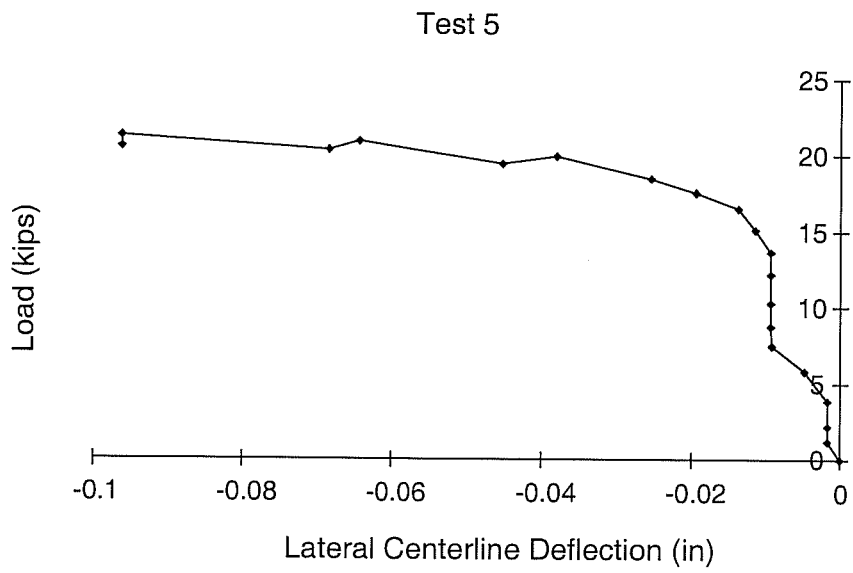
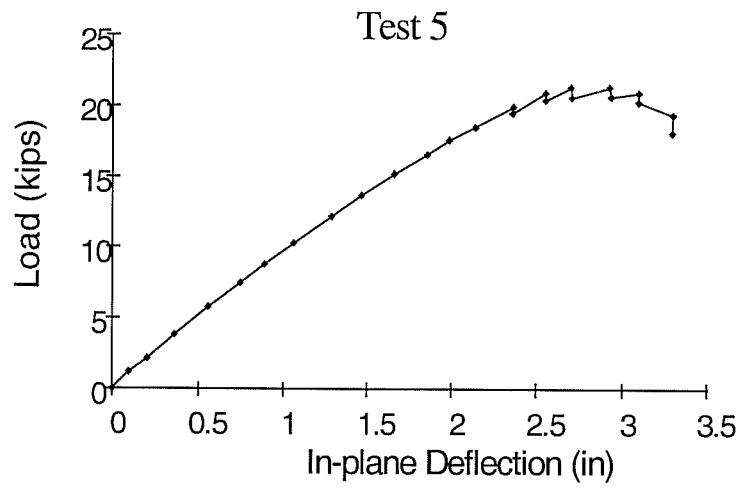
Test 3



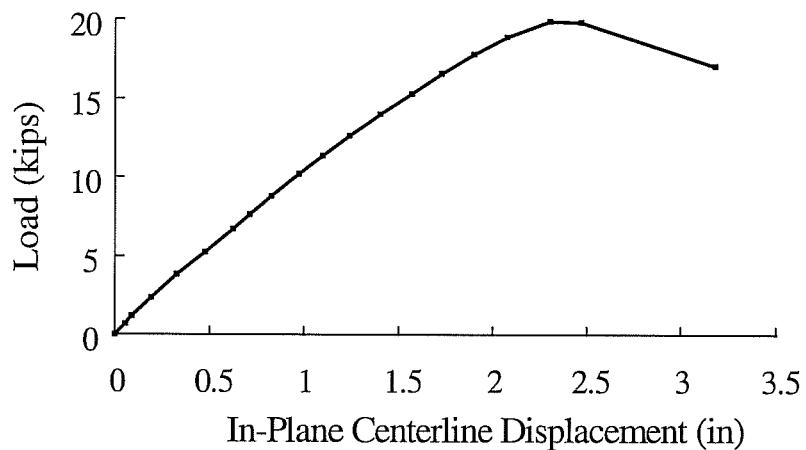
Test 3



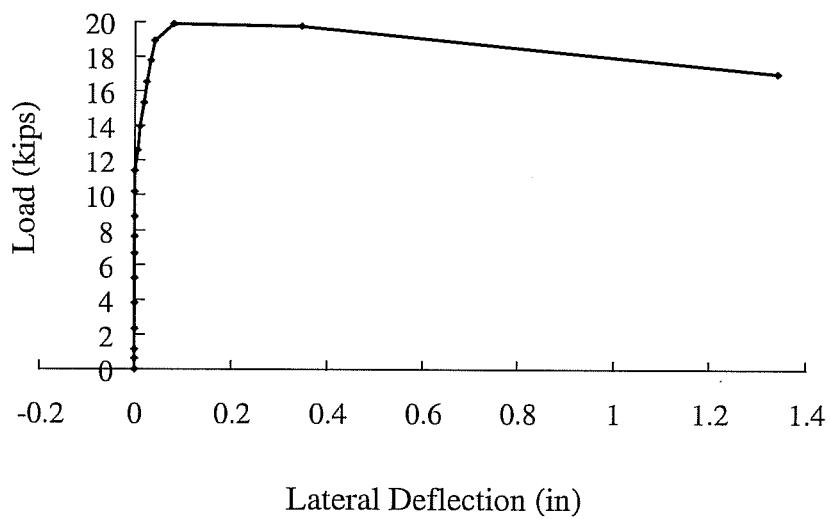


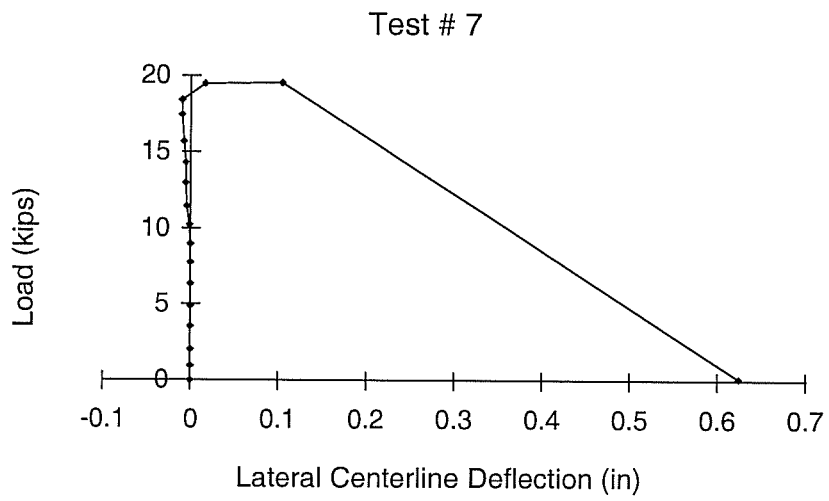
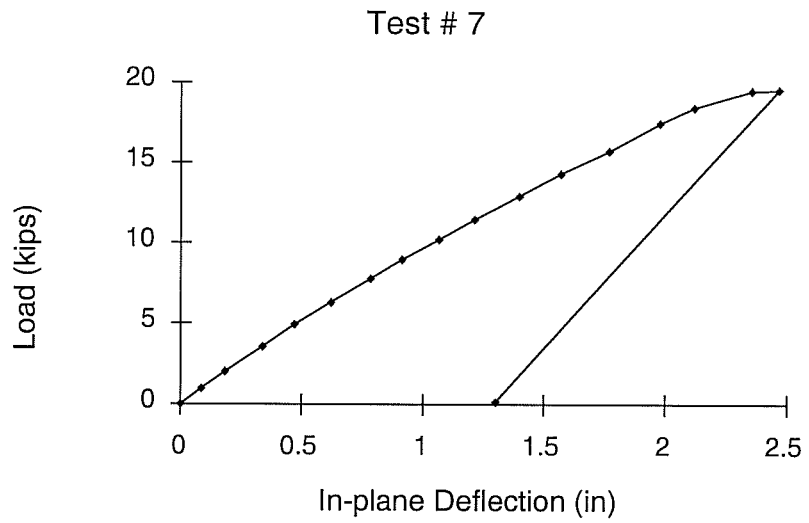


Test # 6

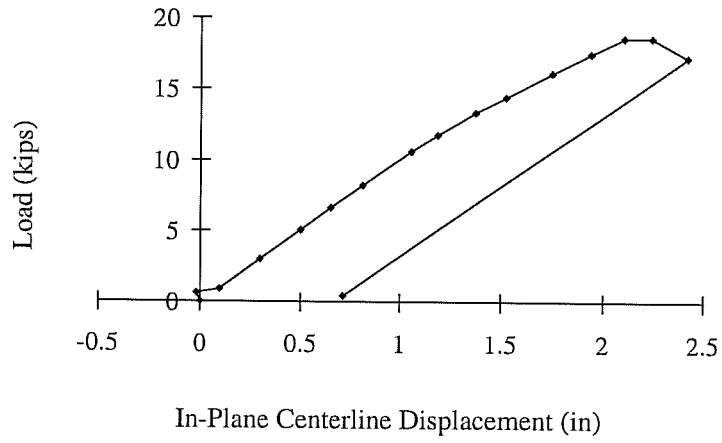


Test # 6

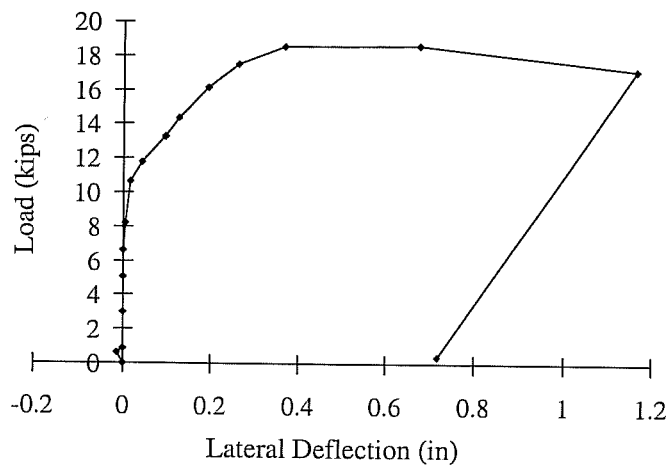


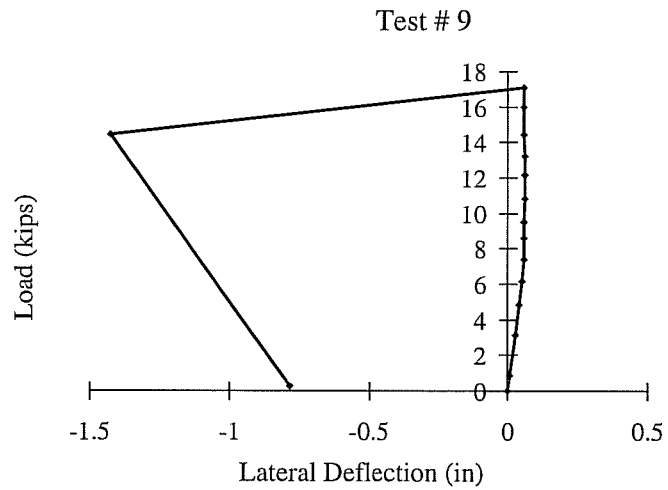
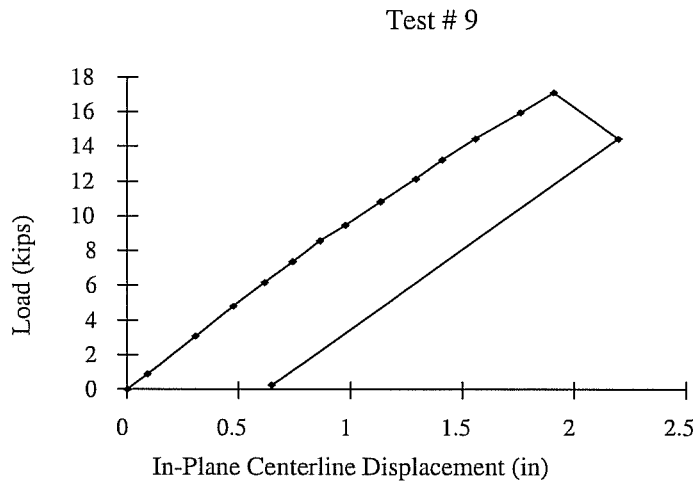


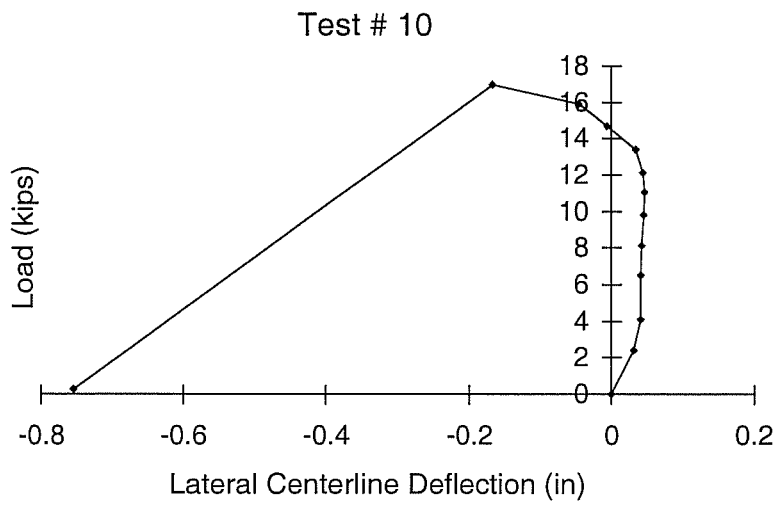
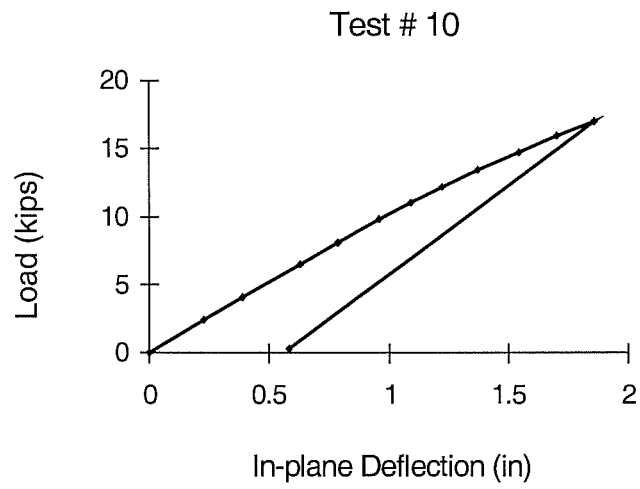
Test # 8

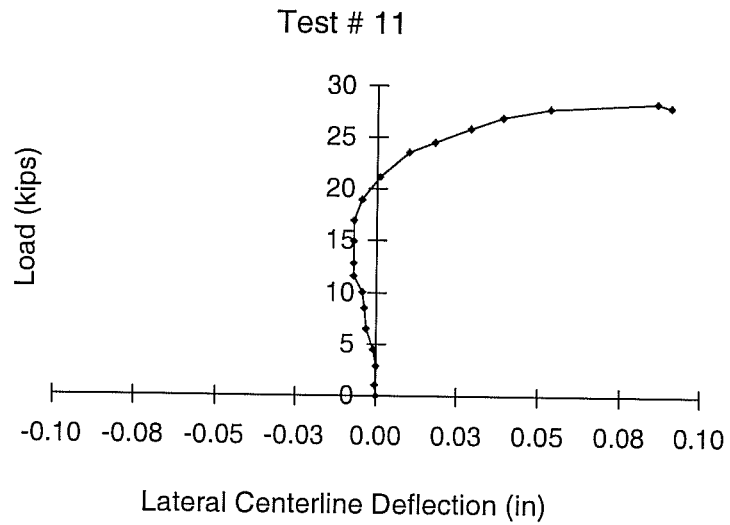
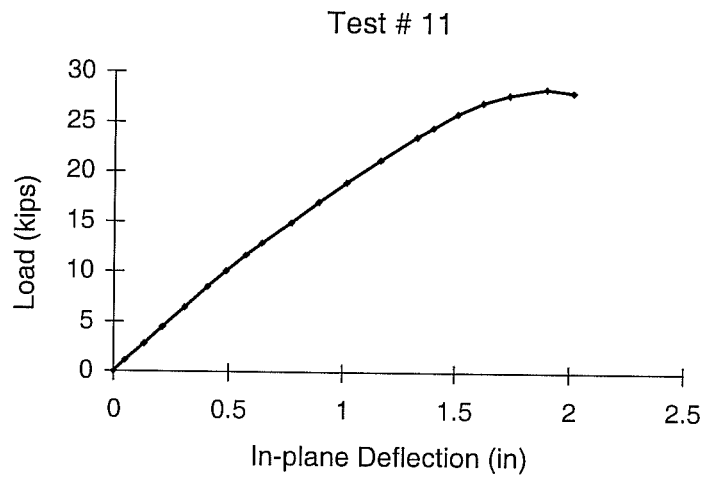


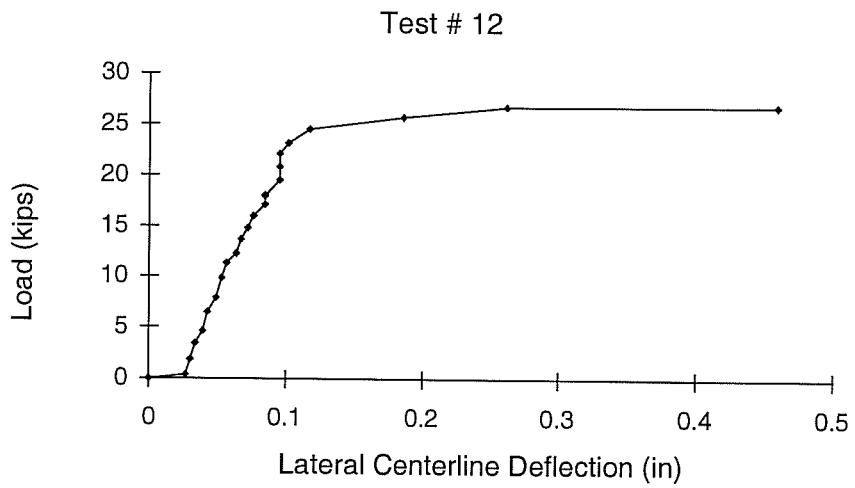
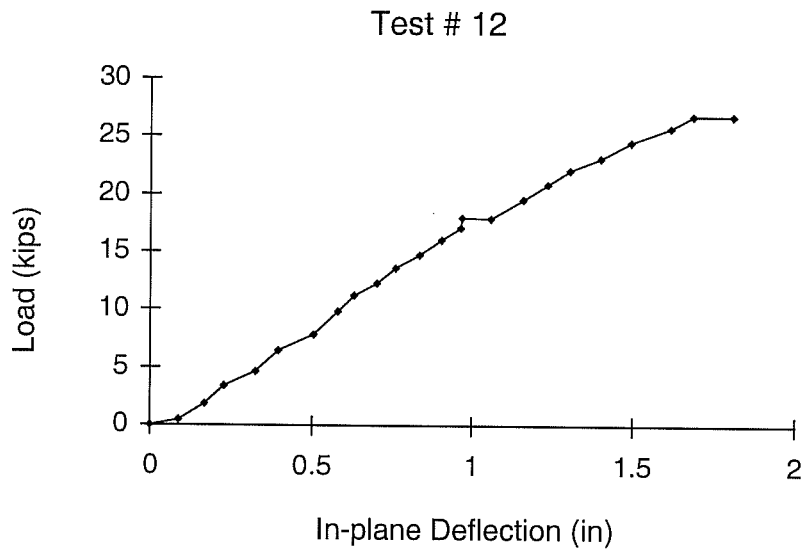
Test # 8

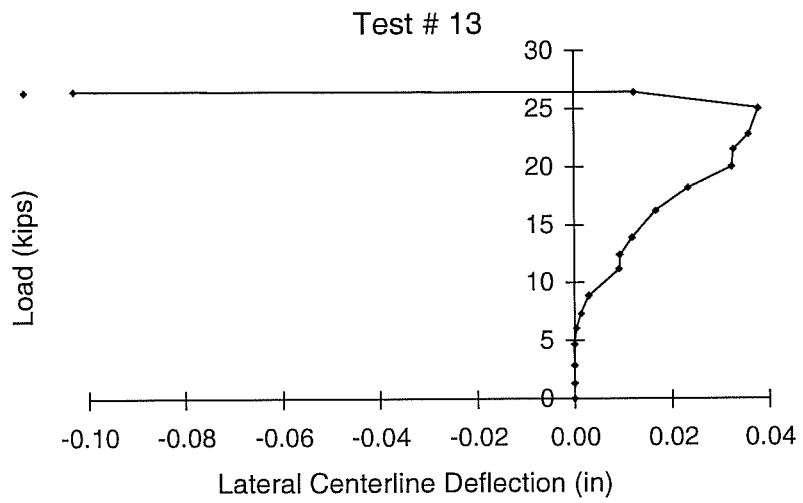
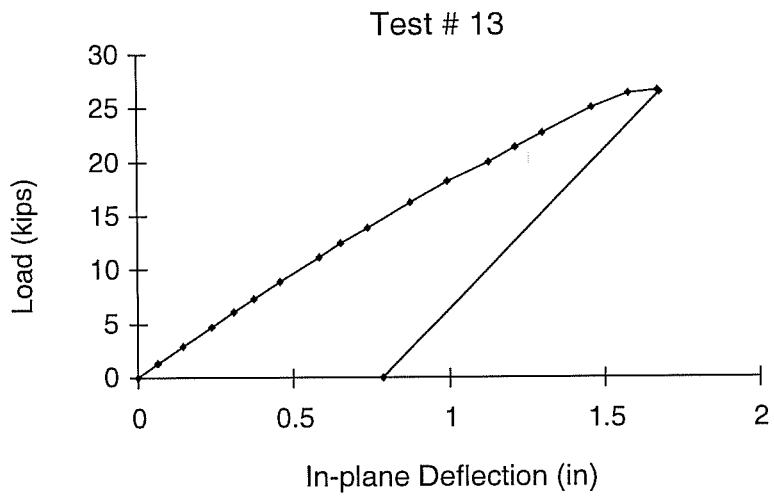


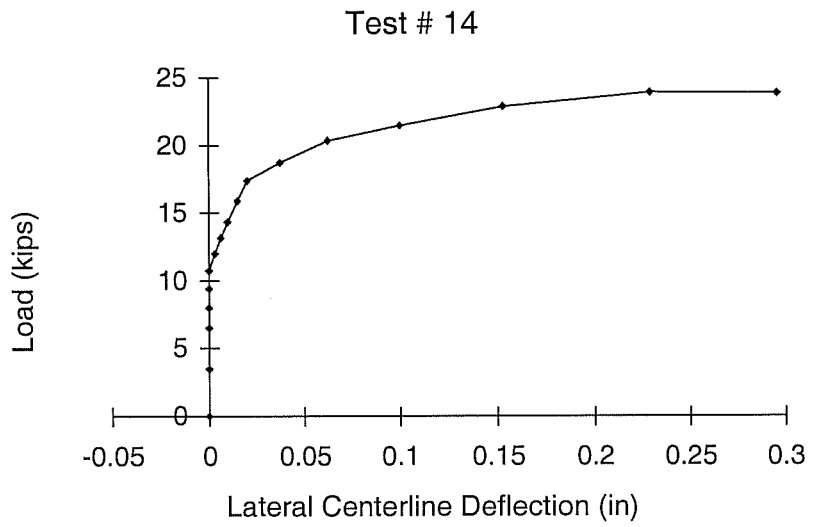
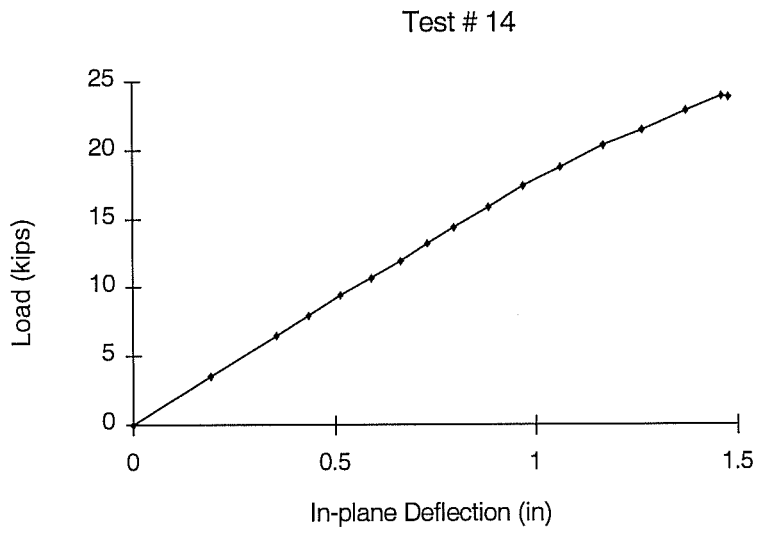


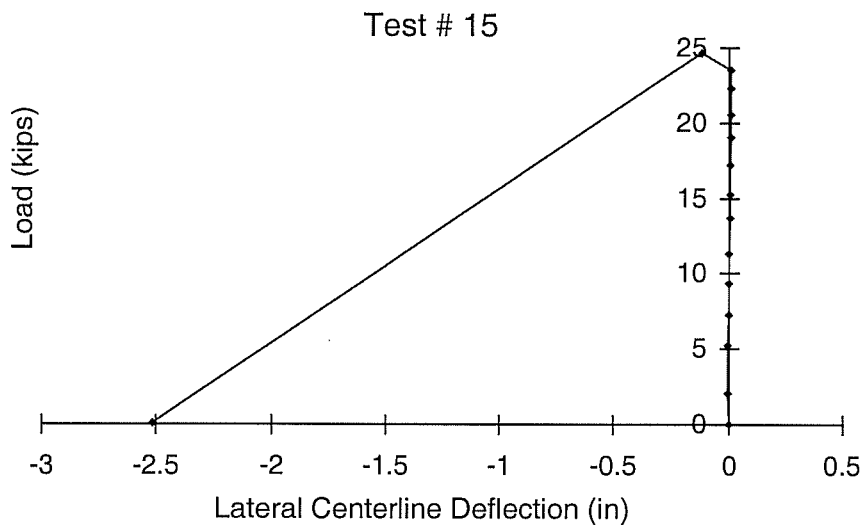
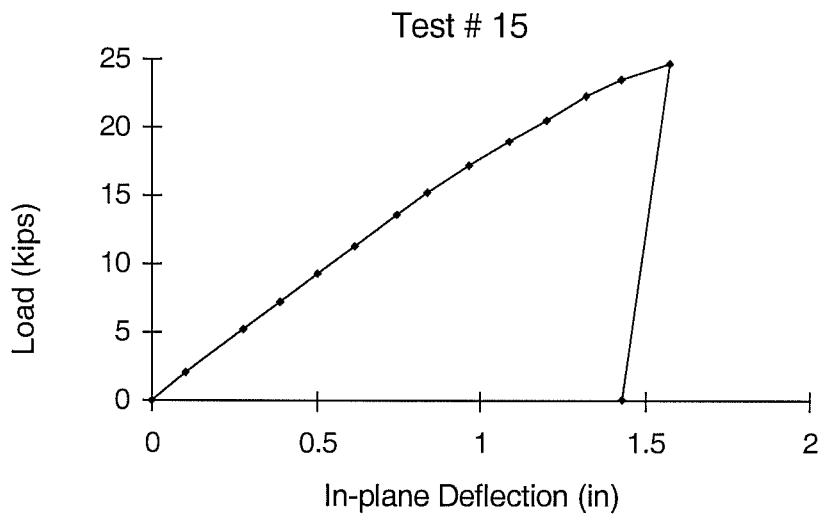




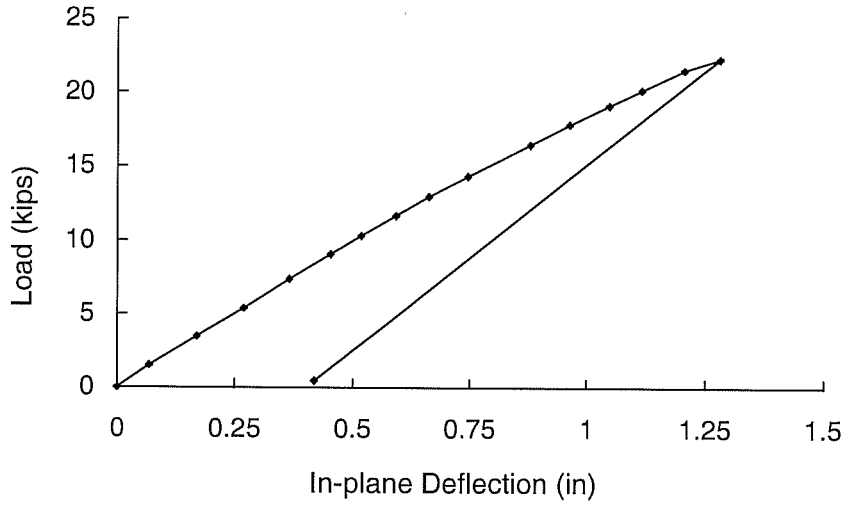




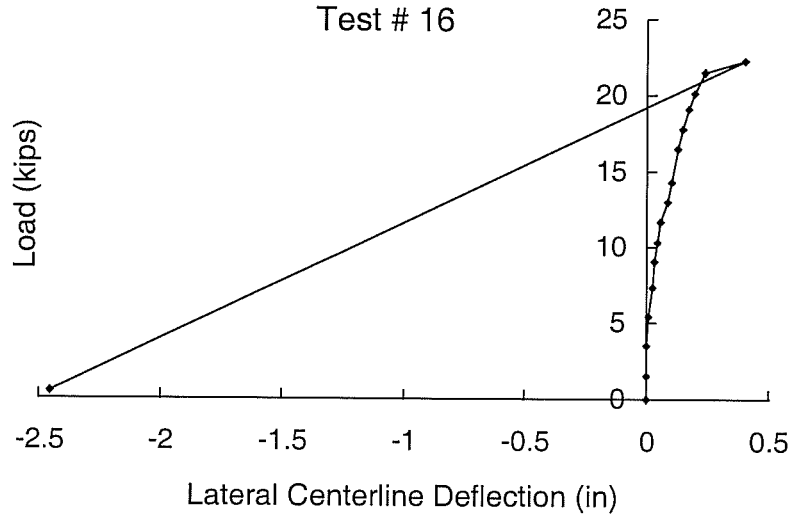


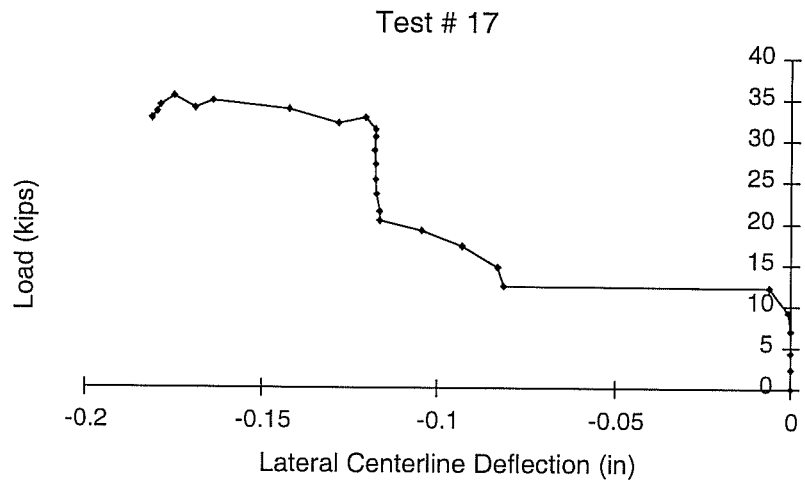
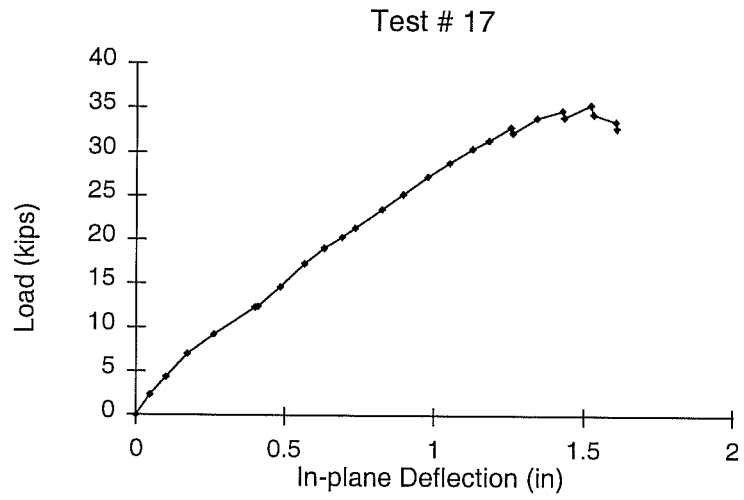


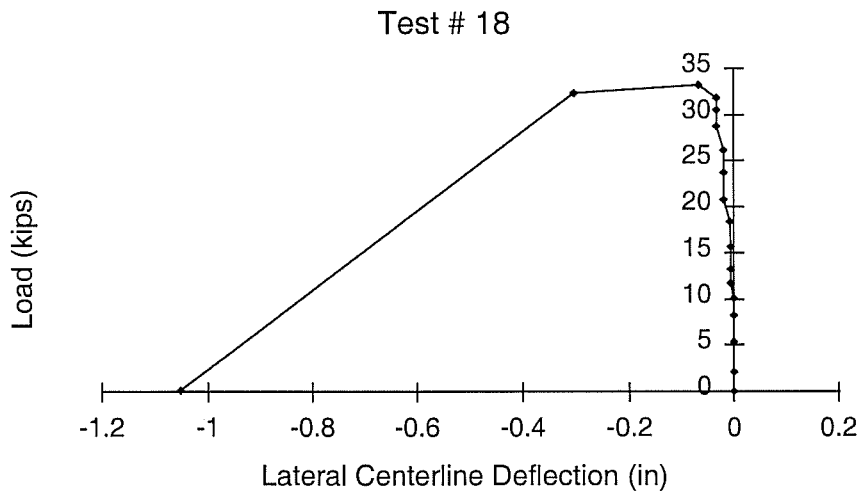
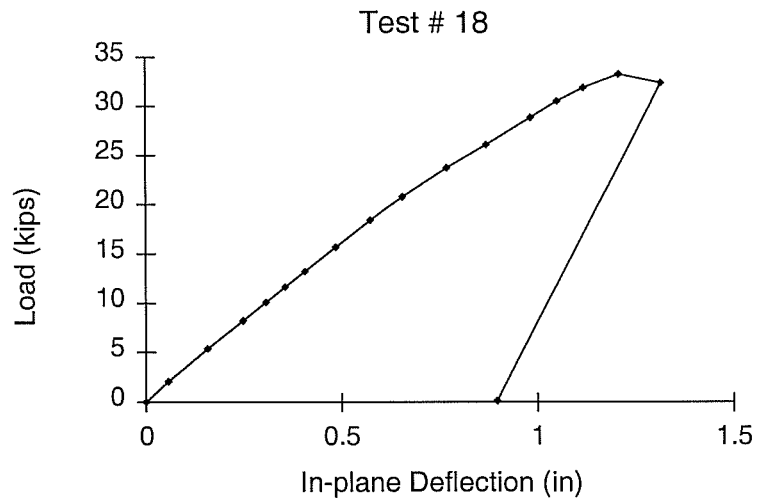
Test # 16

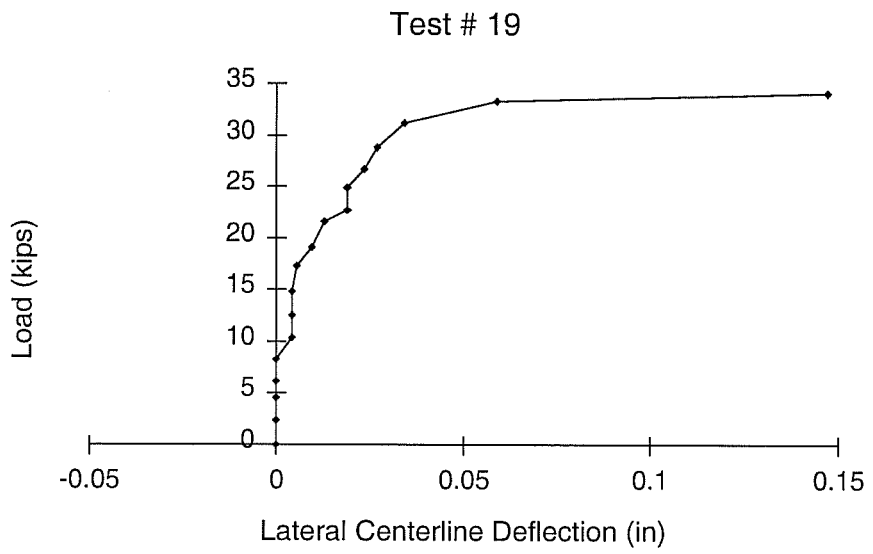
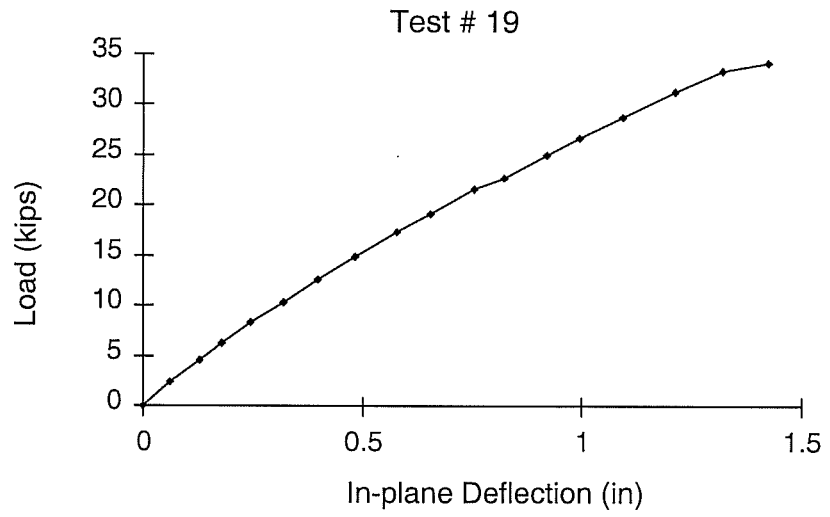


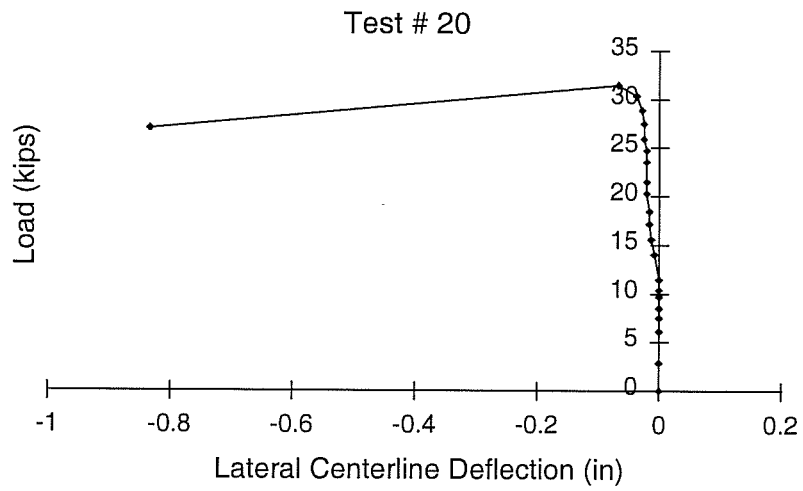
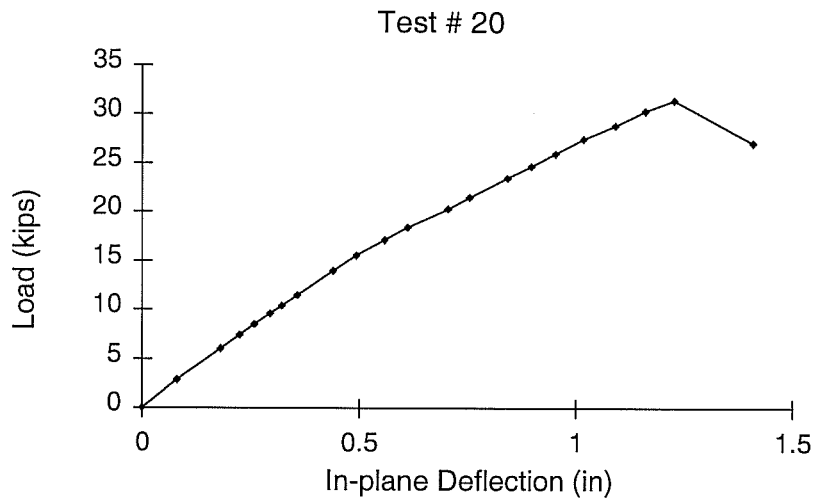
Test # 16

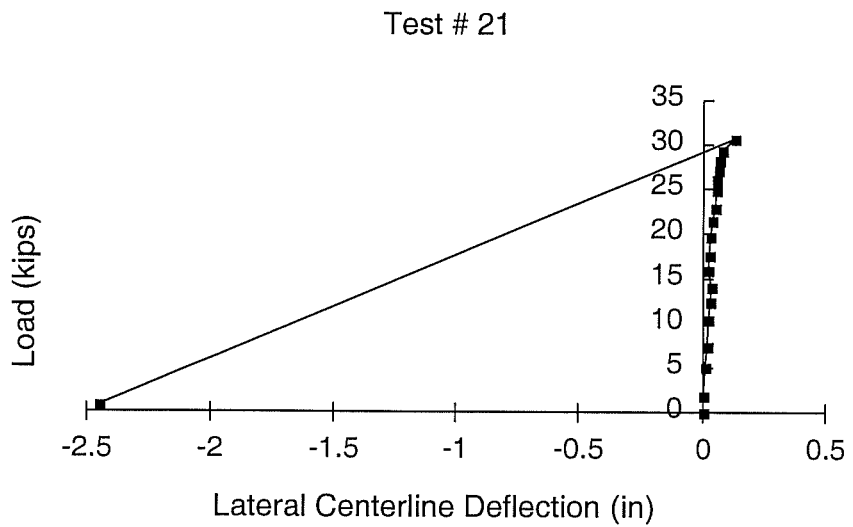
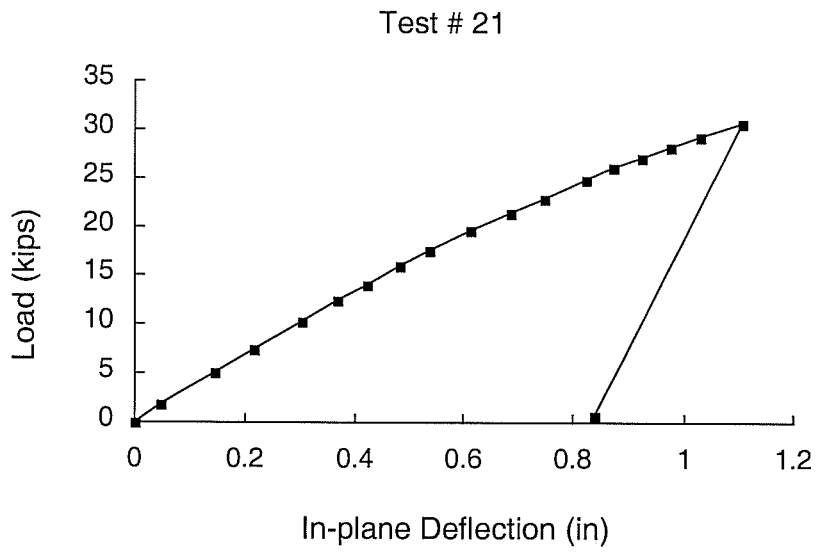


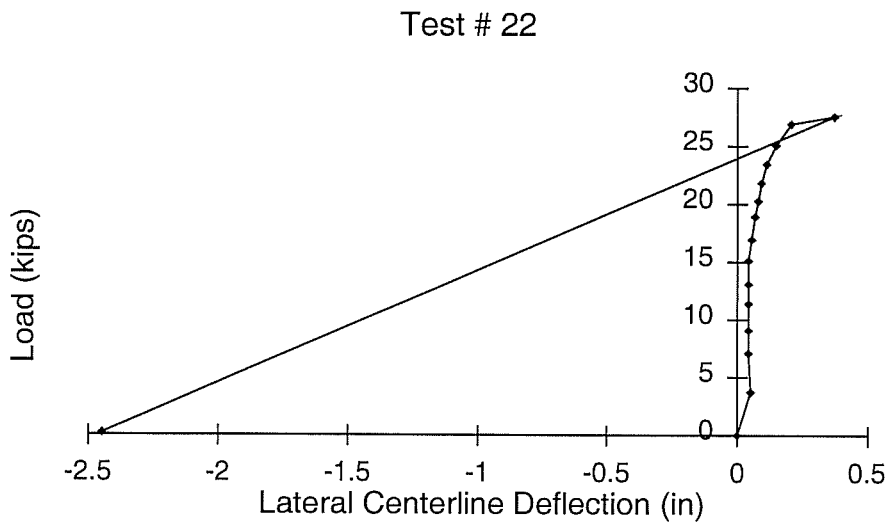
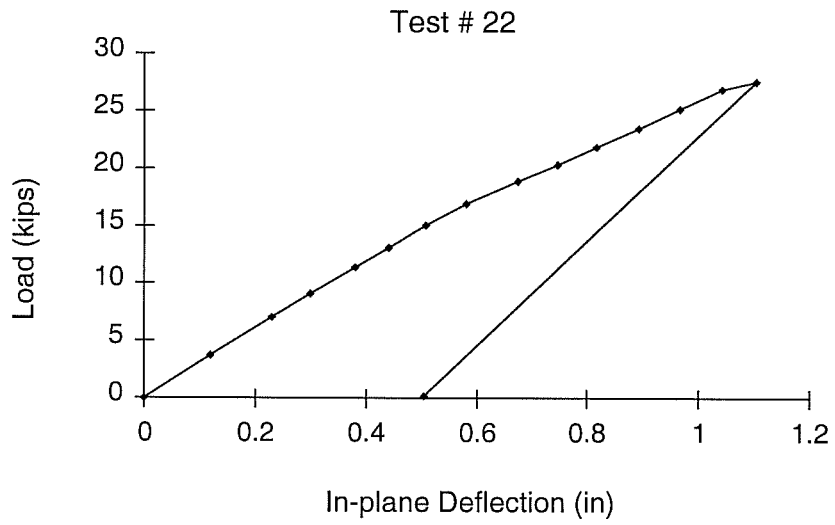




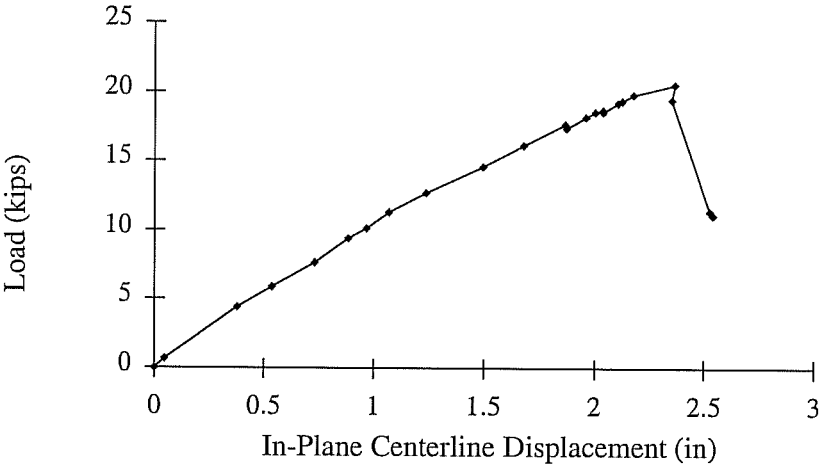




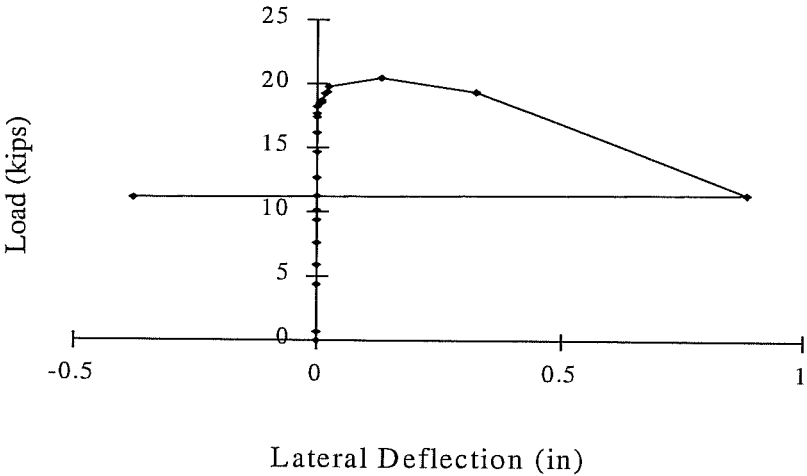


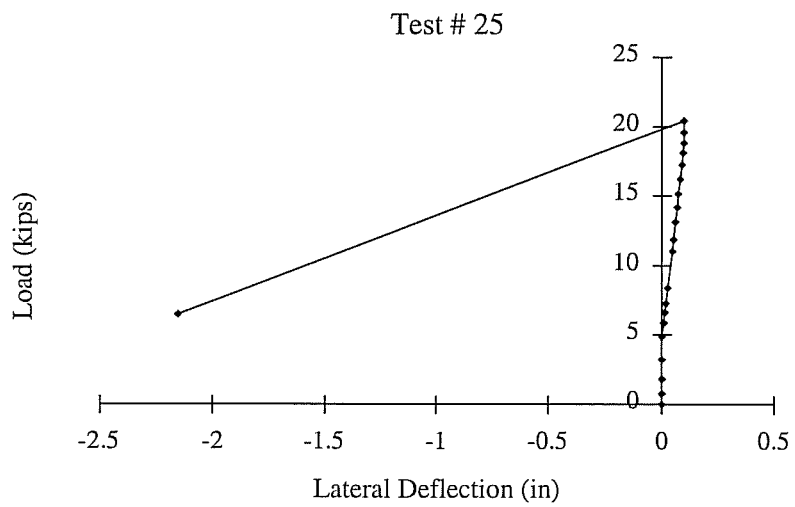
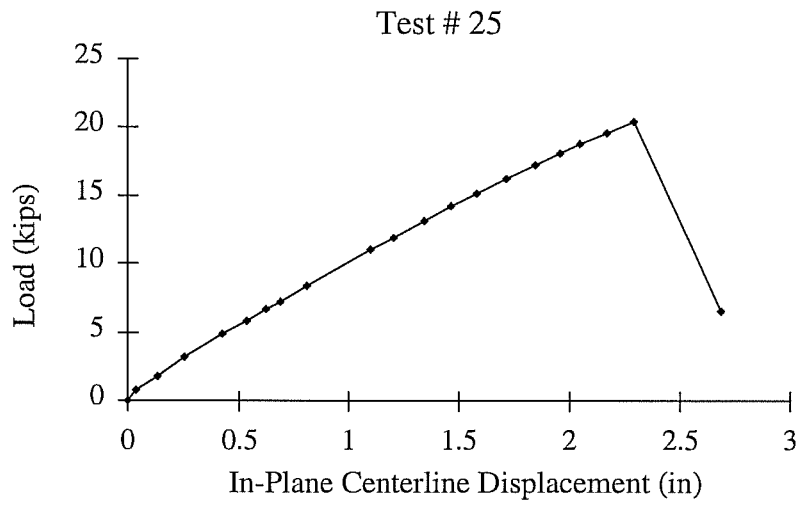


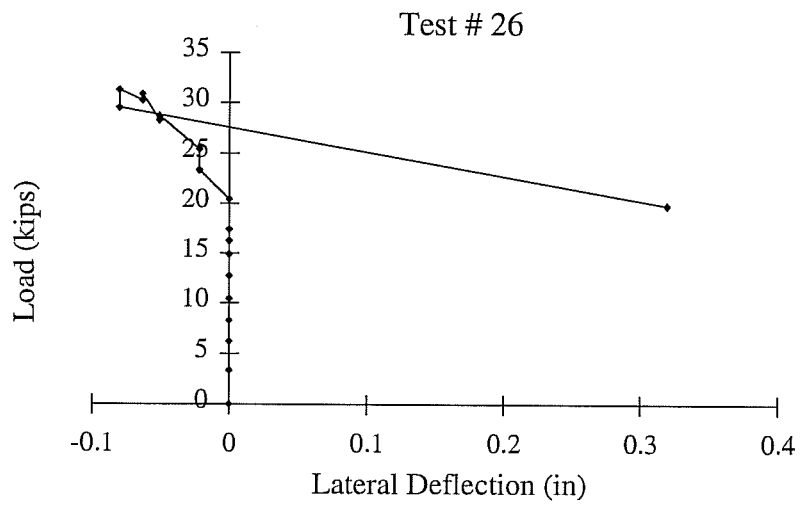
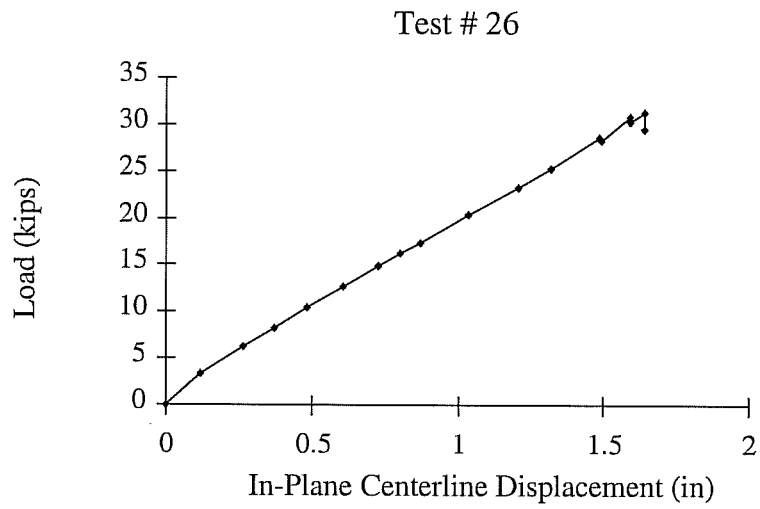
Test # 23 & 24

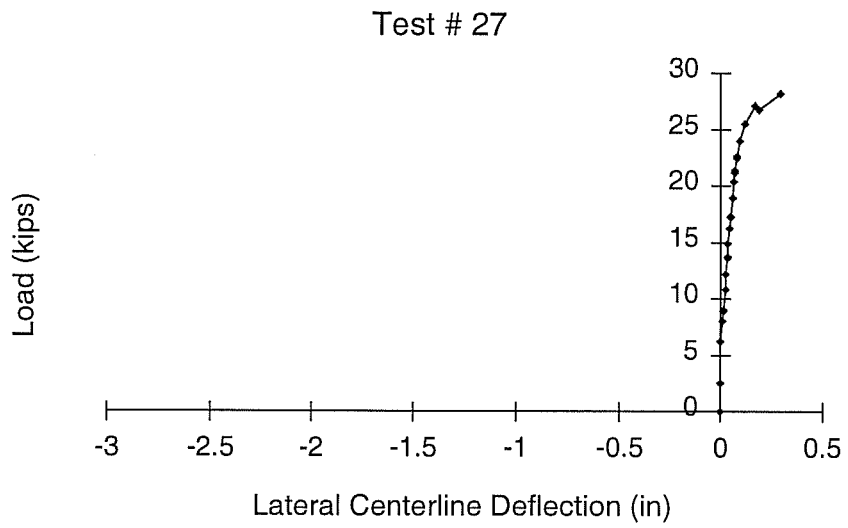
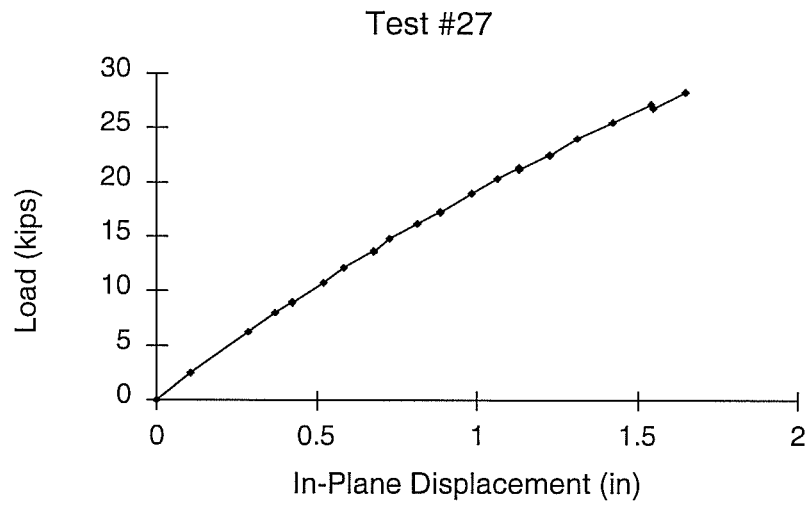


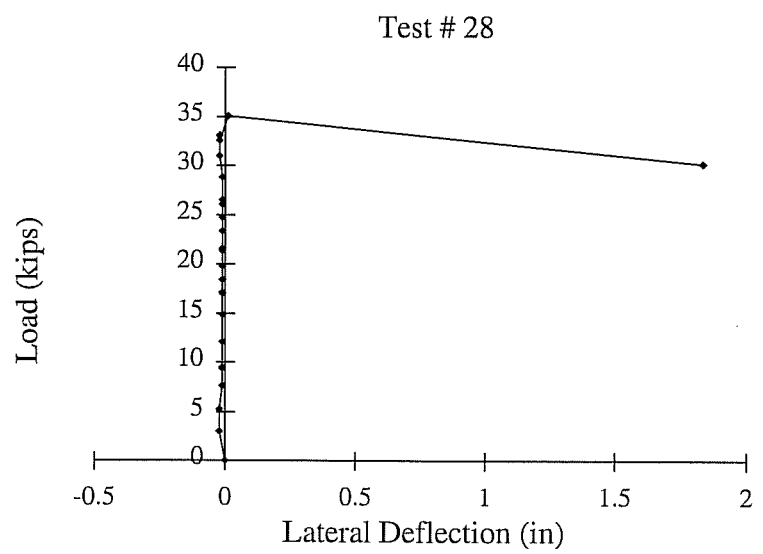
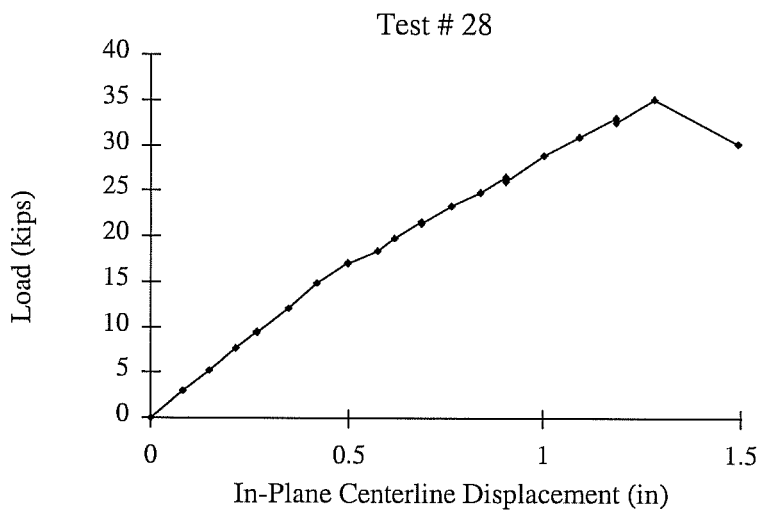
Test # 23 & 24



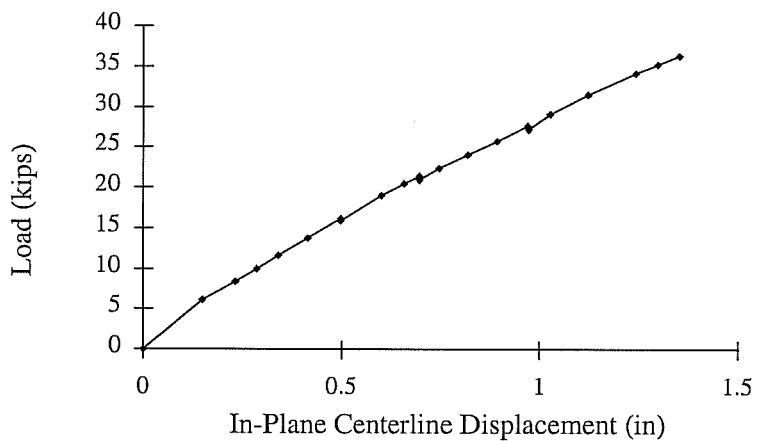




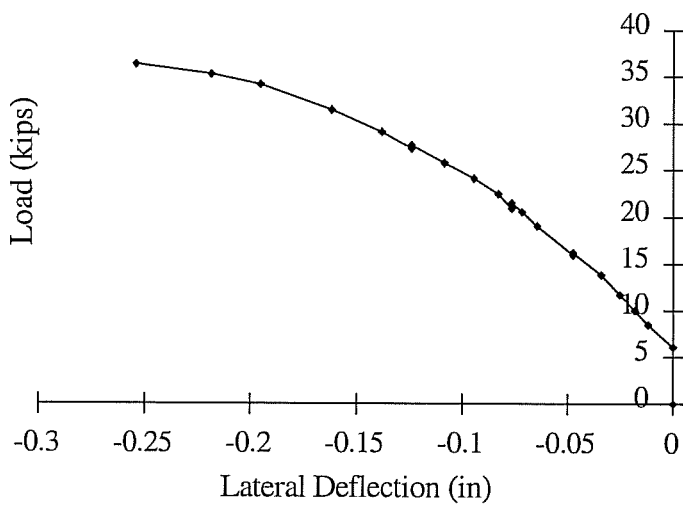




Test # 29



Test # 29



APPENDIX III:
LIST OF VARIABLES

A	Cross-sectional area, in ²
A _f	Area of flange, in ²
A _{fc}	Area of compression flange, in ²
a _r	Ratio of web area to compression flange area
A _w	Area of web, in ²
A _{wc}	Area of the compression portion of web, in ²
b _f	Flange width, in.
b _w	Flange width, in.
C _b	Moment gradient coefficient
C _{pg}	Plate girder coefficient
C _w	Warping constant, in ⁶
d	Overall depth of member, in.
D _{cp}	Depth of compression portion of web, in.
E	Modulus of Elasticity of steel, (29,000 ksi)
F _L	Smaller of (F _{yf} -F _r) or F _{yw} , ksi
F _{yf}	Flange yield stress (ksi)
F _{yw}	Web yield stress (ksi)
G	Sheer modulus of elasticity of steel (11,200 ksi)
h	Clear distance between flanges less the fillet or corner radius for rolled shapes; and for built-up sections, the distance between adjacent lines of fasteners or the clear distance between flanges when welds are used, in.
I _y	Moment of inertia in the y-direction, in ⁴
J	Torsional constant for a section, in ⁴
L _b	Unbraced length, in.
M _p	Plastic bending moment, kip-ft or kip-in
M _y	Initial yield bending moment, kip-in.
R _e	Hybrid girder Factor
R _{pg}	Plate Girder Reduction Factor
r _y	Radius of gyration in the y-direction
S _x	Elastic section modulus, in ⁴
t	Thickness, in.
t _f	Thickness of flange, in.
t _w	Thickness of web
Z _x	Plastic section modulus, in ⁴
λ	Slenderness parameter
λ _p	Limiting slenderness parameter for a compact element

λ_r Limiting slenderness parameter for a noncompact element

BIBLIOGRAPHY

- AISC. Manual of Steel Construction, Load and Resistance Factor Design, Volume 1, 2nd ed. Chicago, IL: American Institute of Steel Construction
- Barth, K. E. Thesis presented to Purdue University, May, "Moment Rotation Characteristics For Inelastic Design Of Steel Bridge Beams And Girders." 1996.
- Basler, K. "Strength of Plate Girders in Bending." Journal Of Structural Engineering, ASCE, Vol. 87, No. ST6. August 1961.
- Fukumoto, Y. Structural Stability Design. 1st ed. Oxford 1997
- Hibbit, Karlson & Sorensen, INC. ABAQUS User's Manuals Version 5.6 Vol. I, II and III. 1996.
- Johnson, D.L. (1985), *An Investigation into the Interaction of Flanges and Webs in Wide-Flange Shapes*, 1985 Proceeding SSRC Annual Technical Session, Cleveland, OH, Structural Stability Research Council, Lehigh University, Bethlehem, PA.

Metal Building Manufacturers Association. Low Rise Building Systems Manual. 1996.

Tall, L. Salmon & Johnson. Steel Structures, Design and Behavior Emphasizing Load and Resistance Factor Design, 4th ed. New York, NY: Harper-Collins Publishers, Inc., 1990 pg. 287.

Timoshenko, S.P., & Gere, J.M. Theory of Elastic Stability, 2nd ed. McGraw-Hill Publishing Company. 1961.

Yura, J.A., Galambos, T.V., & Ravindra, M.K. Salmon & Johnson. Steel Structures, Design and Behavior Emphasizing Load and Resistance Factor Design, 4th ed. New York, NY: Harper-Collins Publishers, Inc., 1990 pg. 560.

